Gamma/hadron discrimination using composite cherenkov telescopes

Shaw, Simon Edward

Shaw, Simon Edward (1999) *Gamma/hadron discrimination using composite cherenkov telescopes*, Durham theses, Durham University. Available at Durham E-Theses Online: http://etheses.dur.ac.uk/4356/

Gamma/Hadron Discrimination using Composite Cherenkov Telescopes

Simon Edward Shaw, BSc.

A thesis submitted to the University of Durham in accordance with the regulations for admittance to the degree of Doctor of Philosophy

November 1999

Department of Physics
University of Durham
South Road
Durham UK

Gamma/Hadron Discrimination using Composite Cherenkov Telescopes

Simon Edward Shaw, BSc.

PhD Thesis, November 1999

ABSTRACT

The Durham University Mk6 Ground Based Gamma Ray Telescope is a sensitive detector in the Very High Energy (VHE) band (~100GeV-10TeV). It is a 'composite' Cherenkov telescope consisting of three 42m^2 mirrors, each of which is viewed by a Cherenkov photon detector. Together the three detectors provide the basis for a sophisticated coincidence trigger that gives the telescope its low energy threshold of ~300GeV. Analysis of high resolution Cherenkov images from the central detector allows gamma rays to be identified from the hadronic background. The Left and Right detectors also record two independent, medium resolution, Cherenkov images. This thesis has investigated the use of the images from the Left and Right detectors to provide extra gamma/hadron discrimination power. Two measurements, represented by the parameters *dDist* and *LRconc*, have been identified that are capable of improving current VHE source detection significance by 20-30%.

In Chapter 1 some of the motivations behind the field of VHE gamma ray astronomy are discussed, along with brief explanations of VHE gamma ray production mechanisms. Potential astronomical sources of VHE photons are outlined in Chapter 2. In Chapter 3 the phenomenon of Cherenkov radiation emitted in the atmosphere from Extensive Air Showers (EAS) is introduced. The construction of Atmospheric Cherenkov Telescopes is considered in Chapter 4 and the Durham Mk6 telescope is detailed in Chapter 5. The moments method of analysing Cherenkov images is given in Chapter 6. Chapter 7 investigates the measurements that that could be made using data from the Left and Right detectors to identify gamma ray EAS from the hadron background. The effects on these measurements of various aspects of the Mk6 telescope's performance are also researched here and in further detail in Chapter 8. Finally a summary and some suggestions for future work are given in Chapter 9.

PREFACE

The work described in this thesis has been associated with the Durham University Atmospheric Cherenkov Telescopes in Narrabri, NSW, Australia. The author has participated in the operation, maintenance and development of the Mk6 telescope in Narrabri. At the University of Durham the author has also been involved in the routine pre-processing and analysis of data as well as the development of Monte-Carlo simulation models of the Mk6 telescope. The GENESIS air shower simulation computer programme was adapted by the author from the original code, written by K. J. Orford. All of the material presented in this thesis is the author's own work, none of which has been submitted previously for admittance to a degree in this or any other University, except where due reference is made.

ACKNOWLEDGEMENTS

There are many people to whom I am indebted for their assistance and support throughout the course of this thesis. I would especially like to express my gratitude to my supervisor, Keith Orford, for many useful conversations and ideas. My thanks also go out to past and present colleagues at the Observatory, in particular Steve Rayner for his willingness to help and ability to put up with sharing an office with me. Professor Ted Turver, is also thanked for employing me as a Research Assistant for this last year.

This thesis has been made possible through the provision of the facilities of the Physics Department at the University of Durham, for which I thank Professor B. Tanner, and my research studentship which was funded by the Particle Physics and Astronomy Research Council.

To the many people who would not accept that I could not complete this thesis, thank you for not believing me.

CONTENTS

Chapter 1

HIGH ENERGY ASTRONOMY

1.1 Introduction

As an A-level physics student my class mates and I were shown a gold leaf electroscope by our lecturer, Pete Naylor. The leaf was hanging away from vertical by 45 degrees or so but by the end of the lesson had dropped considerably. We were asked why we thought this had happened and next lesson insisted that the electroscope was insulated from the bench by standing it on a thick block of polystyrene foam. By the end of the lesson the leaf had dropped.

The problem of how the charge on the leaf could leak away baffled scientists at the turn of the century (see [107] for a full history). Rutherford and Cooke [142] showed in 1903 that most of the loss was due to naturally occurring ionising radiation and prolonged the discharge time by encasing their electroscope in metal. By the early 1910s however, the origin of the ionisation responsible was found not to be terrestrial. Balloon flights by Goeckel [76] and Hess [81] expected to show a decreasing flux of the radiation with altitude and were surprised to find this only true to ~1.5km. Above this altitude the flux steadily increased to the altitude of the highest balloon experiments by Kolhörster of 9km. The radiation had to be extraterrestrial in origin and the term 'cosmic radiation' was first used by Milikan in 1925 to describe it.

The very high penetrating power of the radiation implied that the flux consisted of high energy gamma rays. It was not until the invention of the Geiger-Müller tube in 1929 and subsequent experiments by Bothe and Kolhörster that 'cosmic rays' were identified as being predominantly charged particles of high energy. In fact the mean energy of cosmic-ray particles arriving at Earth is ~1GeV with an energy density ~1eV cm^{-3} — about the same as the galactic energy densities of starlight, the thermal gas in the interstellar medium and the galactic magnetic fields.

Despite the apparent large numbers and high energies of cosmic rays arriving at Earth, their origin is still not certain. On arrival at Earth the charged cosmic ray particles have been deflected by the galactic magnetic field to the extent that it is not possible to tell where they have come from. Only neutral particles can retain any directional information and of the total cosmic ray flux $\sim 10^{-4}$ consists of gamma rays which can travel cosmological distances undeflected. The following sections will show that gamma rays are often produced where high energy cosmic rays exist. If gamma rays can be successfully detected at Earth they can be used as a probe for the sources of the large flux of cosmic-ray particles and offer an insight in to the mechanisms by which cosmic-rays are produced and accelerated.

1.2 Very High Energy Photon Production

The electromagnetic spectrum continues from optical through X-rays to the gamma ray range with photons of different energies being produced by a continuum of processes. Very generally X-rays are atomic in origin, due for example to electron transitions in the field of an atom, where as gamma rays are due to nuclear or particle interactions. The lowest energy photon that can be made by particle annihilation occurs when an electron-positron pair meet and produce two photons each with energy in the centre of mass frame of the rest mass of the electron, 511keV. This energy is often taken arbitrarily to define the start of the gamma ray region of the electromagnetic spectrum.

The area of interest for VHE astronomy concerns photons of energies ranging from ~0.1 - 10TeV (1TeV = 10^{12}eV). In this energy range gamma rays are emitted by accelerating charged particles and particle interactions. The rate of energy loss by the particles in these processes are inversely proportional to some power of the particle mass which means that accelerated electrons and positrons are the dominant source of the radiation. For simplicity electrons and positrons will often be referred to collectively as 'electrons' from here on.

1.2.1 Synchrotron Emission

Synchrotron radiation is emitted by a gyrating charged particle travelling relativistically in a magnetic field. High energy electrons travel in a helix along magnetic field lines resulting in an oscillating electromagnetic field which is emitted as photons (figure 1.1). The photons are polarised depending on the angle at which they are viewed. When observed along the field lines the radiation is cir-

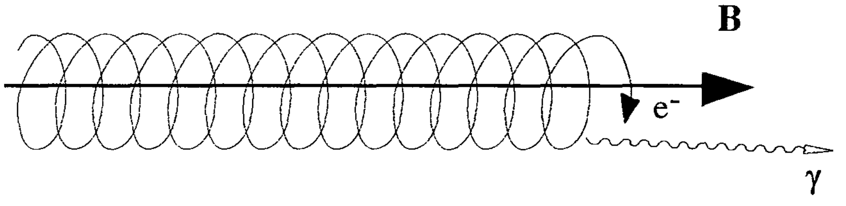

Figure 1.1: Emission of synchrotron radiation by a high energy electron.

cularly polarised and strongly beamed in the direction of the net particle motion. For a particle moving with velocity βc the relativistic Lorentz factor, γ, is given by

$$\gamma = \frac{1}{\sqrt{1-\beta^2}}. \tag{1.1}$$

The synchrotron radiation is contained within a cone with half angle $\sim 1/\gamma$. Lighter particles are more efficient at emitting synchrotron radiation since the rate of photons emitted is a function of the particle mass, $\propto 1/m^4$. Therefore the rate of emission from electrons is considerably higher than for protons. A synchrotron emission spectrum is characterised by three regions, illustrated schematically in figure 1.2. A power law electron energy distribution, of index s, produces a power law synchrotron emission spectrum. The index, α, of the optically thin emission region of the spectrum is linked to s by a simple expression, $\alpha = (1-s)/2$ [139]. At low frequencies the synchrotron emission is self absorbed by collisions with the same radiating electrons leading to a turnover and fall off in the spectrum. At higher frequencies the photons are emitted by the highest energy electrons which radiate large fractions of their energy. The spectrum departs from a power law at these frequencies as the electrons suffer severe energy loss. The typical energy,

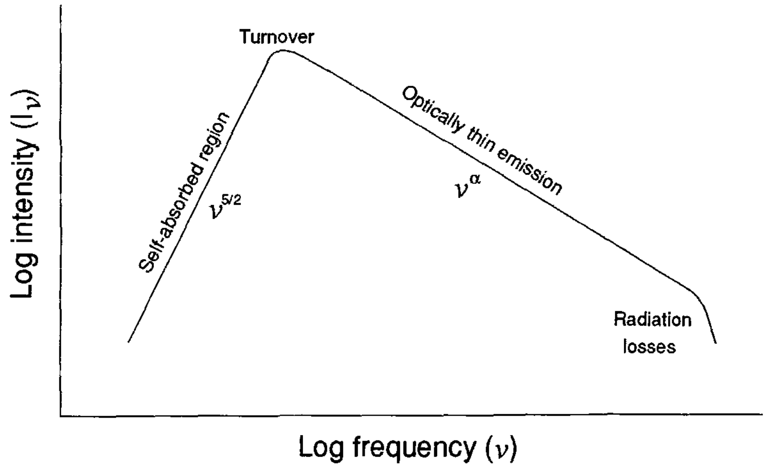

Figure 1.2: Schematic of a synchrotron spectrum (after Robson 1996).

E_γ GeV, of radiation emitted by electrons with energy, E_e, in a magnetic field, B, can be given by

$$E_\gamma \approx 20BE_e^2, \tag{1.2}$$

when the electron energy is measured in EeV (10^{18} eV) and the magnetic field measured in μG. Hence the energy of photons emitted is considerably less than that of the radiating electrons and it is rare for synchrotron photons to be observed at VHE energies. The presence of X-ray synchrotron radiation from an object indicates that electrons of energy high enough to produce gamma rays by other methods are present.

1.2.2 Curvature Radiation

Curvature radiation was proposed to explain gamma ray emission from pulsars and is very similar to synchrotron radiation [147]. In the region of a pulsar very strong, curved magnetic fields are present ($B \sim 10^{12}G$). Any charged particle

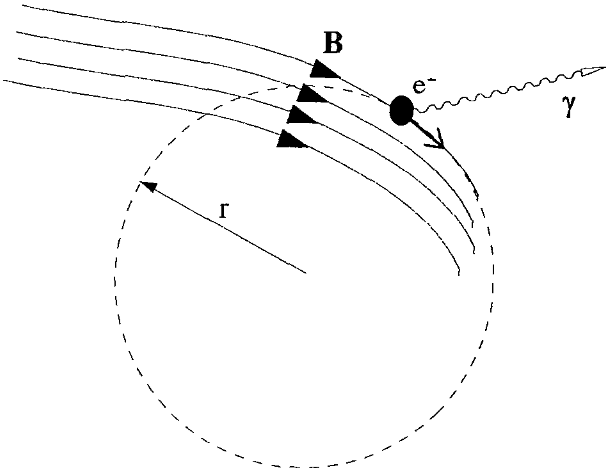

Figure 1.3: Curvature radiation in a high magnetic field.

will follow these field lines very closely; even if it is highly energetic because any motion across the field lines will result in damping by synchrotron emission. The emission depends on the strength and radius of curvature of the field lines and the kinetic energy of the particle. The observed photon energy emitted is $\sim \gamma^3$ times the angular frequency of the electrons, $\beta c/r$. Magnetic fields $> 10^{12}$G are needed to produce gamma rays by this method. A sketch of the process is shown in figure 1.3.

1.2.3 Bremsstrahlung

The German for 'braking radiation' describes this process of photon production very well. When an accelerated charged particle passes within the electromagnetic field of an atomic nucleus or electron it experiences a change in direction and emits a photon. The energy of the photon depends on the size of the deflection with the maximum energy obtainable approximately equal to the kinetic energy of the initial particle. The rate of energy loss for a charged particle by bremsstrahlung

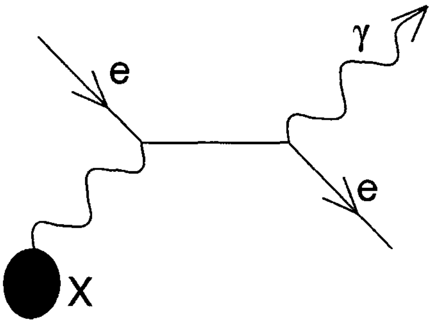

Figure 1.4: Feynman vertices for the bremsstrahlung process.

is inversely proportional to the square of the mass of the particle, i.e. ~10^6 times higher for electrons than protons. The Feynman diagram for bremsstrahlung is shown in figure 1.4.

1.2.4 Inverse Compton Effect

Figure 1.5 shows the Feynman diagram for the inverse Compton effect where a relativistic electron interacts with a low energy photon in a radiation field and loses energy, thus boosting the photon to higher energies. To a relativistic electron of energy γmc^2, a low energy photon of energy E looks as if it is of a much higher energy $E' = \gamma(E + cp_l)$, where p_l is the longitudinal component of the photon's momentum. In the case of a head on collision, $E' = 2\gamma E$ and if all the electron's longitudinal momentum is given up in the interaction, the photon will be boosted to a higher energy $E'' = 2\gamma^2 E$. If the original photon is of a low enough energy so that $E' \leq 1$MeV then the cross-section for interaction is large enough to make the inverse Compton effect an efficient method of producing VHE energy photons.

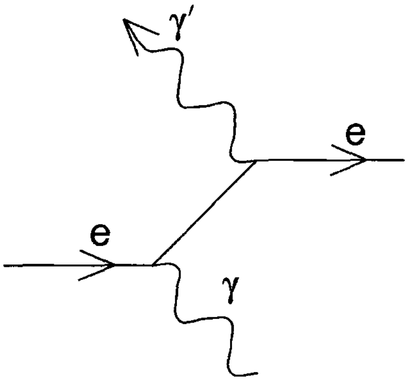

Figure 1.5: Feynman vertices for the inverse Compton effect.

1.2.5 Pion Decay

In the above processes, high energy photons are produced mainly by accelerated particles. The cross-section for the processes involve a mass dependence of the accelerated particle which means that the lighter electrons dominate the emission of gamma rays. An efficient method of generating gamma rays due to the interaction of high energy protons (or neutrons) with matter is the decay of the neutral π^o. The π^o particle is produced in interactions between high energy nucleons and is a short lived meson with rest mass, m =135 MeV/c^2. It has a very short lifetime of 2.6×10^{-8}s before decaying to two gamma rays, which are produced with energy $E_o = m/2$ in the meson rest frame. The photon energies translate to the observers reference frame via the following for a pion with velocity βc

$$E_\gamma = E_o \left(\frac{1-\beta}{1+\beta}\right)^{(\pm)\frac{1}{2}} . \tag{1.3}$$

Table 1.1: Examples of astrophysical locations of photon fields, of energy E_b, where the pair production mechanism is important for attenuating gamma rays of energy E_γ (after Longair 1997).

Background	Example Location	$E_b(eV)$	$E_\gamma(eV)$
Cosmic Microwave Background	Extragalactic Space	6×10^{-4}	4×10^{14}
Starlight	Interstellar Space	2	10^{11}
X Ray	Neutron Star	10^3	3×10^8

1.3 VHE Photon Attenuation

1.3.1 Photon-Photon Pair Production

Photon-photon absorption is the production of an electron-positron pair by the interaction of two photons,

$$\gamma + \gamma \longrightarrow e^- + e^+. \tag{1.4}$$

For two photons with momentum vectors separated by θ, pair production occurs above a threshold energy when the product of the energies of the two photons, $E_{bg}E_\gamma$, is greater than the mass energy of the electron-positron pair in the centre of mass frame, $E_{bg}E_\gamma = 2(mc^2)^2/(1 - \cos\theta) = 0.24\text{TeV}$. Table 1.1 shows combinations of gamma ray (E_γ) and background photon (E_{bg})energies that are important for the pair production process in astrophysical situations. The cross-section, $\sigma_{\gamma\gamma}$, for this process is such that it reaches a maximum a little above the threshold and decreases with increasing total energy, $\sigma_{\gamma\gamma} \propto E_{cm}^{-3/2}$ [119].

The interaction length for this process depends on the spectral distributions of the background and gamma ray photons. The process is important for gamma rays near a neutron star, due to the high X-ray radiation density present, and for the Cosmic Microwave Background Radiation (CMBR) over extragalactic distances.

1.3.2 Single Photon Pair Production

A single VHE photon can also produce an electron positron pair in the presence of a strong magnetic field by interactions with virtual photons. The process was first described by Klepikov in 1954 and probably only occurs in astrophysical locations. The threshold energy for this process is $2m_ec^2/\sin\theta$ for a photon whose momentum makes an angle θ with the magnetic field. A complicated function of E_γ and B describes the cross-section, which is peaked where different states of the electron-positron pair are created [60]. Components of magnetic fields, perpendicular to the gamma ray momentum, greater than 10^6G are needed to produce electron-positron pairs from photons of TeV energies.

1.4 Particle Acceleration Methods

The previous sections showed how VHE photons could be produced through the acceleration of charged particles. In this section some mechanisms of accelerating charged particles to energies where VHE photons could be produced are discussed.

1.4.1 Dynamo Mechanism

The motion of a conductor in a magnetic field, such as in a generator, induces an electric field, $\vec{E} = \vec{v} \times \vec{B}$. If a magnetic field moves through a highly conducting plasma the net induced field will be zero unless there are regions within the plasma of significantly different charge density. Large potential differences may develop across such regions and allow the acceleration of charged particles to high energies. The existence of vacuum gaps in the plasma surrounding a magnetised, spinning neutron star have been postulated as sources of high energy photons and are discussed later.

1.4.2 Second Order Fermi Acceleration

Second Order Fermi Acceleration was proposed by Fermi in 1949. It is a statistical method of gaining a net increase in the energies of a population of relativistic particles through collisions with 'magnetic mirrors' in the interstellar medium. The magnetic mirrors are associated with irregularities in the Galactic magnetic field and assumed to move randomly with a velocity V. The probability that a relativistic particle of velocity v will collide head on with the magnetic mirror is $v + V\cos\theta$, with the collision assumed to be perfectly elastic. Similarly the probability of a following collision is $v - V\cos\theta$. Hence it is more likely that a particle will gain energy in a head on collision than lose energy in a following collision. The average fractional gain in particle energy is dependent on the the quantity $(V/c)^2$,

$$\frac{\Delta E}{E} = \frac{8}{3}\left(\frac{V}{c}\right)^2 . \tag{1.5}$$

A more detailed explanation of the above expression can be found in [108].

This model of particle acceleration results in a power law spectrum if each particle remains in the accelerating region for a fixed time before being lost, with the total number of particles in the population held constant. However, the process does not account for the observed cosmic ray spectrum at Earth; irregularities in our galaxy's magnetic field move relatively slowly, $V \sim 10^{-4}c$, and collisions between them and cosmic rays are too infrequent to accelerate particles at a reasonable rate. Ionisation losses by the particles have not been considered and would mean that the particles would need to be injected into the accelerating region at high energies, or in a short time scale, to ensure the required particle acceleration by this method. The second order Fermi process may be a more effective model of particle acceleration in areas, such as young supernovae remnants and accretion discs, where there is lots of turbulent plasma motion on a small scale and strong local sources of high energy particles.

1.4.3 First Order Fermi Acceleration

The second order Fermi acceleration process is clearly limited by the fact that, although rarer, following collisions are possible and decelerate the particles. A more efficient mechanism of high energy particle acceleration is the first order Fermi process, where only accelerating head on collisions occur. This is possible in regions where there exists a flux of high energy particles and a shock wave formed by matter expanding into a medium at a speed faster than the speed of sound in that medium. Examples of such locations are found where a supernova explosion is expanding into space or in the relativistic jets of active galactic nuclei.

A flux of very high energy particles will be present both in front of and behind the expanding shockwave and will be isotropically mixed, with respect to the gas on the same side of the shock. Turbulence caused by the explosion upstream of the shock and irregularities in the interstellar medium downstream of it will ensure the random scattering of the particles. The particles can pass through the shock without interacting with it if their energies are high enough so that their gyro radii are larger than the thickness of the shock.

Consider the situation in the frame of reference of the shock, moving with supersonic speed U (figure 1.6a). Upstream gas, of density ρ_1, moves into the shock at velocity $v_1 = U$ and leaves at v_2, ρ_2. Fluid dynamics requires that mass is conserved through the shock, so $\rho_1 v_2 = \rho_2 v_1$, and $\rho_2/\rho_1 = (\gamma+1)/(\gamma-1)$ where $\gamma = 5/3$ is the specific heat for a fully ionised gas. Hence $v_2 = \frac{1}{4}U$. Changing the frame of reference to that of the particles ahead of the shock it is possible to see that the gas behind the shock is advancing towards the particles at $v = |v_2 - U|$ (figure 1.6b). Therefore a particle crossing the shock will be moving relative to the gas behind the shock with a velocity $V = \frac{3}{4}U$ and will have gained a small amount of energy ΔE. The attractive part of this model is that by changing the frame of reference again and considering the particles behind the shock one can see that the same gain in energy is available for particles traversing the shock (figure 1.6c). Every time a particle crosses the shock front, from either side, it will gain energy (figure 1.6d). There are no following collisions as there were with the second order Fermi mechanism.

The Lorentz transform for a relativistic particle, with momentum p, crossing the non-relativistic ($\gamma = 1$) shock front at an angle θ gives the particles energy, E', where

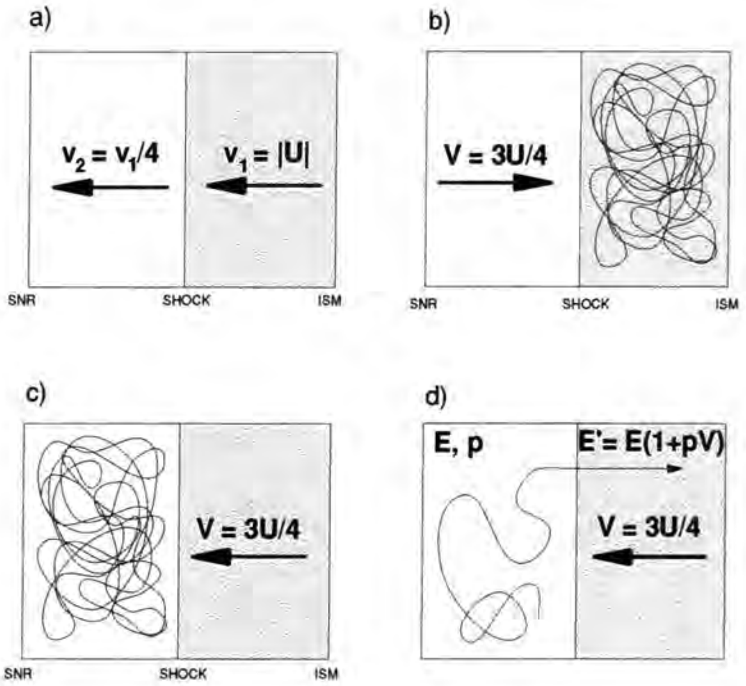

Figure 1.6: The first order Fermi acceleration method in the region of a strong supernova shock expanding into the interstellar medium with velocity U. a) In the frame of reference of the shock, the upstream gas approaches the shock at velocity $v_1 = U$ and leaves at $v_2 = U/4$ since mass flow rate through the shock is conserved. b) The gas behind the shock front moves towards the interstellar gas at a relative velocity $V = 3U/4$. The particles in this frame of reference are assumed isotropically mixed by elastic scattering with irregularities in the ISM. c) The same as b) applies with reference to the gas behind the shock. Particles behind the shock are isotropically scattered by turbulence in the gas. d) A particle of momentum p from either side of the shock experiences a net gain in energy, $\Delta E \sim pV$ each time it crosses the shock front. The fractional gain in energy is proportional to the first order in the quantity V/c (after Longair 1997).

$$E' = \gamma_L(E + pV\cos\theta), \tag{1.6}$$

The average energy increase for particles crossing the shock in the range $0 < \theta\pi/2$ is proportional to the first order of the quantity V/c

$$\left\langle \frac{\Delta E}{E} \right\rangle = \frac{2}{3}\frac{V}{c}. \tag{1.7}$$

The increase in energy is slow; depending on the velocity of the shockfront each particle will gain a few % of energy per crossing and the accelerative phase of a supernova may only last $\sim 10^5$years. There is also a limit to the maximum energy obtainable by this method which does not account for the observations of the highest energy cosmic rays. However this is still a considerably better rate of acceleration than would be obtained by the second order Fermi process. The particles ahead of the advancing shock are swept forward by it and some escape from the accelerating region in the vicinity of the shock front. This leads to a power law energy spectrum with a well defined differential spectral energy distribution of $N(E)dE \propto E^{-2}dE$ [108].

1.5 Fundamental Physics with TeV Observations

The primary interest in observing TeV gamma ray sources has been to investigate the origins of cosmic rays. Several other interesting measurements are possible by observing astrophysical sources in the VHE region of the electromagnetic spectrum [127], [30].

The cosmic microwave background radiation (CMBR) is strongly linked to the epoch of star formation in the early Universe and extends into the infra-red. VHE gamma rays can be absorbed, by the pair production interaction, in a field of infra-red (IR) photons. The detection of extragalactic TeV sources has allowed an upper limit to be placed on the density of the IR background in the wavelength range $1 - 30\mu$m [15], [69]. The limit set by this method is at least two orders of magnitude more restrictive than that capable by direct measurements in the same wavelength range and has allowed estimations of primordial neutrino decay times. Accurate measurements of the energy spectra of extragalactic gamma ray sources would be necessary to further tie down the intergalactic IR photon density. It will be shown in later chapters that the spectral energy distribution (SED) of gamma ray sources often follow a power law. Theoretical estimates suggest that the VHE gamma ray emission of objects at redshift, $z \approx 0.03$, will depart significantly from a power law at ~10 - 20TeV [146].

Observations of variable TeV sources can be used to constrain E_{QG}, the energy scale at which quantum gravity couples to electromagnetic radiation. A gravitational medium containing quantum fluctuations causes a dispersive effect on high energy photons travelling through it. In the formulation of Amelino-Camelia et al. [5];

$$\Delta t \approx \xi \frac{EL}{E_{QG}c} \tag{1.8}$$

where Δt is the time delay relative to the energy independent speed of light, c; E is the energy of the observed radiation; L is the distance the radiation has travelled to the observer and ξ is a model dependant factor ≈ 1. Theoretical work in string theory have suggested that E_{QG} could be as low as 10^{16}GeV [164].

Recent measurements of a strong flare of TeV emission from the active galaxy Markarian 421 have suggested that E_{QG} is at least 4× larger than the theoretical lower limit [16]. The constraint on E_{QG} could become considerably stricter given future, more sensitive, observations of other TeV emitting objects.

Observations of VHE gamma rays may also be a good probe for the cold dark matter (CDM) required to explain galactic rotation. A good candidate for the 'missing mass' in many cosmological models are the stable supersymmetric particles, the lightest of which is the 'neutralino', χ. Results from particle accelerators and cosmological restraints limit the neutralino's mass, m_χ, to 30GeV - 3TeV. A monoenergetic spectral line of emission should be observed, via the annihilation channels $\chi \rightarrow \gamma + \gamma$ and $\chi \rightarrow \gamma + Z_o$, from areas where neutralinos are expected to be numerous. Theoretical studies have suggested that observations of the Galactic Centre with sensitive VHE gamma ray detectors could detect the annihilation line emission [10]. This would allow a more accurate estimation of m_χ and could constrain cosmological models by estimating the amount of CDM in the Galaxy.

Chapter 2

ASTRONOMICAL SOURCES OF VHE PHOTONS

Recent exciting results in VHE astronomy have been the discovery of VHE gamma ray emission from Active Galactic Nuclei (AGN). These objects have been observed to be highly variable in their activity displaying short sporadic outbursts of emission in which the flux of VHE photons may increase many fold. Such observations have been made possible by recent developments which have increased the sensitivity and reduced the detection threshold energy of ground based gamma ray detectors.

Early observations at TeV energies concentrated on galactic sources of VHE gamma rays. Several types of galactic object support suitable conditions to accelerate charged particles and therefore produce VHE gamma rays. Possible sources include Isolated Pulsars, X-Ray Binary systems (XRB), Supernova Remnants (SNR) and Plerions (the nebula of a recent supernovae containing a population of high energy particles). All of these objects have involved the supernova explosions of dying stars. It was postulated that if spinning neutron stars existed in these objects then the VHE emission might be emitted in regular pulses at the pulsar period. By employing accurate event timing in these early observations it was possible to gain increased sensitivity to gamma rays by looking for regular pulses in the signal.

2.1 Active Galactic Nuclei

Galaxies whose total luminosity is dominated by non-thermal processes are known as 'Active Galaxies'. Their observed luminosities are much larger than can be accounted for by the thermal emission of the stars within the galaxy. The power source responsible for driving the non-thermal processes, which result in the emission of photons over many decades of the electromagnetic spectrum, is thought to be the accretion of matter onto a central, supermassive black hole ($\sim 10^8 M_\odot$) [139]. The black hole at the centre of an active galaxy is known as an Active Galactic Nucleus (AGN). Large numbers of classifications exist for objects with an AGN based on their spectra, flux variability at different wavelengths and the presence of emission lines. One group of objects which are particularly important in the field of gamma ray astronomy are the 'blazars', also known as the flat spectrum radio-loud quasars (FSRQs). Unlike most quasars, blazars are powerful radio sources that exhibit a continuum of emission that has been measured from radio frequencies up to VHE gamma rays. Blazars are also characterised by high luminosity ($> 10^{45}$ ergs/s at most wavelengths), extreme flux variability and high optical polarisation. Figure 2.1 shows the average spectral energy distributions (SED) of a selection of blazars. All of the SEDs shown exhibit the distinctive double peaks which are typical of blazars [67]. The exact location and spacing of the peaks varies from object to object with the first peak and second peaks

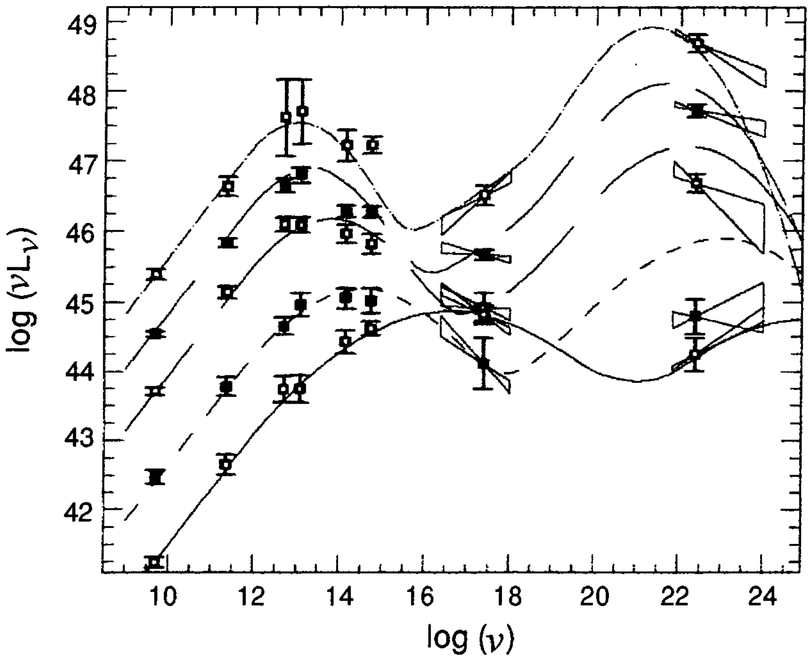

Figure 2.1: Average SEDs for a group of blazars binned according to their radio luminosities (from Fossati et al. 1998).

appearing anywhere in the infra-red to soft X-ray and X-ray to hard gamma ray regions respectively. Blazars also undergo violent periods of flux variability in many regions of their spectra which may last for periods as short as hours up to a few days. The short timescale and luminosity of the flux variations, or 'flares', has lead to the the conclusion that the emission from blazars is due to non-thermal processes in a relativistic jet of electrons ejected from the AGN. Shock fronts formed by the plasma in the jets are able to accelerate a population of electrons to very high energies by the mechanisms discussed in section 1.4. The processes at work in the jet are linked; multi-wavelength observations made when blazars are flaring have detected correlations between the flux increases at different energies [18], [75], [155]. Figure 2.2 shows the light curves of observations of the blazar

Markarian 501 made between 8-19 April 1997 during such a flare [28]. There are clear similarities between the light curves at different energies although the fractional increase in amplitude of emission is much greater in the VHE range than it is at any other. The SED of the observations is shown in figure 2.3 compared against archival data from other years. There are increases in flux at all photon energies with a steady increase in the VHE flux, by a factor of ~10, from 1995 up to the peak of the 1997 flare.

The similarities in the light curves at different wavelengths suggest that the same electrons in the jets are responsible for the whole SED. The electrons in the relativistic jet emit synchrotron radiation in the strong magnetic fields which are present. Since relativistically emitted synchrotron radiation is strongly beamed in the forward direction it is likely that blazars are only observed when the jets are aligned very closely with the observer's line of sight. The first peak in a blazar SED is often referred to as the 'synchrotron' peak since the emission here is well described by this process.

The second peak in the observed blazar SEDs has a very similar shape to the synchrotron peak. Together with the correlated variability observed at different wavelengths this suggests that the same population of electrons is responsible for the x-ray/gamma ray emission. Synchrotron Self Compton models (SSC) are able to describe the SEDs of blazars with reasonable success. In these models the synchrotron photons can be boosted to higher energies, via the inverse Compton effect, by the same relativistic electrons which produced them.

TeV emission is expected to be strongest from blazars with their synchrotron peak in the X-ray region. A subset of blazars which have been identified as good candidates for TeV emission are the X-ray selected BL Lacertae (XBL)

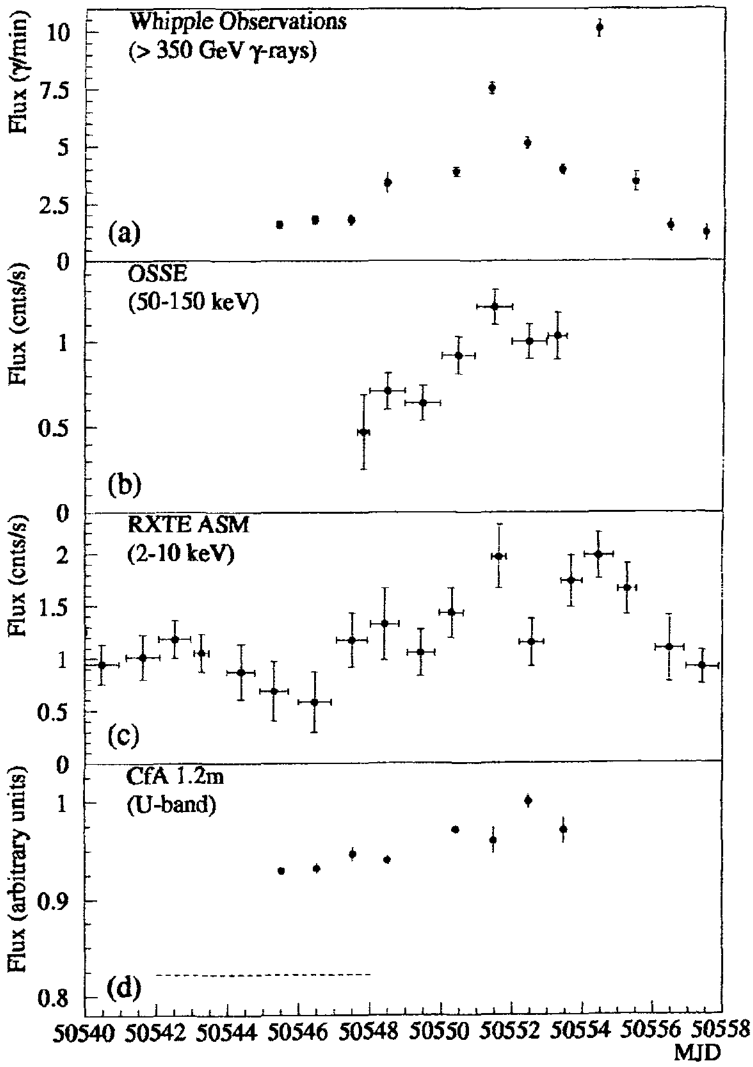

Figure 2.2: a) VHE gamma ray, b) OSSE 50keV-150keV, c) ASM 2-10keV and d) U-band optical light curves of Mrk 501 for the period 2 April (MJD 50540) to 20 April 1997 (MJD 50558). The dashed line in d) indicates the average U-band flux in March 1997 (from Catanese et al. 1997).

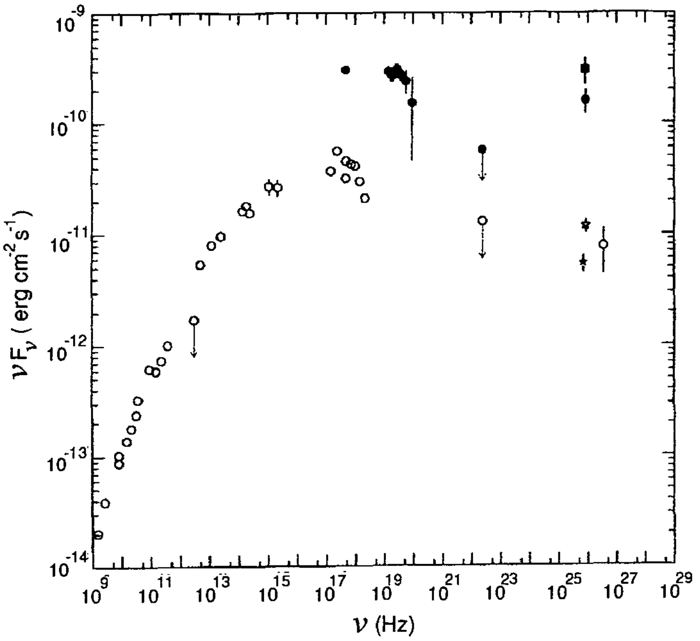

Figure 2.3: The spectral energy distribution of Mrk 501 during a flare (taken from Catanese et al. 1997). Shown are the contemporaneous observations taken as part of a multi-wavelength campaign between 9-15 April 1997 (filled circle), the mean VHE gamma ray fluxes in 1995 (upper star), 1996 (lower star) and the peak VHE emission during the flare (filled square). For more details on the origins of the archival flux measurements (open circles) see the Catanese et al. paper.

objects. BL Lacertae objects are named after the first object discovered in the class, initially thought to be a variable *galactic* radio source with an extremely smooth synchrotron spectrum. Initially the objects were interesting as their spectra showed no emission or absorption lines. Recent more sensitive measurements have shown that this is not the case (most notably in BL Lacertae itself ! [18]) and indicates the presence of clouds of gas separated from the jet. The clouds of gas are known as 'broad line regions' and are responsible for the absorption of

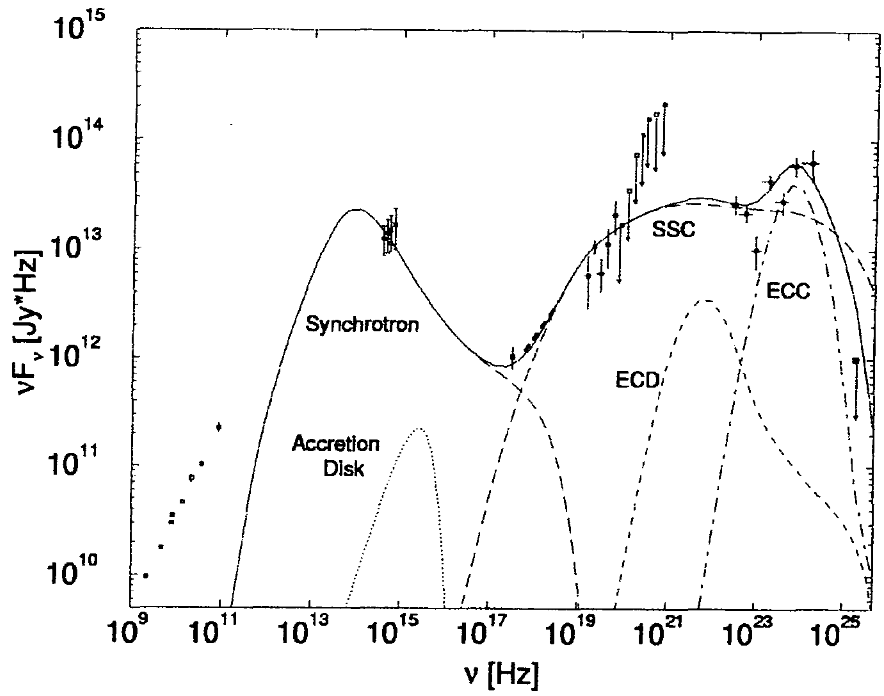

Figure 2.4: A fit to the SED of BL Lacertae with an external SSC model, including external Compton contributions of photons from an accretion disk (ECD) and clouds (ECC) (from Böttcher and Bloom 1998).

photons from the accretion disk and the emission of atomic transition lines such as L_α. Modifications to the SSC models of BL Lacertae objects include contributions by external sources of photons which are scattered into the jet and alter the inverse Compton emission (see figure 2.4). It is interesting to note that all four of the currently detected extragalactic TeV sources (Mrk 501 [134], Mrk421 [132], 1ES2344 [29] and PKS2155 [40]) are all XBLs.

2.2 Isolated Pulsars

Since their discovery in 1967 [82] close to 600 pulsars have been discovered, usually through the detection of pulsed radio emission. The emission is extremely regular with pulse periods ranging from a few milliseconds to a few seconds. Seven Pulsars have been identified by the CGRO satellite to be emitting pulses of gamma rays, three of which are sources of unpulsed TeV photons; the Crab, Vela and PSR1706-44.

A pulsar consists of a spinning neutron star in a 'magnetosphere', the region of space dominated by the neutron star's strong ($\sim 10^{12}$G) magnetic field, shown in figure 2.5. The magnetosphere is highly conductive along, but not perpendicular to, the magnetic field lines. The magnetic and rotational axes of the pulsar are not necessarily aligned and hence the rotating dipole causes the emission of an electromagnetic wave at the pulsar period. This is the major source of energy loss from the pulsar which is confirmed as all isolated pulsars are observed to be gradually increasing their pulsation periods, radiating away their rotational energy. The magnetic field corotates with the neutron star out to a radius, r_c, from the spin axis beyond which the velocity of rotation exceeds the speed of light. This radius defines the 'light cylinder' within which the magnetic field lines are closed and contain electrons and ions drawn from the surface of the neutron star by strong electric fields. The net charge density in the magnetosphere has the opposite sign as the scalar product of the rotation and magnetic field vectors, $\vec{\Omega} \cdot \vec{B}$ [109]. The equatorial and polar regions of the pulsar are separated by a line joining the points where $\vec{\Omega} \cdot \vec{B} = 0$, the 'null charge surface', and are populated by opposite signs of net charge.

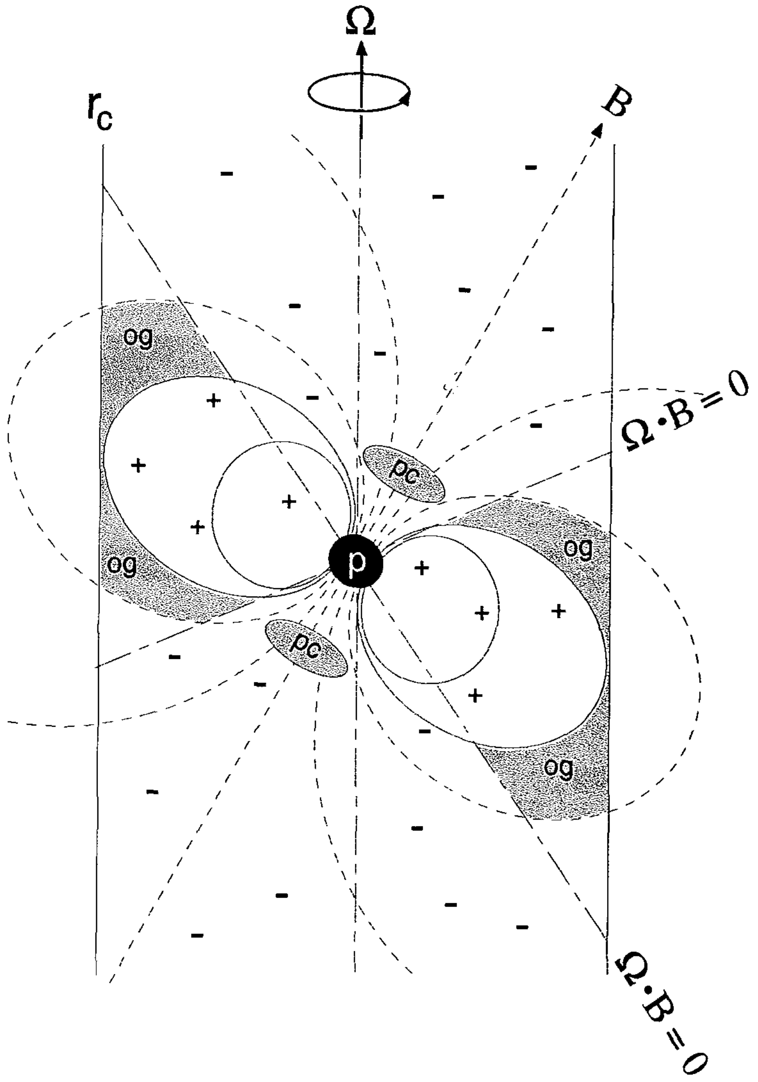

Figure 2.5: The geometry of a pulsar magnetosphere showing the closed (solid) and open (dashed) magnetic field lines. Charge separation occurs either side of the null charge surfaces (dot dashed), where the instantaneous magnetic field and rotation vectors are orthogonal. The shaded areas show the outer gap (og) and polar cap (pc) regions where particle acceleration may take place.

2.2.1 Polar Caps and Outer Gaps

The circular region at the poles of a pulsar that is defined by the last closed field lines is known as the 'polar cap' [109]. Streams of electrons are constrained to move along the open field lines above the polar cap in a beam a few degrees wide and it is these electrons which produce the observed radio pulses. The pulsar can be thought of as a lighthouse with a pulse of synchrotron radio radiation detected when the rotating beam crosses an observer's line of sight. The energies of the emitted photons will depend on the magnetic field strengths and hence radio photons originate high above the surface of the star with optical and higher energy photons originating from lower down in the magnetosphere. Gamma rays may also be emitted by the curvature radiation process nearer to the stellar surface although it is unlikely that this is a source of VHE gamma rays; positrons or electrons from pairs created at higher altitudes in the polar cap will fall back down to the surface of the star producing a gamma ray opaque field of lower energy thermal photons.

The 'outer magnetospheric gaps' occur near the light cylinder radius and are bounded by the null charge surface and the last closed field line. The existence of such gaps requires that the pulsar has a combination of large magnetic field and short spin period and may be almost any size depending on the field strength and alignment of spin and magnetic axes. The potential drop along $\vec{B}$ maybe as large as 10^{15}V in the Crab and Vela pulsars.

The model of Cheng, Ho and Ruderman [44], [45] allows for pulsed emission of photons from IR to gamma ray energies. Gamma rays created lower in the magnetosphere can traverse the gap and may interact with a transverse component of magnetic field or with lower energy photons to produce electron-positron pairs. Electrons and positrons within the gap are oppositely accelerated along the field lines and produce gamma rays, up to a few GeV, by curvature radiation or inverse Compton scattering with low energy (IR) radiation. It is possible, via secondary emission processes, that a small amount of the gap generated power could be emitted as a spectrum of photons with a maximum energy approaching 10^{12}eV. This flux would be pulsed but may be hard to observe due to absorption by the magnetosphere magnetic field and pair production on IR photons. Periodic TeV emission has been reported from the Vela [11] and Crab pulsars [1], [55] but has not been confirmed by recent more sensitive measurements.

2.3 Plerions

A plerion is a nebula formed by a recent supernova explosion and filled with a population of accelerated charged particles. The source of the particles is a relativistic magnetohydrodynamic (MHD) wind of electrons that emanates from the pulsar surface. A good example of a plerion is the Crab, shown in figure 2.6. The Crab is the result of a supernova explosion, in the year 1054AD, which left behind an expanding shell of matter (the Crab Nebula) and a bright pulsar (the Crab Pulsar). A double peaked light curve from the pulsar has been observed at a pulse period of 33ms over a very large spectral range, from ~100MHz radio to a few GeV. Early VHE observations claimed detections of pulsations [55], or outbursts of pulsations [1], [12], [73]. These measurements have not been confirmed by later, more sensitive experiments.

The first clear steady VHE signal from the Crab nebula was detected by the

Whipple Observatory in 1989 [159]. Since then the Crab nebula has been extensively studied at VHE energies by many Northern Hemisphere groups and found to be a remarkably constant source, within the ±20% accuracy of determining accurate fluxes with current detectors [121]. More recent measurements by the Whipple Observatory have measured the integral flux at energies above 300GeV to be $\sim 8 \times 10^{-11}/\mathrm{cm}^2$ /s of which it is estimated that $< 2.5\%$ is a pulsed component at the 33ms pulsar period [74]. The significance of the source detection in this observation was 23σ based on a total data set of 50hours. The discovery of the Crab as a steady 'standard candle' of VHE gamma rays has proved invaluable in the development and calibration of ground based detectors in the Northern Hemisphere.

The radiation from the Crab nebula comprises an intense synchrotron spectrum seen from radio to gamma ray, shown in figure 2.7. The MHD wind of electrons is confined within the slowly expanding nebula and forms a shock front. Just upstream of the shock it is expected that the ratio of the magnetic to particle energy densities, $\sigma << 1$. The figure shows the results of of a detailed MHD wind model of the SED using different values of σ. The SED is largely explained, at energies up to ~100MeV, by the synchrotron radiation of electrons in the magnetic field at the shock front. At higher energies inverse Compton scattering of the synchrotron electrons with in a field of soft photons is the best fit to the spectrum when $0.003 < \sigma < 0.007$, in agreement with predictions [91]. The fact that the VHE emission is unpulsed supports the hypothesis that it emanates from the nebula.

In addition to the Crab Nebula, the plerion PSR1706-44 has been confirmed as a source of VHE photons [39], [97]. The reported integral flux above 300GeV

Figure 2.6: The Crab Nebula is one of the most observed objects at all wavelengths. The blue/white emission is due to synchrotron emission of electrons ejected from the pulsar in the tangled magnetic fields of the nebula. Thermal (reddish) emission is seen where gas is heated by the radiation from other areas of the nebula (picture obtained from LHEA 1999).

is half that of the Crab, $\sim 4\times 10^{-11}/\mathrm{cm}^2$ /s, and there is no evidence for pulsed emission. The mechanism behind the VHE emission is less clear for PSR1706-44 than it is for the Crab. PSR1706-44 does not have such a bright nebula as the Crab and its pulsar period is much longer at 102ms, meaning a weaker MHD wind. The lack of nebula makes it less likely that the VHE emission is due to a Crab like SSC mechanism. There are, however, some theoretical arguments which suggest that PSR1706-44 may exhibit pulsed VHE emission via an outer gap model [48], [140]. TeV emission has also been reported from the Vela pulsar [166] and the supernovae remnant SN1006 [98] by the CANGAROO group. Measurements by other groups have not confirmed these results (e.g [21], [41]).

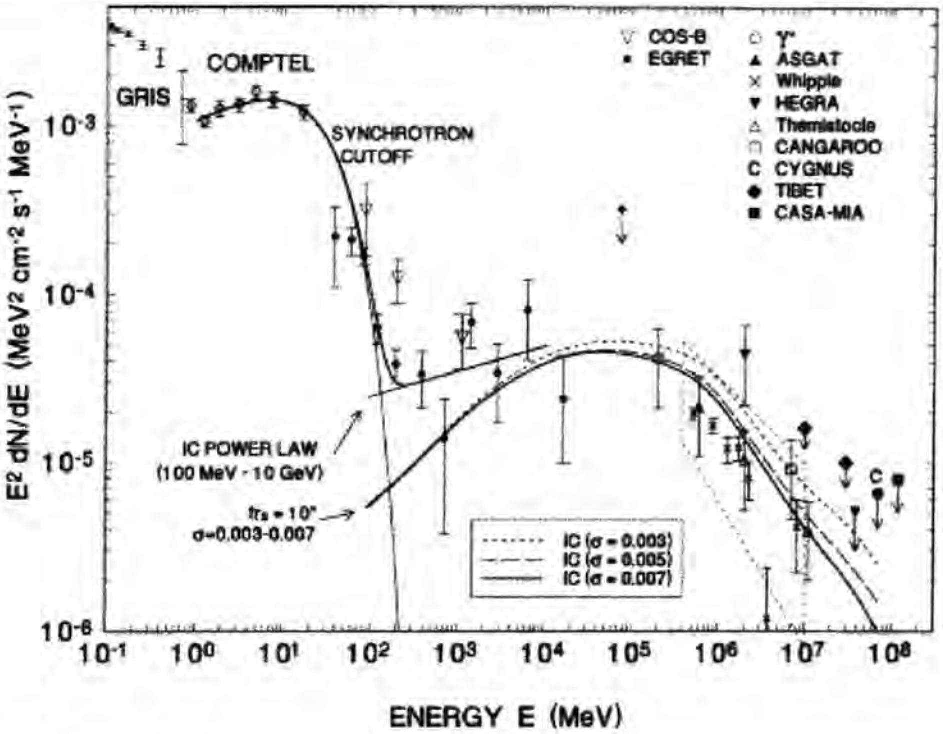

Figure 2.7: The Crab Nebula unpulsed spectrum in terms of E^2 times the differential spectrum. The results from observations at different wavelengths have been fitted with various theoretical models (from de Jager et al. 1996).

2.4 Accreting Binary Systems

Mass transfer between binary systems of a compact object, such as a neutron star or black hole, and a companion main sequence star results in the accretion of matter from the companion onto the compact object. The pulse period of the spinning neutron star in an Accreting Binary System tends to decrease or 'spin-up' with time as angular momentum is transferred to it from the companion. Accretion of matter onto a neutron star is an efficient method of converting the gravitational potential energy of the matter into radiation and can release as much as 10% of the rest mass energy of the accreted matter. Such systems are often bright X-Ray sources and known as 'X-Ray Binary Systems' (XRBs). They exhibit strong pulsed X-Ray emission and often some modulation of that flux due to eclipses of the x-ray source in the binary orbit. The orbital phase of the source is defined with 0 being the major eclipse of the neutron star by the companion, i.e. when the minimum x-ray flux is observed. XRBs may involve either a neutron star or black hole and can be divided into two groups by the mass of the companion star. An excellent description of the different types of XRB is given in [125].

2.4.1 High Mass XRBs

High mass X-Ray binary (HMXRBs) systems involve a late O or early B type star of $M > 10M_{\odot}$ in orbit with a compact object such as a neutron star. The giant star makes up most of the mass of the system. One quarter of the 100 or so brightest galactic X-ray sources are HMXRBs, almost all of which emit periodically pulsed X-rays [108]. The young, giant companion stars of systems such as Vela X-1 have an enlarged stellar atmosphere that fills, or almost fills, its Roche Lobe. These systems have eccentric and relatively wide binary orbits and are unlikely to form permanent accretion disks. They accrete material mainly from the companion star's strong stellar wind, which is also important as a source of matter for the scattering and absorption of X-rays and as a target material for gamma ray production by particle interactions. Stellar wind material does not carry much angular momentum and such systems tend to have long pulsar periods of several hundred seconds. The accreted material is directed along the neutron star magnetic field lines to the poles. A beam of emission is seen when the pole is oriented towards the observer. Low level VHE emission at the 283s pulse period has been reported by the Durham Group [35]. The X-Ray emission from these objects is low, $2 \times 10^{35} - 2 \times 10^{36}$ ergs^{-1}, and sensitive to fluctuations in the stellar wind.

HMXRBs such as Cen X-3, LMC X-4, SMC X-1 differ from wind fed systems as they have closer, very circular orbits with short binary periods, generally <10days. The companion star fills its Roche Lobe allowing a stream of material to escape from the companion through the inner lagrangian point and accrete on to the neutron star via a large accretion disk. The accretion rate is higher than in wind fed systems and the spin-up phenomenon more pronounced with pulsar periods generally <10s. These systems are known as 'disk fed' systems and exhibit bright X-Ray emission with luminosities of $\sim 10^{38}$ergs^{-1} possible. VHE gamma ray emission has recently been observed from the HMXRB Cen X-3 by the Durham group [38].

A further subset of HMXRB are the BeXRBs, so called because their spectra show Be emission lines. Mass transfer in Be/X-ray binary systems is also due, in part, to a stellar wind but includes irregular amounts of matter ejected from the surface of the Be star. This is due to the high rotational velocities of such stars causing matter to be flung off along the equatorial plane. As the compact object moves around the gas giant the stellar wind density varies and the accretion rate may suddenly turn on or off. VHE emission from the BeXRB 4U0115+63 has been detected at the 3.6s pulsar period and seems to be highly sporadic [33], [160].

2.4.2 Low Mass XRBs

The second family of accreting x-ray binary systems are the Low Mass X-Ray Binaries (LMXRB) with evolved companion stars with mass of order $1M_{\odot}$. Mass exchange in LMXRB is due mostly to Roche lobe overflow of the companion as the companions have weak stellar winds. Mass accreted from the companion star slowly spirals onto the neutron star (or in some cases black hole) via a flat accretion disk. The x-ray emission is generally unpulsed since the magnetic field of the neutron star has decayed and the accreted matter is not tightly funnelled onto the poles. Bright LMXRBs are rare when the companion masses are between $2-10M_{\odot}$. Simplistically this is because the rate of mass exchange by Roche Lobe overflow is unstable when both stars in a binary system are of similar masses and continues so quickly that the neutron star becomes engulfed in an x-ray opaque field of matter. HMXRBs only start to appear when the companion mass is $>10\mathrm{M}_{\odot}$ due to their stellar wind strengths and different binary parameters. One exception is Her X-1, a system involving a $2.2M_{\odot}$ late type star and a possible black hole candidate. Her X-1 has been observed at TeV energies [56]. The evolved companions in LMXRBs also means that they are distributed differently in the sky to HMXRBs and tend to be associated with galactic bulge and globular cluster x-ray sources.

2.4.3 Cataclysmic Variable Stars

Cataclysmic variables (CV) are binary systems in which the compact object is a white dwarf (WD) rather than a neutron star and are not as bright as XRBs at X-Ray frequencies. The companion stars are usually late-type stars which transfer matter onto the white dwarf via Roche Lobe overflow and an accretion disk. The optical and UV emission can be highly variable and in some systems, in which the companion star is a dwarf star, the accretion disk is bright enough to be observed directly. Outbursts of periodic pulsed VHE gamma ray emission have been observed from the CV AE Aquarii indicating particle acceleration at locations tied to the rotating WD during periods of enhanced accretion [19], [115].

2.4.4 Models of TeV Emission from Accreting Binary Objects

Models of gamma ray emission from isolated pulsars and plerions concentrate on accelerated electrons as the source of the VHE photons. The VHE emission from accreting binary systems is most likely due to the decay of π^o particles produced in the interactions of a beam of accelerated protons (or ions) with a target material or background radiation. Electrons are not favoured in these models because their acceleration is curtailed by inverse Compton scattering in the fields of intense X-rays in regions surrounding accreting neutron stars. The exact location of the target material may differ from object to object and lead to variable emission at different phases in the binary orbit. A few examples are shown in figure 2.8, but for a full review see [119].

At present there is not a clear theoretical understanding of how the protons are accelerated to the ultra high energies required, largely due to the small numbers of observed sources. Some binary systems could produce large potential differences or shocks across which particles could be accelerated (e.g. [99]). Models such as that of Cheng and Ruderman suggest that large charge separated

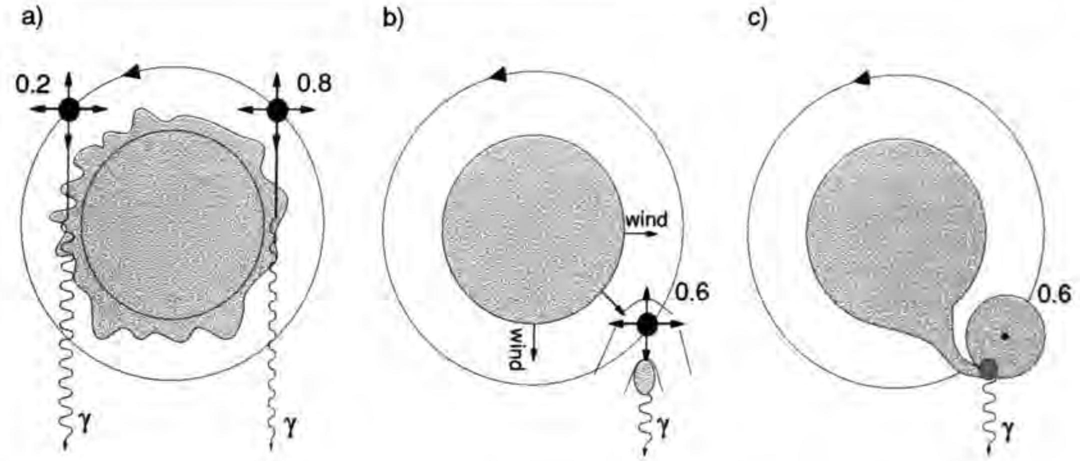

Figure 2.8: Possible phases of emission of VHE gamma ray in binary systems when the target material is a) the companion's stellar atmosphere, b) an accretion wake is formed in a stellar wind, c) a structure attached to an accretion disk (from Hillas 1987).

gaps with potential drops of up to 10^{16}V are possible where there is differential rotation across the accretion disk, [46], [47]. The simplified model considers the magnetosphere in two parts; the inner part which corotates with the neutron star and the outer part rotating with the disk (figure 2.9). A gap, similar to those in the outer gap models of isolated pulsars, separates the two regions and protons or ions can be accelerated along the gap at ultra-high energies towards the disk. Pionisation occurs in proton collisions with matter within the accretion disk producing TeV gamma rays by decay of the π^o particles. Where the pulsar spin and magnetic axes are not aligned the angle of attack of the proton beam with the accretion disk will vary and may lead to periodic emission of photons when the resulting precessing gamma ray beam crosses the observer's line of sight.

Present objects of interest are the galactic microquasars, a sub class of XRBs

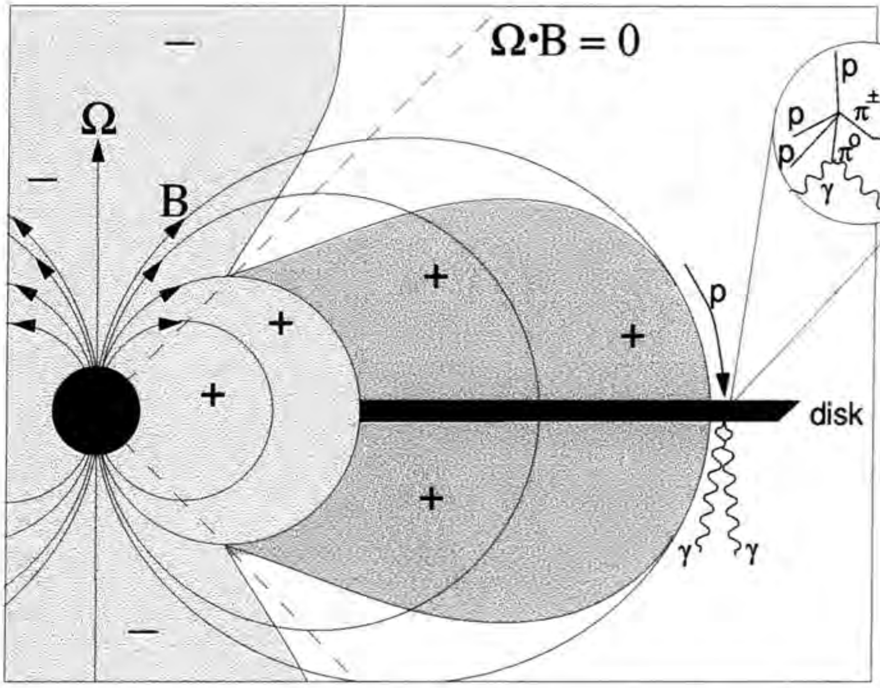

Figure 2.9: The accreting neutron star model of Cheng and Ruderman (1989). The inner (light shaded) region corotates with the neutron star while the outer (dark shaded) region has the same rotation as the accretion disk. Protons are accelerated across the vacuum gap and interact with the accretion disk to produce gamma rays via π^o decay.

containing a black hole, an accretion disk and collimated relativistic jets along the rotational axis of the black hole. As such these objects are analogous to AGN, but on a smaller scale. One such object, GRS1915+105, is predicted to emit a detectable VHE flux during sporadic flares [7].

Chapter 3

PRODUCTION OF CHERENKOV RADIATION IN THE ATMOSPHERE

3.1 Introduction

The atmosphere of the Earth is a very effective barrier against photons from Ultra-Violet (UV) and higher energies. Hence astronomy in this region of the electromagnetic spectrum has been confined largely to observations at high altitude or in space. At gamma ray energies below a few GeV satellite experiments have been used to great effect to investigate the sky. The most notable of these has been the Compton Gamma Ray Observatory (CGRO), at 2000kg one of the largest satellites ever launched. The CGRO contains four experiments capable of detecting photons with energies between 15keV and ~3GeV . These are the Oriented Scintillation Spectroscopy Experiment (OSSE – 0.5 - 10MeV) [27], the Burst and Transient Source Experiment (BATSE – 30 - 1900keV) [65], the Compton Telescope (COMPTEL – 0.8 - 30MeV) [80] and the Energetic Gamma Ray Experiment (EGRET – 30MeV - 30GeV) [78], [151].

Above EGRET's energy range, the size (and therefore cost) of experiment needed to collect the low fluxes of increasingly penetrating gamma rays becomes prohibitive. Gamma rays above ~100GeV interact with particles in the upper atmosphere to produce cascades of electrons and positrons known as Extensive Air Showers (EAS). Secondary optical radiation is emitted by the EAS which can be detected at ground level by large detectors. This method of observing VHE gamma ray sources is known as the Atmospheric Cherenkov Technique (ACT). The development of the ACT has required a careful understanding of EAS development and Cherenkov photon production. A very useful tool for this has been the computer modelling of EAS using numerical 'Monte-Carlo' techniques.

3.1.1 Monte-Carlo Simulations of EAS

The Monte Carlo method has been used to create model data in high energy particle physics since the 60s and is described in detail elsewhere (see, for example [2], [129]). It is a numerical method of simulating events that occur and interact randomly, but with known probability distributions. For simulating EAS the cross-sections and probability distributions for the various particle interactions at work are well known. The fate of individual particles within an EAS can be decided by drawing random numbers from the probability distributions of the appropriate particle interactions, i.e whether a particle decays or interacts with another particle, is deflected and by how much, loses energy etc. By repeating the simulation many times a distribution of simulated EASs can be produced which accurately reflect observations.

Simulating data for an Atmospheric Cherenkov Telescope involves two parts:

1. The creation by a primary particle of an EAS in the atmosphere and the

subsequent emission and transmission to ground level of Cherenkov photons.

2. The response of a model telescope to those photons and the recording of a simulated Cherenkov event.

The early chapters of this thesis are primarily interested in the development of EAS in the atmosphere and the ground level distribution of Cherenkov photons. Different sets of computer code are available for this and generally available by contacting their authors. These include MOCCA [83], which includes the hadronic event generator SIBYLL [66], and CORSIKA [101]. The Monte carlo code used for the simulations of events in this thesis has been adapted from the 'GENESIS52' code written by K.J.Orford at the University of Durham. To reduce computing time all of these codes use an 'atmosphere slicing' method of simulation. Rather than following individual particles all the way through the atmosphere, particle interactions are calculated after a small 'slice' of atmosphere (generally $1g/cm^2$ thick) has been traversed. Comparisons of the Cherenkov photon yields and lateral distribution of particles from the simulated EAS shows broad agreement between the codes [130].

Creating a telescope model requires accurately simulated showers and a good understanding of the detector to be modelled. The GENESIS simulations are used in various models of the Durham University Mk6 telescope in chapters 7 and 8. It will be shown that hadronic events simulated by these methods are in good agreement with the observations in section 8.3.

3.2 Extensive Air Showers

When a high energy cosmic photon or nucleon interacts in the atmosphere it can initiate a cascade of many other particles which travel towards the ground. These cascades of particles are known as Extensive Air Showers (EAS). There are differences between EAS initiated by gamma rays and hadrons, which are shown in the following sections of this chapter. The 'core' of an EAS is often defined as an axis from the top of the atmosphere to ground level along which the primary particle would have travelled if it retained its initial direction. EAS can extend for many km into the atmosphere producing particles several hundreds of metres away from the core at sea level.

3.2.1 Gamma Ray EAS

An extraterrestrial gamma ray photon arriving at Earth has a finite probability of undergoing the pair-production process when in the Coulomb field of an atmospheric atom, X;

$$\gamma + X \longrightarrow X + e^- + e^+. \tag{3.1}$$

For electrons produced with kinetic energies above 84MeV the dominant energy loss process is bremsstrahlung;

$$e + X \longrightarrow X + e + \gamma \tag{3.2}$$

where an electron is deflected by the field of a nucleus and loses energy which is released as a high energy gamma photon. The gamma ray is then available to produce more electron positron pairs which produce more gamma rays and so on, leading to a cascade of increasing numbers of particles in the atmosphere. The EAS is purely electromagnetic in nature, consisting entirely of electrons, positrons and gamma rays. Photonuclear interactions, producing kaons and pions, are possible but the probability of this relative to pair production is $\sim 10^{-3}$. Each interaction takes a fraction of the energy of its primary particle and so the energy per particle in the shower decreases as the numbers of particles rise. The maximum number of particles within the shower is reached when the energy of the particles reaches the 'critical energy' for air, 84MeV. Below this energy ionisation, described by the Bethe-Bloch equation (given in many texts, e.g. [167]), takes over from bremsstrahlung as the dominant energy loss mechanism for the electrons. Ionisation is a more severe energy loss process than bremsstrahlung; the electrons in the cascade lose energy quickly and the number of gamma ray photons produced in bremsstrahlung interactions is reduced. In addition the cross-section for pair production falls until Compton scattering and photoelectric absorption are the dominant energy loss mechanisms for gamma rays and the cascade stops growing.

The radiation length in a material is defined as the mean distance travelled in which a high energy particle loses all but $1/e$ of its energy [2]. For a high energy electron undergoing bremsstrahlung in air this is approximately 37g/cm^2 . Simple models to describe the development of electromagnetic EAS in the atmosphere have been proposed [4]. A schematic of such a model is shown in figure 3.1. The model assumes that the radiation length for bremsstrahlung is approximately the same as the interaction length for pair production and defines a 'cascade length', $X_o = 37\text{g/cm}^2$, to describe both interactions.

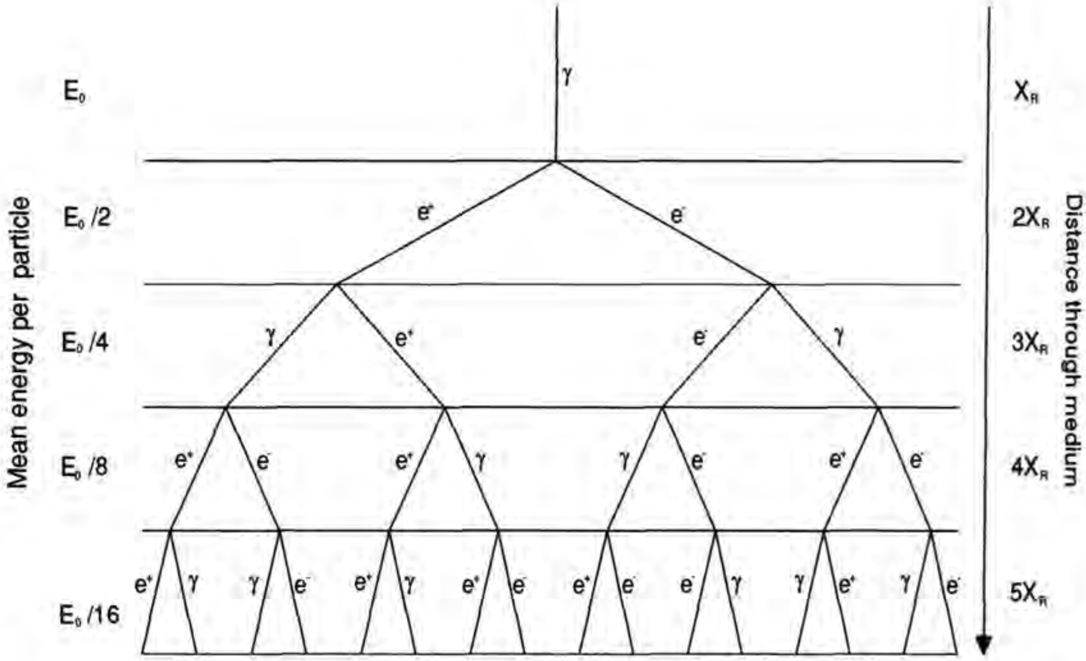

Figure 3.1: A toy model of gamma ray EAS (after Longair 97).

In this model the probability of an electron undergoing bremsstrahlung or a photon pair producing is 50% at some depth X into the atmosphere where

$$\exp -(X/X_o) = \frac{1}{2}, \tag{3.3}$$

If we assume that the total energy of the shower is conserved then the mean particle energy halves after each cascade length. The average particle energy, $\langle E \rangle$, of the particles after n interactions is given by

$$\langle E \rangle = \frac{E_o}{2^n} \tag{3.4}$$

where E_o is the energy of the primary gamma ray. In this model the number of particles in the shower will continue to double with every interaction length but in reality the shower will eventually reach a maximum and die out at the critical particle energy, $E_c \approx 80\text{MeV}$. The maximum number of particles, $N \approx E_o/E_c$, occurs at a particular depth in the atmosphere known as the depth of maximum, X_{max}, and can be estimated by

$$X_{max} \approx X_o \ln\left(\frac{E_o}{E_c}\right). \tag{3.5}$$

For primary gamma rays in the hundreds of GeV range $X_{max} \approx 300\text{g/cm}^2$. Assuming that the density of the Earth's atmosphere decreases exponentially, with an e folding height of ~7km and a total depth of 1000g/cm^2, then X_{max} should occur at ~7km above sea level. In reality the actual heights of maximum will be at a somewhat higher altitude as the electrons in the shower undergo some continual energy loss by ionisation of the atmosphere. A Monte-Carlo simulation of a gamma ray EAS is shown in figure 3.2.

The lateral spread of particles is dominated by Coulomb scattering of the electrons in the atmosphere which is larger than the opening angles of pair production and bremsstrahlung. For multiple Coulomb scattering the mean angle that an electron travelling δx g/cm^2 will be scattered is given by [70]

$$\langle \delta\theta^2 \rangle \approx \left(\frac{21\text{MeV}}{E}\right)^2 \delta x. \tag{3.6}$$

The angles an electron is scattered by can be approximated by a gaussian distribution with width= $\sqrt{\langle \delta\theta^2 \rangle}$. For an 80 MeV electron travelling through 37g/cm^2 of atmosphere the angular spread is $\sim\pm 12°$. The lateral spread of low energy (80MeV) particles in a shower is given by the Moliere unit, r_1,

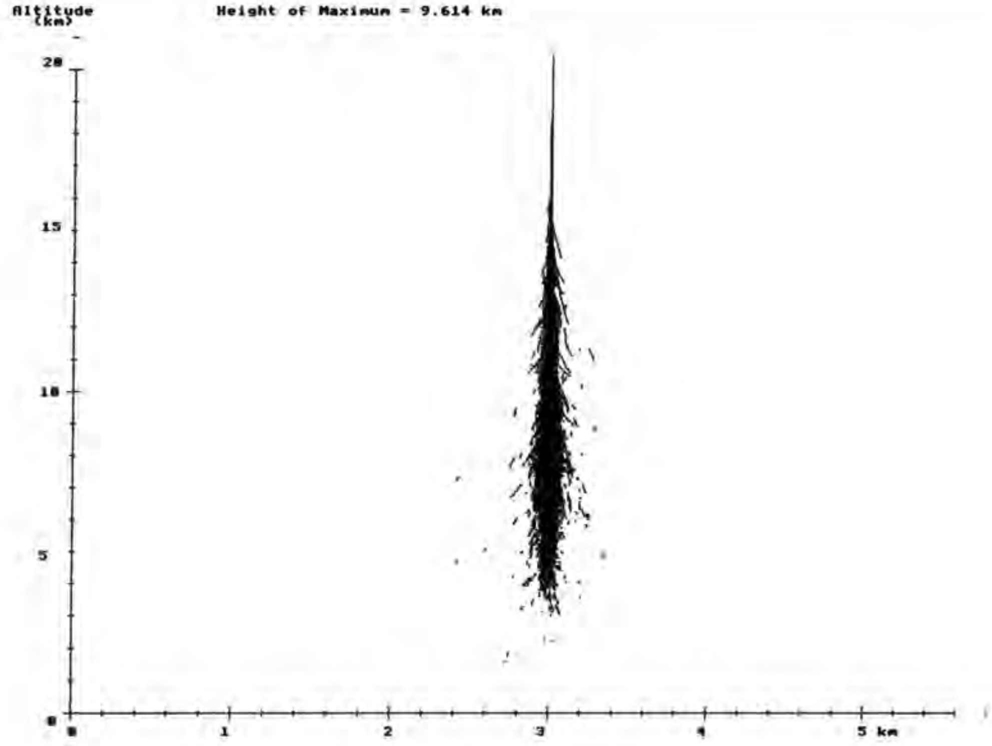

Figure 3.2: The simulated development of a 300GeV gamma ray EAS. Shown are the tracks of electrons and positrons with energies above 21MeV.

$$r_1 \approx \frac{21}{80} X_o \approx 9.3\mathrm{g/cm}^2, \tag{3.7}$$

which is approximately 80m at sea level. For higher energy particles the characteristic spread is smaller by a factor of 80MeV/E.

3.2.2 Hadronic EAS

The elemental composition of the isotropic flux of cosmic ray nuclei incident at Earth is shown in figure 3.3. Roughly 90% of the cosmic-ray background flux is

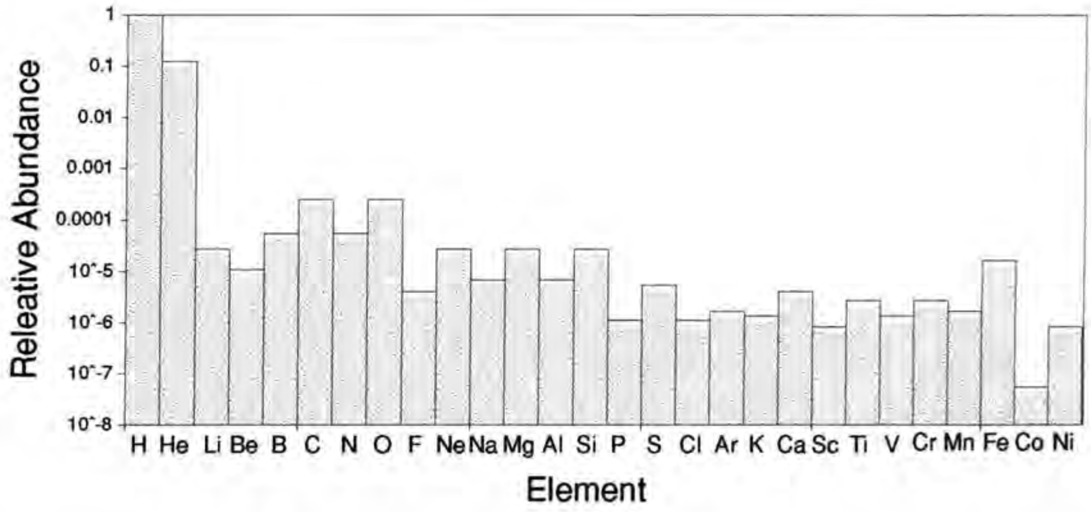

Figure 3.3: The composition of cosmic rays incident at the top of the atmosphere (from Longair 97).

protons, the rest being mostly ^4He nuclei with traces of heavier elements.

Neutrons are not expected to reach Earth from cosmic sources since their decay lifetime is only ~10^3s and it is difficult to see how large numbers of neutral particles could be accelerated directly to high energies. For a neutron to survive the journey to Earth from the Galactic Centre would require $\gamma \approx 10^9$, i.e. acceleration to ~10^{18}eV of kinetic energy. Like gamma rays a cosmic-ray proton (or nucleus) produces cascades of particles in the atmosphere, a sketch of which is shown in figure 3.4.

An EAS initiated by a cosmic ray proton starts with a process known as pionisation. On average after ~86g/cm^2 of atmosphere has been traversed a 100GeV proton will interact with an atmospheric nucleus to produce a shower of protons, neutrons or larger fragments of the nucleus as well as some charged and neutral pions. The interaction length was noticed to reduce with increasing particle

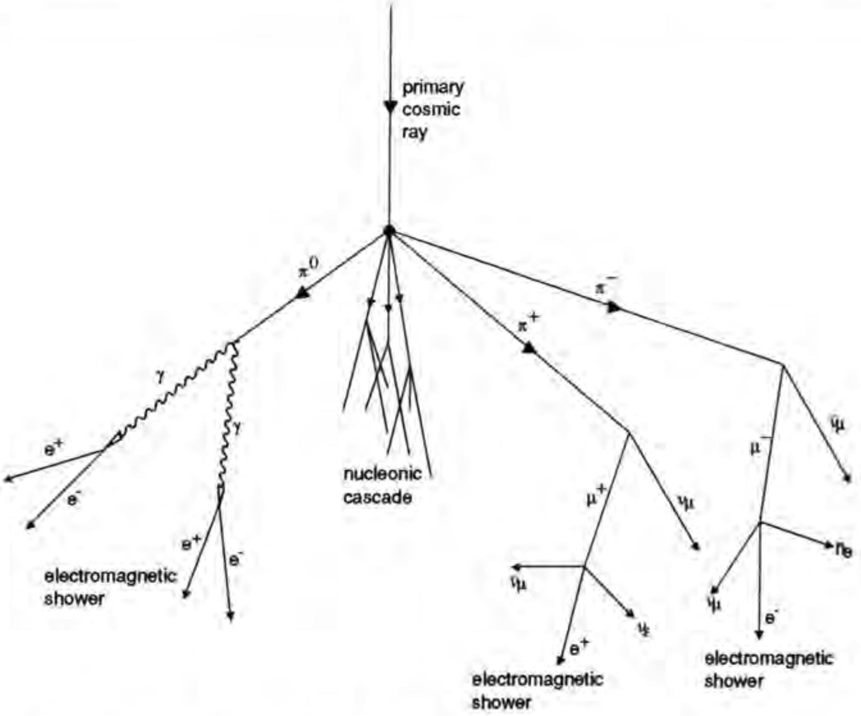

Figure 3.4: A schematic of a hadron EAS in the atmosphere.

energy in cosmic ray experiments in the late 1970s [59], [165]. The interaction lengths for proton-proton collisions in air have been measured as 83g/cm^2 and 60g/cm^2 for 1TeV and 1PeV protons respectively [70]. Pionisation will continue until the energy per particle drops below ~1GeV which is the energy required for multiple pion production. The neutral π^o are very short lived with a mean life time of 8×10^{-17}s and decay into two gamma rays. These will start electromagnetic showers which continue to develop in the atmosphere identically to a gamma ray shower by the processes of pair production and bremsstrahlung. The charged pions have a lifetime of 2.6×10^{-8}s and decay to very penetrating muons

$$\pi^+ \longrightarrow \mu^+ + \nu_\mu. \tag{3.8}$$

Muons produced in this reaction are ~100 times longer lived than the charged pions with a lifetime of 2.2×10^{-6}s. They are often produced with many GeV of kinetic energy and thus lose only a small fraction of this by ionisation of the atmosphere, ~2-3MeV/g/cm^2 . Energy can also be lost by bremsstrahlung, pair production and photo-nuclear interactions although the total fractional energy loss is small, ~10^{-4}/g/cm^2 for a 10GeV muon [2]. Above ~3 GeV the average relativistic lifetime of a muon is such that they are capable of surviving to ground level from an atmospheric altitude of ~20km. Lower energy muons may decay to electrons

$$\mu^+ \longrightarrow +e^+ + \overline{\nu}_e + \nu_\mu. \tag{3.9}$$

Since the mean free paths for proton and pion interactions in the air is 2-3 times that for a gamma ray, a proton will penetrate much deeper in the atmosphere before initiating an EAS than a gamma ray primary of the same energy. Large transverse momenta can be given to the pions produced in the pionisation process and they may separate from the primary particle axis by several tens of degrees. The development of hadronic EAS varies greatly from shower to shower and their lateral spread is much larger than pure electromagnetic showers. Gamma rays created in the π^o decays produce electromagnetic sub-showers, which can be distinctly separated from the main part of the shower. Muons, from charged pion decays, will be spread out from the shower core. The numbers of electrons in hadron EAS may rise or fall with altitude as nuclear fragments from the initial interaction penetrate further into the atmosphere before starting new electromagnetic showers. Figure 3.5 shows a simulation of the tracks of charged muons,

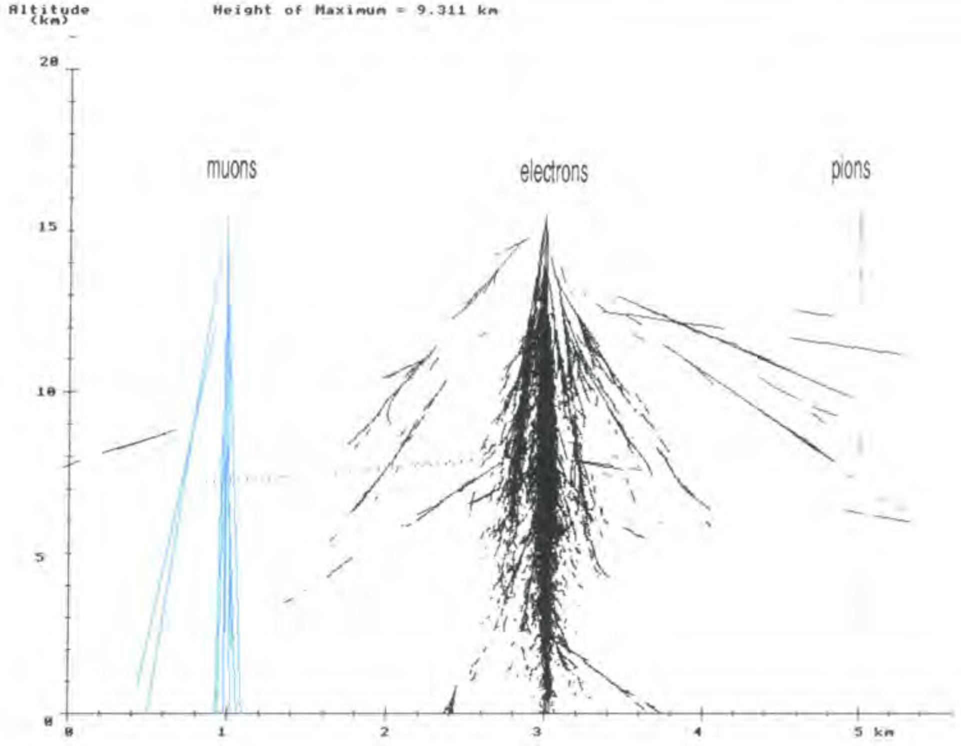

Figure 3.5: The longitudinal development of a hadron EAS showing electrons, charged muons and charged pions with energies > 21MeV, 4.3GeV and 5.6GeV respectively. The muon, electron and pion components of the shower have been separated for ease of viewing.

electrons and pions within a cascade caused by a 1TeV proton.

Cosmic ray nuclei tend to interact higher in the atmosphere with increasing atomic mass number. For an Iron nucleus the interaction length is much lower than for a proton, $\sim 2\text{g/cm}^2$. The nucleus will fragment quickly in the atmosphere and individual protons and neutrons will then go on to develop like proton EAS. Nuclear EAS also produce more muons, the number of which goes as the mass number, $A^{0.24}$ [88].

3.2.3 Differences Between Gamma Ray and Hadron Initiated EAS

Hadronic EAS can be thought of as a superposition of several electromagnetic showers each caused by the decay of neutral π^o and $\mu^{\pm}$ particles. The pions produced in nuclear interactions can have larger transverse momenta than the particles produced by the electromagnetic force. Hence the electromagnetic cascades in a hadron initiated EAS may diverge from the original particle axis by many degrees more than the single cascade formed by a cosmic gamma ray. Primary protons penetrate deeper in the atmosphere than gamma rays (with the same inclination to the atmosphere) before interacting and the particle production rate fluctuates greatly from shower to shower as proton collision products start new electromagnetic showers. Figure 3.6 shows the distributions of depth of maxima for a number of simulated showers, which are summarised in table 3.1. The heights of maxima for hadrons vary greatly from shower to shower and appear lower in the atmosphere than gamma rays of the same energy.

Particles from a proton EAS can appear a long way from the core of the shower, which is wide when compared to a gamma ray shower (figure 3.7).

Although the bulk of particles comprising a hadron EAS are electrons, positrons and gamma rays, the nuclear interactions which gave birth to the electromagnetic sub showers early in the EAS's development make it much wider and more penetrating, than a gamma ray EAS, with a highly fluctuating particle production rate.

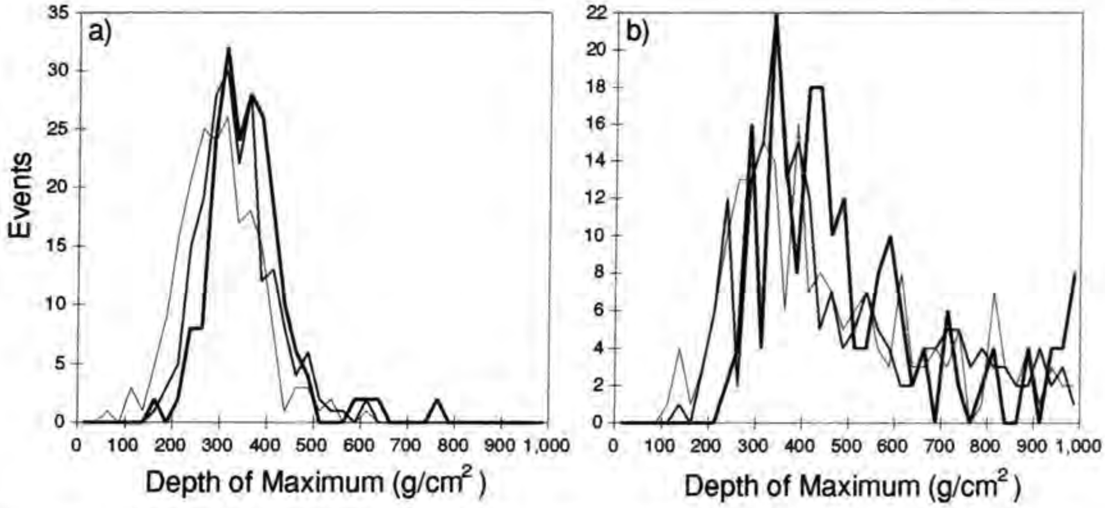

Figure 3.6: Normalised (to total events= 200) distributions of the depth of maxima for a) gamma ray and b) hadron showers. The thicker lines indicate higher primary energies (see table 3.1 for more details).

Table 3.1: The mean depth of the height of shower maximum distributions and their associated standard deviations for the simulated EAS shown in figure 3.6.

Primary Particle	Energy (GeV)	Number of Simulated Events	<Xmax> (g/cm^2)	σ (g/cm^2)
gamma ray	300	200	299	84
	500	200	334	78
	1000	100	359	86
Proton	500	200	461	213
	1000	200	470	206
	3000	100	502	197

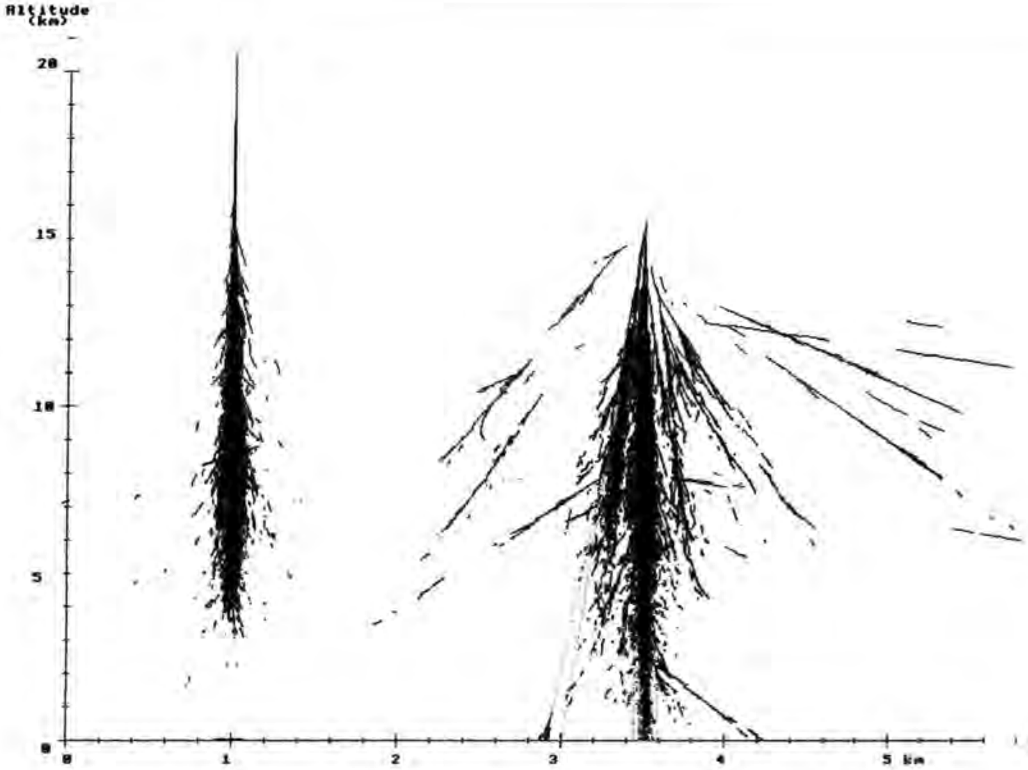

Figure 3.7: Simulations of EAS from a 300GeV gamma ray and a 1TeV proton falling vertically through the atmosphere. Note that although the proton has 3 times the primary energy of the gamma ray and particles within its shower penetrate to ground level, both showers heights of maximum ~9.5km.

3.3 Cherenkov Radiation

Scientists working in the field of radioactivity at the turn of the century, were aware that transparent substances in the vicinity of a strong radioactive source could emit a faint blue glow. The phenomenon was not properly investigated until the experiments of Mallet in the 1920s (reported in [111], [112], [113]), although he did not attempt to offer an explanation for the light's origin. It was not until

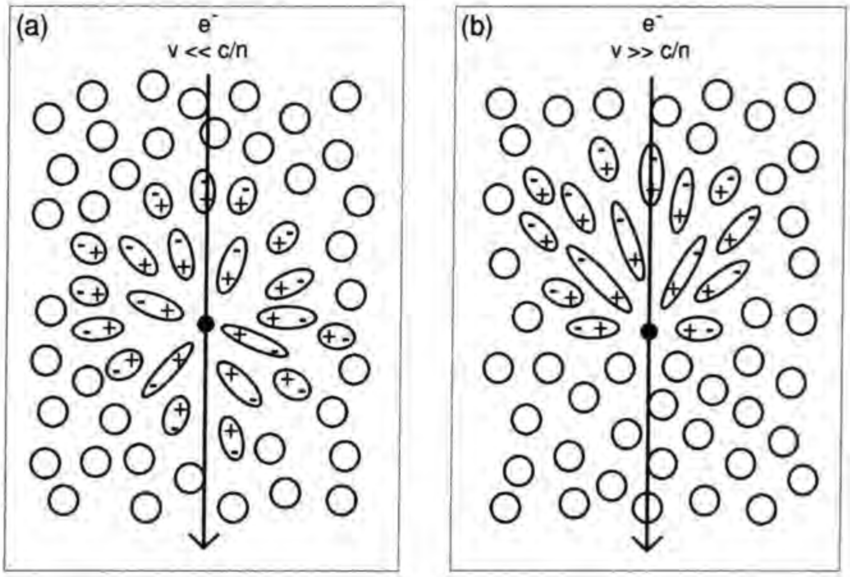

Figure 3.8: The polarisation of a medium when an electron moves through it with velocity a) $v < c/n$ and b) $v > c/n$ (from Jelley 1958).

the 1930s and the works of Čerenkov [32] that the effect was properly measured and named after him. A quantum-mechanical explanation was suggested soon after by Frank and Tamm [68] in 1937. A good descriptive account of Cherenkov photon production has been given by Jelley [93].

When a charged particle moves with a velocity v through a dielectric with refractive index n the surrounding atoms in the dielectric will be polarized by the electromagnetic field of the particle. The electrons around the nuclei are attracted to or repelled from the moving particle, depending on its charge, forming dipoles that point away from the particle. Every elemental part of the medium will receive a brief electromagnetic pulse as the particle passes through. The atoms return to their normal shape after the particle has passed. If the charged particle moves slowly through the medium (i.e. $v < c/n$) then the polarization field is completely symmetric and any net change in electromagnetic field will cancel out

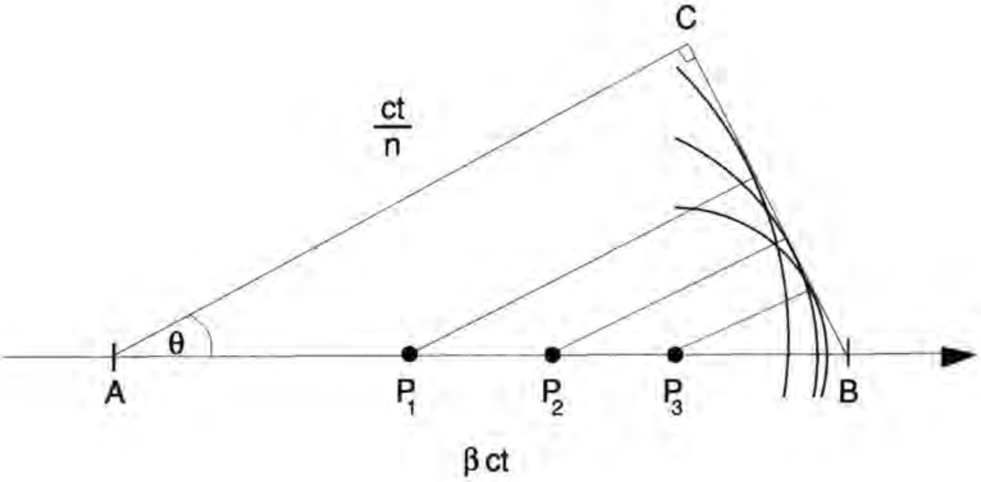

Figure 3.9: A charged particle moving along AB with velocity $v > c/n$ through a medium of refractive index n emits Cherenkov radiation at points P. The individual wavefronts at each point lead to a net emission of Cherenkov light over the surface of a cone with semi-vertical angle θ.

(figure 3.8a). However, for a particle moving with $v > c/n$ atoms ahead of the particle can not be distorted until the particle has passed them. Dipoles are only created behind the particle's present position and the symmetry is broken along the axis of motion (figure 3.8b). This results in a net electromagnetic pulse being emitted forward of the particle for every elemental length of the particles velocity. An analogy for this effect is the 'sonic boom' heard when an aircraft travels faster than the speed of sound in air.

For a fast moving particle a Huygens construction of the wavefronts of radiation produced in the medium shows how the Cherenkov photons are emitted at a particular angle θ with respect to the particle axis (figure 3.9). A charged particle is moving with a velocity $v = \beta c$ and travels from A to B in a short time

t emitting light at points along the way. In the same time the light emitted at A can travel a distance AC at a velocity c/n. The individual wavelets emitted along the particle's track combine to form a plane wave, from which the emission angle, θ, can be found

$$\cos\theta = \frac{AC}{AB} = \frac{1}{\beta n}. \tag{3.10}$$

Although the radiation is due to the asymmetry of polarisation of the atoms in the medium along the particle's axis, there is still azimuthal symmetry. This leads to the radiation from each elemental length of particle track being emitted over the surface of a cone with semi-vertical angle θ with its apex at the start of the track. Cherenkov radiation will only be produced when the particle velocity is above a minimum threshold given by

$$\beta_{min} = 1/n. \tag{3.11}$$

When $v = \beta_{min}c$ the angle $\theta = 0$. The maximum angle of emission, θ_{max}, will occur when $\beta = 1$.

$$\theta_{max} = \arccos\left(\frac{1}{n}\right). \tag{3.12}$$

Most media are dispersive so θ will be a function of the wavelength, λ, of the emitted photons. If $n(\lambda) < 1$ then equation 3.10 has no solution and Cherenkov radiation is not produced. In addition there will be absorption regions at some wavelengths due to anomalous dispersion. This effectively limits the production of Cherenkov photons in air to the near ultra-violet and visible regions of the spectrum.

3.4 Cherenkov Radiation in the Atmosphere

Any charged particle will produce Cherenkov photons in any medium with refractive index, $n > 1$, provided that it is energetic enough. For air, at visible wavelengths, $n = 1.000293$ at standard temperature and pressure (STP). The pressure of air in the atmosphere decreases approximately exponentially with altitude and is proportional to n. Writing $n = 1 + \eta$ allows us to formulate an expression for η as a function of altitude, h (from [93])

$$\eta(h) = \eta \exp(-h/h_o) \tag{3.13}$$

where h_o is the scale height for an exponential atmosphere, 7.1km. The kinetic energy of a particle, E, is given by $(\gamma - 1)mc^2$ where the Lorentz factor, γ is given by $1/\sqrt{(1-\beta^2)}$. Using equation 3.11, and since η is small, a threshold energy, E_T, can be defined below which no Cherenkov emission occurs

$$E_T = mc^2 \left(\frac{1}{\sqrt{(2\eta)}} - 1 \right). \tag{3.14}$$

The energy thresholds for charged particles to emit Cherenkov photons in air at normal temperature and pressure are as follows; electrons 21 MeV, muons 4.3 GeV, pions 5.6 GeV, protons 38 GeV and He nuclei 151.5 GeV. Most of the Cherenkov light in an EAS therefore, comes from electrons and positrons which are more numerous and have a considerably lower threshold energy for photon production than any other particle. The Cherenkov light will be emitted over a very small angle. Because $n \approx 1$ and using equation 3.12 we see that at sea-level $\theta_{max} \approx \sqrt{(2\eta)} \approx 1.3^\circ$.

The number of optical photons, N, within wavelength bounds λ_1 and λ_2 emitted by a relativistic electron per unit path length (in g/cm^2)is given by

$$\frac{dN}{dl} = \frac{20\pi\alpha}{\rho} l \left(\frac{1}{\lambda_2} - \frac{1}{\lambda_1} \right) \cdot \sin^2 \theta, \tag{3.15}$$

where $\alpha \approx 1/137$ is the fine structure constant, $\rho = 1.3$ is the atmospheric density in kgm^{-3} at sea level. This gives a value of ~250 Cherenkov photons, with wavelengths between 300 and 500nm, emitted per g/cm^2 of atmosphere traversed. Although large numbers of photons are emitted, this figure represents a very small fractional energy loss of the electron, $dE/dx \approx$ 100eV/g/cm^2 , several hundred times less than that for ionisation. If a 100GeV EAS produces 700 100MeV cascade electrons that each continue for 37g/cm^2 into the atmosphere then ~6×10^6 Cherenkov photons will be produced. The light will spread out in a pool, the size of which is determined by the altitude and value of θ of the emitting particle. For a vertically falling shower where $\theta = 1°$ at 10km altitude the light will fill a circular area with radius measured from the core, r ~150m. Therefore Cherenkov radiation from EAS is highly beamed and the optical photons are produced in large numbers. Since the electrons in the shower move with velocity nc in air the Cherenkov photons arrive at the ground in a short pulse. The pulse length can be approximated by

$$\Delta t = \frac{d}{c} \left(\frac{n-1}{n} \right) \tag{3.16}$$

where d is the length over which the photons are emitted, a few km, giving a pulse of photons lasting a few ns. A flux collector placed anywhere within ~150m from the core of a shower should be able to detect a brief but intense flash of optical photons at ground level.

3.5 Cherenkov Radiation from Gamma Ray EAS

Cherenkov radiation in gamma ray EAS is emitted by electrons with kinetic energies above 21MeV. The interaction length of 37gcm^{-2} for gamma ray photons means that the showers start high up in the atmosphere and die out fairly quickly. All the shower particles are created with little transverse momentum and consequently the EAS forms a narrow column in the atmosphere, glowing with Cherenkov light. Each radiating particle emits a cone of photons with an opening angle given by equation 3.10. This angle is ~1° for particles high in the atmosphere and rises to ~1.5° at sea level as the refractive index of the atmosphere increases with depth. The increase in the Cherenkov angle at lower altitudes leads to a focussing effect at ~100m from the shower axis and the ground level Cherenkov photon lateral density function (LDF) rises slowly to a prominent circular ridge, often known as the 'hump', before dropping away quickly (figure 3.10). Nearer to the shower axis the photons are radiated by particles in the tail of the shower, nearest to the observer. The Cherenkov photon intensity here will fluctuate greatly from shower to shower. Electrons that penetrate to ground level from showers with the highest primary energies may also be surrounded by localised bright peaks of light [85]. The Cherenkov photon LDF of these showers may show a steeply increasing brightness profile towards the core of the shower. Beyond the hump the brightness falls off rapidly as $1/r^2$ and the photons are due to Cherenkov

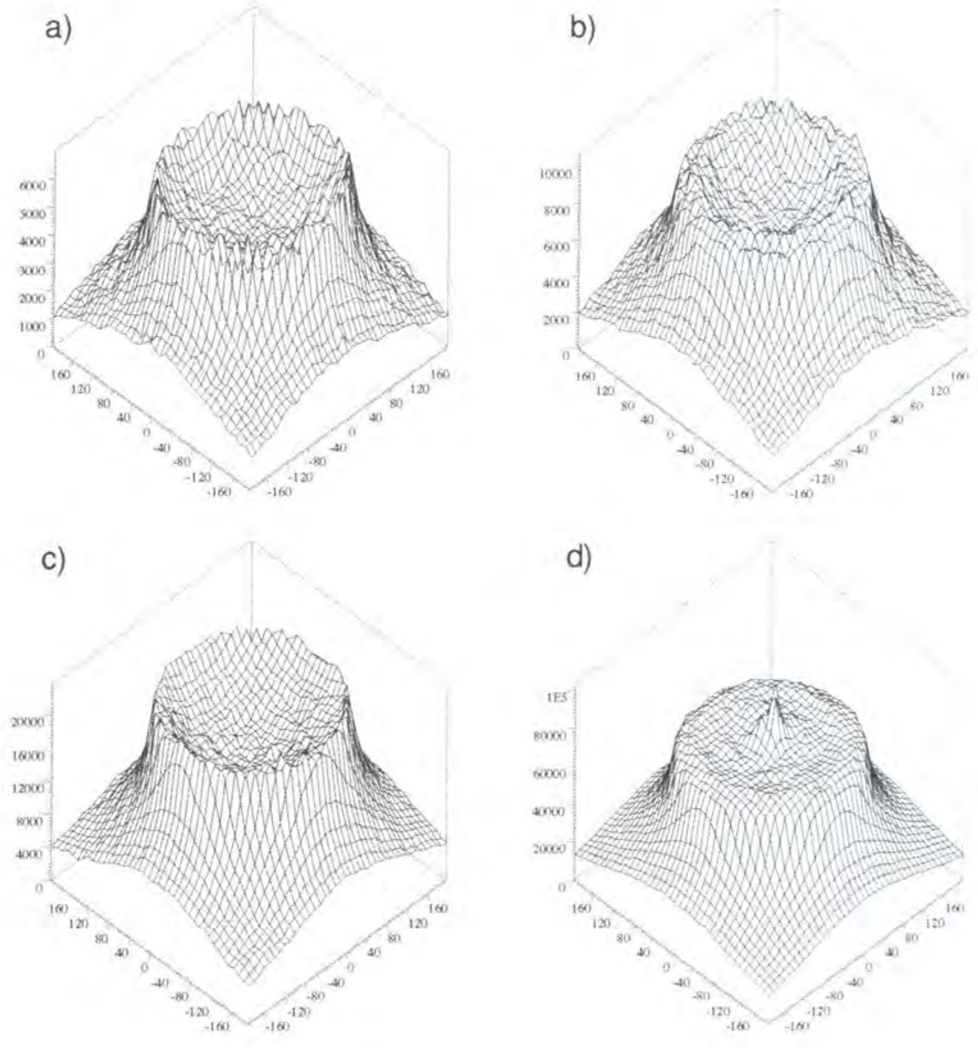

Figure 3.10: The distribution on the ground of Cherenkov photons from gamma ray EAS with primary energies of a) 300GeV, b) 500GeV, c) 1TeV and d) 3TeV. The distributions are measured over a 400×400m area with 10×10m grid resolution.

emission from lower energy electrons which have been deflected away from the shower axis by many large angle Coulomb scatterings.

3.5.1 Cherenkov Radiation from Nucleonic EAS

The average interaction length for hadrons is 83gcm^{-2} at 1TeV and so hadron EAS begin deeper in the atmosphere and may penetrate to ground level. This leads to a lateral distribution of photons which is peaked around the shower axis and drops away with distance from the shower axis (figures 3.11 and 3.12). Electromagnetic showers produced by pion decay within the shower also produce peaks of brightness away from the core. Since high energy hadron showers penetrate deep into the atmosphere there are likely to be bright peaks of Cherenkov light from low altitude electrons. The distinctive hump in the LDF from gamma ray EAS is not usually visible in hadron initiated showers. Hadron EAS can be thought of as a collection of many electromagnetic showers all pointing at different angles and hence the net focussing effect, seen in gamma ray EAS, is lost [135]. Up to a few tens of muons are also created in hadronic showers and easily penetrate to ground level. Figure 3.13 shows a 300GeV proton event in which the Cherenkov emission is dominated by two penetrating charged muons. A ring of light from each particle is clearly visible and surrounds a bright peak emitted by the particle nearer to the ground. The light in the peak will arrive at the ground first since the muons are travelling much quicker through the atmosphere than any other particle in the shower.

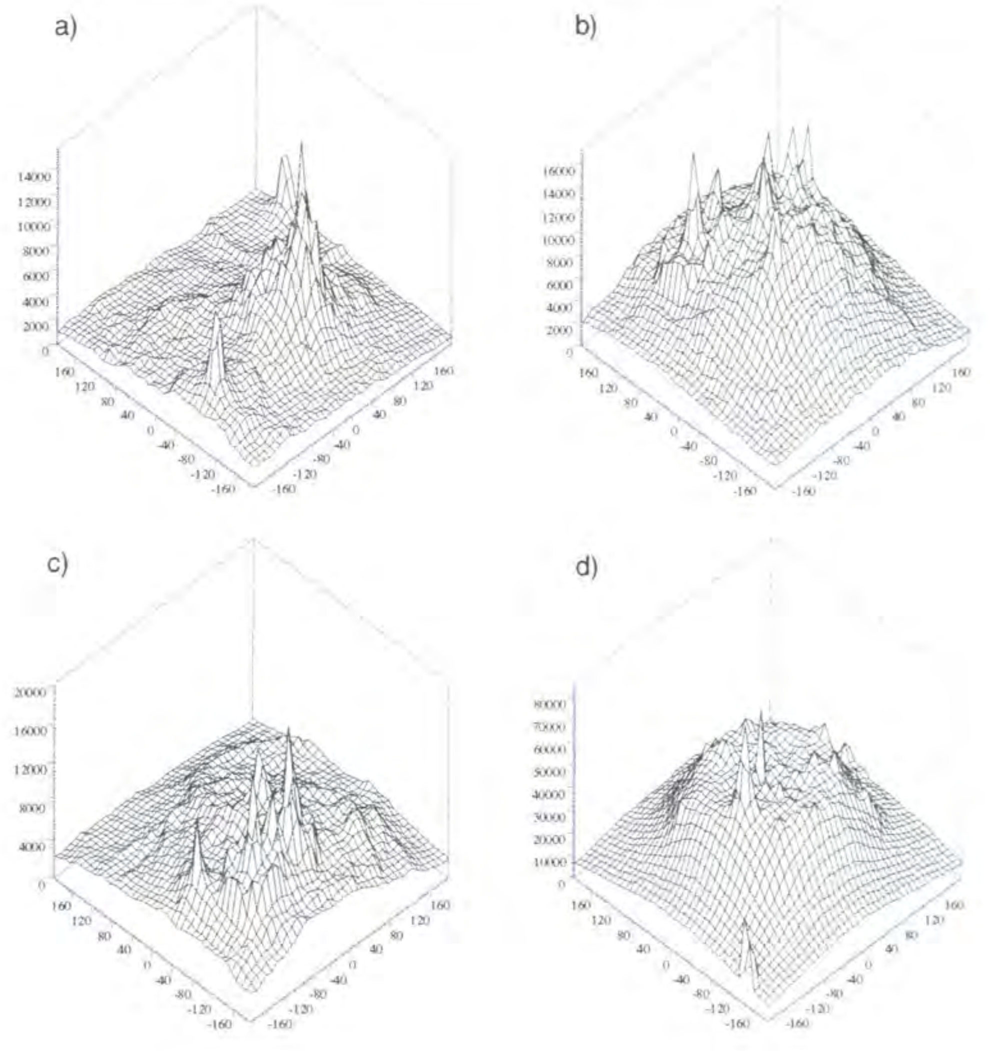

Figure 3.11: The distribution on the ground of Cherenkov photons from proton EAS with primary energies of a) 500GeV, b) 1TeV, c) 1.5TeV and d) 3TeV. The distributions are measured over a 400×400m area with 10×10m grid resolution. Note the peaks of light due to individual particles penetrating to near ground level.

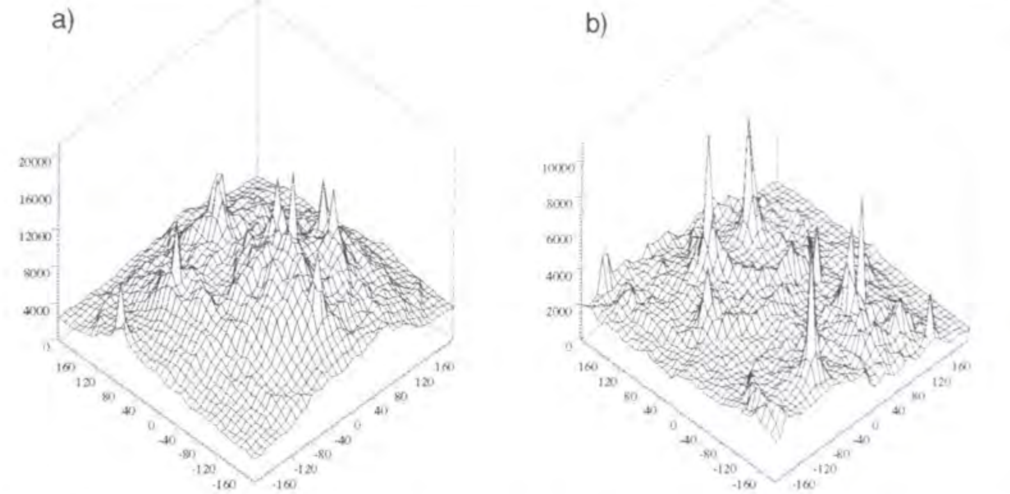

Figure 3.12: The distribution on the ground of Cherenkov photons from a) Helium and b) Magnesium nuclei with primary energies of 2TeV. The graphs are measured over a 400×400m area with 10×10m grid resolution.

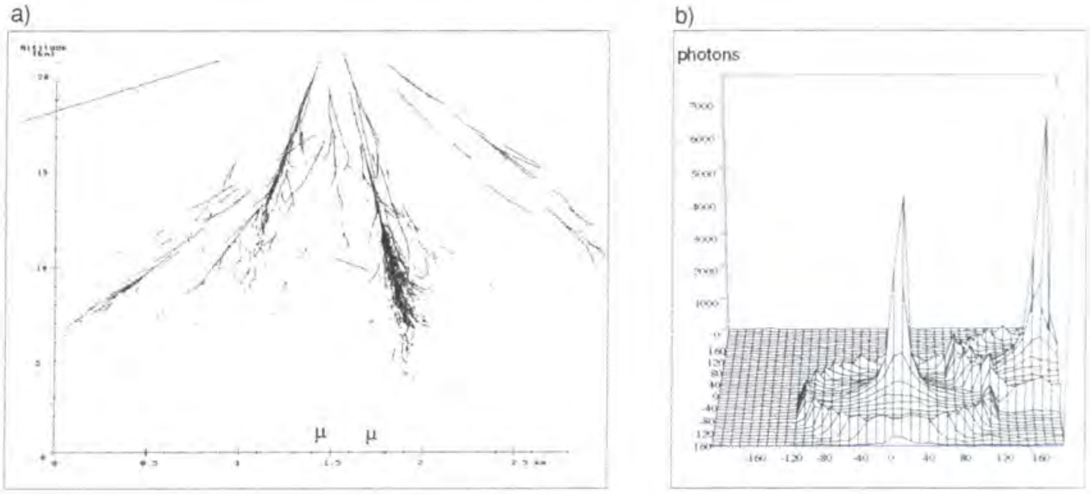

Figure 3.13: a) A low energy (300GeV) proton EAS with two penetrating high energy muons. b) The Cherenkov emission, plotted on the ground in 10×10m bins, is dominated by the muons.

3.6 The Differences Between gamma ray and Hadron Cherenkov Events

3.6.1 Cherenkov Photon Yield

Turver and Weekes [153] investigated the emission of Cherenkov photons and found that gamma ray and proton EAS at different energies yielded different amounts of light. Below 1TeV the ratio of Cherenkov photon emission from gamma ray and hadron EAS rose from a factor of 2-3 to ~14 at a core distance of 100m. Simulations of EAS have been performed to find the Cherenkov photons detected, over a 400×400m area centred on the core, from gamma rays and hadrons, and their ratios. The results are shown in figure 3.14(a-b). It can be seen that the yield of Cherenkov photons from gamma ray EAS increases quicker than the number of photons seen from hadron EAS with decreasing energy. There is some evidence for a steep rise in the ratio at lower energies. On a shower to shower basis there is a greater variation in Cherenkov photon density from proton EAS than there is in EAS initiated by gamma rays.

The reason for the reduction in emission from proton showers is that pions and muons created in the cascade take an increasingly large fraction of the energy budget as primary energy decreases. The energy threshold for Cherenkov emission from muons is $>$ 4GeV, considerably higher than for electrons, due to their considerably larger rest mass, and these particles may contribute nothing to the total Cherenkov emission in the lowest energy showers. Hence there is an increasingly diminishing amount of primary energy available to produce electrons. The electrons that are produced will have lower energy and thus be more susceptible

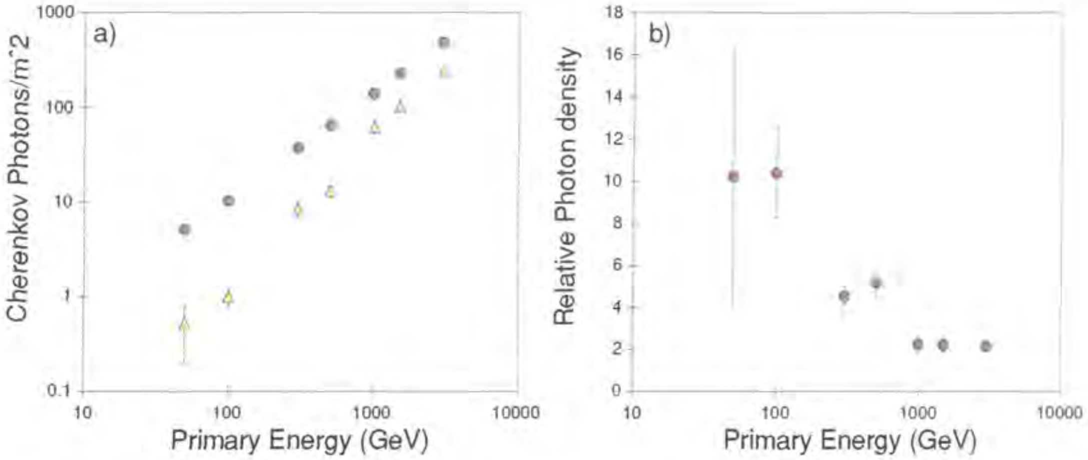

Figure 3.14: Monte Carlo simulations of Cherenkov photon yields from gamma ray and hadron EAS. a) The Cherenkov photon densities measured from gamma ray (circles) and proton (triangles) primaries as a function of energy. b) The ratio of gamma ray/proton Cherenkov photon density. Statistical error estimations are shown.

to large angle Coulomb scattering. The Cherenkov photon emission decreases and is more spatially diffuse as primary proton energy reduces. The effect of this is that at lower primary energies it becomes relatively easier to detect gamma ray initiated than hadron initiated Cherenkov events. The drive to reduce the energy thresholds of Cherenkov telescopes has increased over previous years not only to close the gap in the observable electromagnetic spectrum but also to exploit this effect.

A very simple calculation of the minimum gamma ray energy detectable by a Cherenkov telescope can be made using the model of section 3.2.1. A detector is assumed, with a large $100\mathrm{m}^2$ flux collector and photon detectors capable of detecting a pulse of 100 photons, and placed in a light pool of $10^5\mathrm{m}^2$. The total emission of Cherenkov photons for the shower to be detected would have to be ~100photons $\times 10^5 \text{m}^2/100\text{m}^2 = 10^5$ photons. From equation 3.15 we see that a high energy electron emits ~9000 photons per cascade length. Therefore the number of electrons required to produce a detectable Cherenkov pulse would be ~12. The number of particles in the shower doubles after each cascade length with electrons produced by pair production being twice as numerous as bremsstrahlung gamma rays in the toy model considered. The number of cascade lengths, n, required to produce the necessary 12 electrons is given by $2^n = 12 \times 3/2 \longrightarrow n \approx$ 3-4. After four cascade lengths each particle in the shower has energy $= E_o/2^4$. Since electromagnetic showers effectively stop in the atmosphere when ionisation of the atmosphere by the electrons becomes important at ~80MeV then the minimum primary gamma ray energy detectable would of the order of 1-2GeV.

In practice this low threshold is unrealistic due to inhomogeneities in the LDF and because the calculation takes no account of the effective sensitive area of the detector. The lowest energy threshold detectors currently in operation are the 'solar farm' type, with threshold energies ~50GeV (discussed briefly in section 4.4). At these low energies the Weekes and Turver effect may not be fully exploited in improving the gamma ray signal/background ratio due to the electron component of the cosmic ray spectrum, which may be ~1% of the proton background at a few GeV [120]. Electron initiated showers are identical to gamma ray EAS apart from the first interaction which is bremsstrahlung. It would be very difficult to identify electron showers if they amounted to a significant fraction of the gamma ray signal.

3.6.2 Fluctuations in Cherenkov Photon Density over Small Distances

It was shown in the previous sections that the Cherenkov LDF from hadronic EAS vary greatly from shower to shower and are individually subject to large fluctuations in photon density. Individual gamma rays on the other hand appear very similar to each other and lack the muon component. Simulation studies have shown that the numbers of Cherenkov photons from gamma ray EAS seen by more than one detector, separated by small distances, should be well correlated. The work of Sinha [144] considers three sections of the LDF, the 'plateau' (comprising the light within 100m of the particle axis), the 'hump' (light from 100m to 145m) and the 'steep' region (further than 145m) and finds significant correlation between the photons collected by two 1m^2 mirrors separated by 10m in all three regions. The correlation is greatest in the plateau region and is still highly significant if the separation between the mirrors is increased to 50m. Furthermore the degree of correlation increases in the plateau and steep regions as primary energy increases. This is not true in the hump region and may be because the significance of the hump decreases with increasing primary energy as the shower penetrates deeper into the atmosphere.

Hadron events are considerably less well correlated. Figure 3.15 shows some statistical measures of the fluctuations in Cherenkov photon brightness seen in simulations of gamma ray and hadron EAS at various core distances [13].

Simulations of Cherenkov emission from EAS have been used here to investigate other measures of Cherenkov photon density fluctuation over small separations. The percentage fluctuation in simulated photon density between two

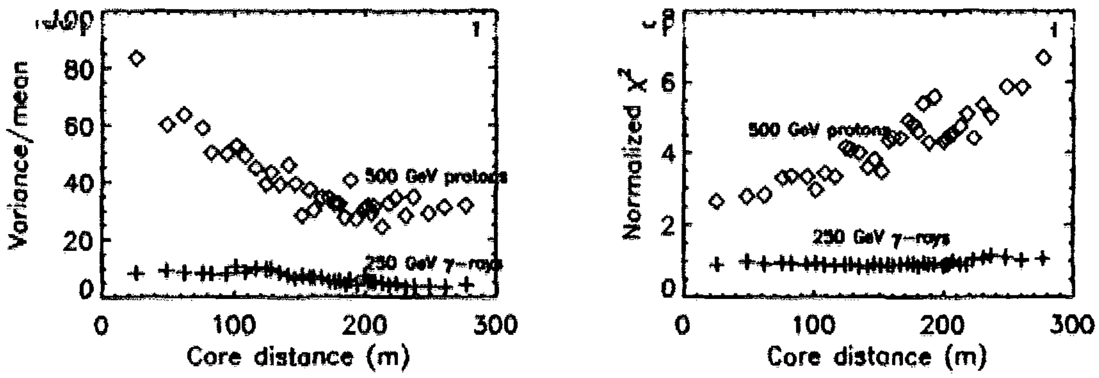

Figure 3.15: Statistical measures of the fluctuations in Cherenkov photon brightness of gamma ray and proton EAS (from Bhat 97).

separated 10 × 10 m bins, A and B, has been described by the parameter Δ where

$$\Delta = \left| \frac{A - B}{B} \right| \times 100\% \tag{3.17}$$

and A and B are both in the plateau region of the LDF, within 100m of the core. The mean value of Δ from several measurements is plotted in figure 3.16 as a function of energy for mirrors separated by various distances.

For gamma rays Δ is small and varies little from shower to shower. At 50GeV Δ ranges from 10% for 10m separation to 14% for 50m separation and decreases with increasing primary energy. The decrease in Δ is smaller for larger separations; for 10m separation the ratio of the values of Δ at 50GeV and 3TeV is ~5. With 20m and 50m separations the ratio is ~3 and ~2 respectively. For protons Δ is ~10 times higher than it is for gamma rays at 50GeV. The spread of Δ measured at different points within a shower is characterised by $\sigma(\Delta)$ (figure 3.17). It can be seen that there is much greater variation in measurements of

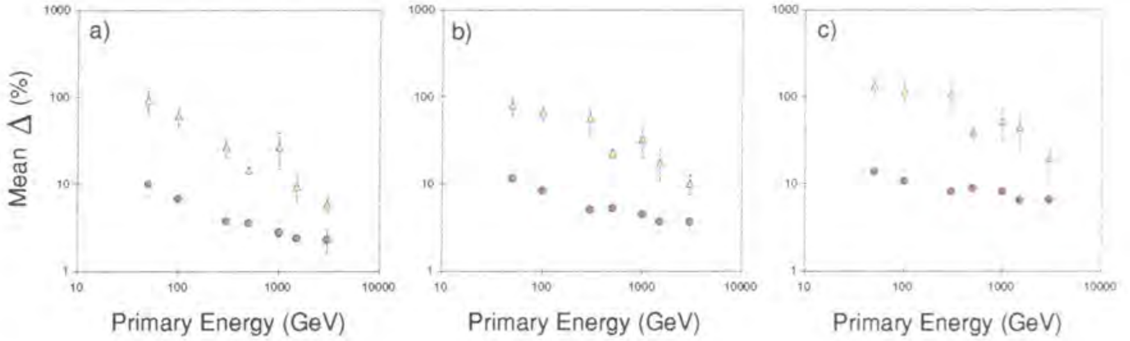

Figure 3.16: The mean values of Δ seen by two 100m^2 mirrors separated by a) 10m, b) 20m and c) 50m. gamma ray and hadron events are shown as circles and triangles respectively. Statistical error estimations are shown.

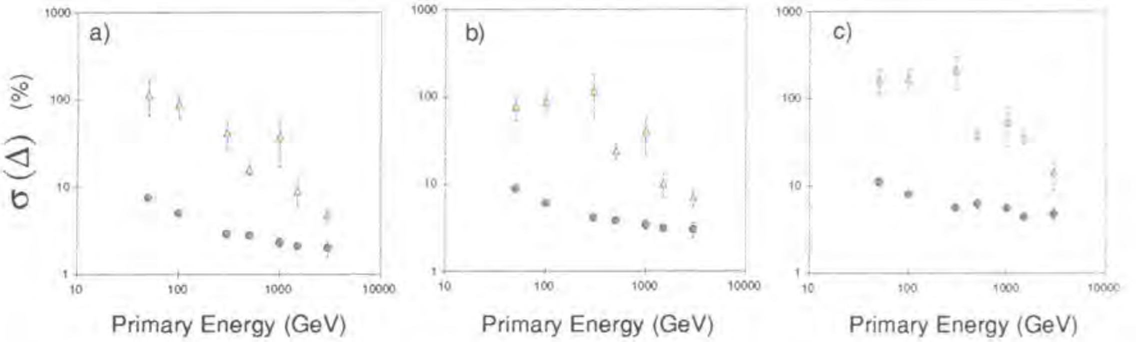

Figure 3.17: The mean variation in Δ measured at different points within the Cherenkov LDF seen by two 100m^2 mirrors separated by a) 10m, b) 20m and c) 50m. gamma ray and hadron events are shown as circles and triangles respectively. Statistical error estimations are shown.

fluctuation in proton showers than there is for gamma ray showers.

3.7 Summary

The differences in gamma and hadron initiated Cherenkov events are due to the physics of the processes at work in cascades of particles in the atmosphere. A useful model of the differences between the types of shower is given by [86] from which figure 3.18 is taken. On average half of the light from a gamma ray EAS is emitted within ~20m of the core. The wider hadronic EAS emit half of their light within a region ~70m from the core and on average penetrate deeper into the atmosphere. The images of hadron showers viewed by an optical system will thus appear wider than those of gamma rays. The penetrating muon component and electromagnetic subshowers formed by non axial pions in hadronic EAS make the Cherenkov images much patchier than gamma ray events and they lack the distinctive Cherenkov hump. At low (tens of GeV) primary particle energies the Cherenkov photons produced by gamma ray showers heavily outnumber those from protons. This is due to the large fraction of primary proton energy that goes into creating muons that are below the Cherenkov photon emission threshold. Monte-Carlo simulations of air showers have suggested that separated detectors viewing the same Cherenkov event will measure larger and more varying amounts of fluctuation in Cherenkov photon brightness from hadron EAS than gamma ray EAS. These differences may be used to distinguish gamma ray induced Cherenkov events from the isotropic and numerous hadron background.

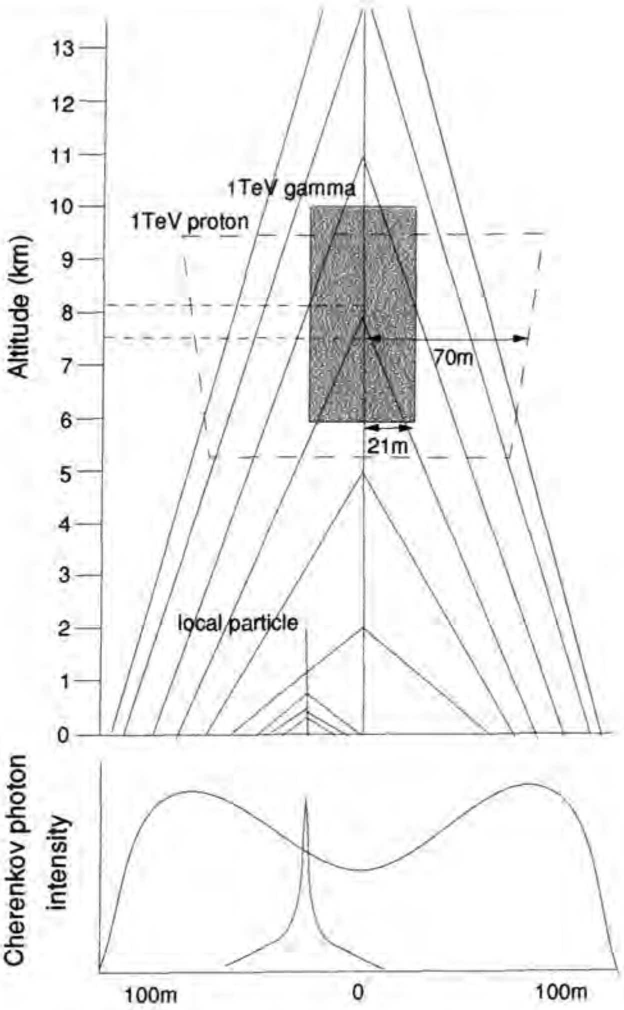

Figure 3.18: A simple model of air showers where Cherenkov photons are emitted along the tracks shown from vertically falling electrons leading to the humped intensity profile shown. The grey and dashed boxes show the 'median' emission cylinders where half of the total Cherenkov photons originate from 1TeV gamma rays and protons respectively. The boxes are centred so that a quarter of the photons are emitted above and a quarter below them. Particles at ground level lead to localised peaks of light (from Hillas 96).

Chapter 4

GROUND BASED VHE GAMMA RAY ASTRONOMY

4.1 Introduction

This chapter describes the detection of Cherenkov photons from the night sky by various experimental techniques. A summary of Cherenkov telescopes in use around the world is given.

4.2 Detection of Cherenkov Radiation from Extensive Air Showers

The first detection of light pulses from high energy air showers was in 1953 due to the work of Galbraith and Jelley [71]. Cherenkov photons from EAS make up only $\sim 10^{-4}$ of the total night sky starlight background [17]. Although this is a small fraction of the total photon flux, large numbers of Cherenkov photons from a single shower arrive at ground level in a very short pulse ~few ns in duration.

The Cherenkov signal, S_C, detected by a PMT at the focus of a mirror is related simply to the characteristics of the detector

$$S_C \propto \eta A_m \,, \tag{4.1}$$

where A_m is the area of a mirror $(\pi D^2/4)$ of diameter D and η is the product of the quantum efficiency of the PMT and the reflectivity of the mirror $(0 < \eta \leq 1)$. If the same detector system is exposed to the night sky for a time t there will be a mean signal, S_{NS}, due to the night sky starlight background,

$$S_{NS} \propto \Omega A_m \eta t \Phi, \tag{4.2}$$

where Ω is the solid angle subtended on the sky by the detector and Φ the photon flux from the night sky background ($\sim 2\times10^{12}$photons/s/sr/m^2 [121]). The fluctuation on this signal is dominated by poissonian statistics such that we can create an expression for the noise, σ_{NS},

$$\sigma_{NS} \propto \sqrt{S_{NS}} \propto \sqrt{\Omega A_m \eta t \Phi}. \tag{4.3}$$

If t is comparable to the length of time that the shower takes to develop, i.e. a few ns, then σ_{NS} will be minimised. Thus if fast electronics in the detector allow short enough observations it could be possible to detect the light from individual showers over the background noise, the minimum signal threshold being given by the inverse of the signal to noise threshold

$$S_{min} \propto \sqrt{\left(\frac{\Omega t \Phi}{A_m \eta}\right)}. \tag{4.4}$$

Galbraith and Jelley's first experiment involved the use of a single photomultiplier tube (PMT) viewing a 25cm parabolic mirror. By placing the PMT apparatus at the centre of an array of 16 Geiger counters it was possible to show that the light pulses were due to high energy charged particles in the atmosphere and not other effects such as distant lightning or meteoric showers. Further experiments [72], [94] used two similar detectors placed side by side with overlapping fields of view. By adjusting the size of the field of view of the detectors and slowly moving their optic axes apart until the rate of coincident signals dropped to zero it was possible to show that the light in the two detectors was parallel to $\sim 1^\circ$. This provided evidence that the detected signals originated mostly from particles at the core of EAS travelling nearly parallel to the primary particle's path. Further experiments on the spectral distribution and polarisation of the photons detected led to the conclusion that the light seen was indeed Cherenkov radiation from EAS. Much of the early work in ground based Cherenkov astronomy was spent developing the hardware involved, such as electronics, PMTs etc. and it was not until the 1980s that Cherenkov telescopes dedicated to gamma ray astronomy started to emerge.

4.3 Atmospheric Cherenkov Telescope Design

The major advantage of a ground based gamma ray telescope is that its effective sensitive area (ESA), A_γ, for gamma ray showers is determined by the size of the Cherenkov light pool on the ground and is potentially very large. An estimate of the size of the ESA can be made for a Cherenkov detector with a given field of view, α° , and is illustrated in figure 4.1 for a shower observed at zenith angle,

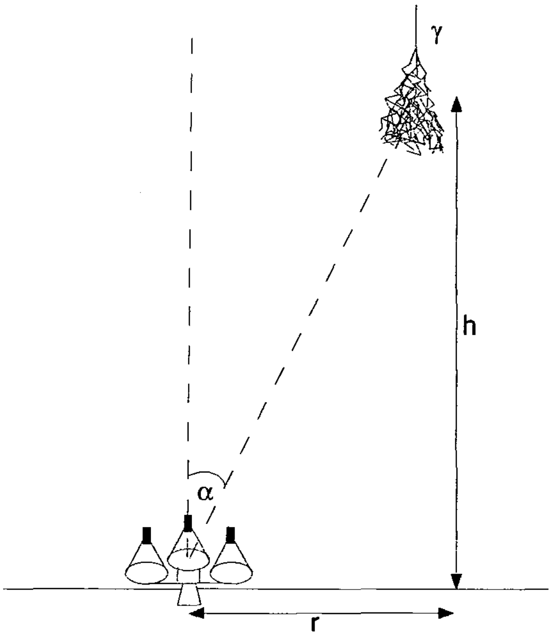

Figure 4.1: An estimate of the effective sensitive area (ESA) of a Cherenkov detector.

$\theta = 0$. The furthest gamma ray EAS, falling parallel to the detector optic axis, which can be detected will maximise just at the edge of the field of view. This will be at a distance away from the detector, d, equal to the vertical height h. A simple geometric approximation for a small field of view gives the radius, $r \approx (\pi\alpha d)/180$ of the light pool on the ground. The ESA is then simply the area of the circle with radius r. For showers observed at the zenith, a depth of maximum of ~300g/cm^2 gives h ~10km and ESA ~2×10^5m^2 .

At larger θ an EAS which maximises after traversing 300g/cm^2 of atmosphere will actually maximise at a vertical depth in the atmosphere equal to $300 \times \cos\theta$. In an exponential atmosphere this will be at a higher vertical altitude, h, than in the $\theta = 0°$ case. This gives a larger value for $d/\cos\theta$ and hence an increased ESA. At $\theta = 60°$ the same energy shower which maximised at 300g/cm^2 in the vertical case will actually maximise at a vertical depth of 150g/cm^2 . A suitable atmospheric model returns $h = 13.5$km for this grammage. The ESA is then ~five times larger than in the vertical case since $d = 13.5/\cos\theta = 27$km. Observing Cherenkov events at low elevations has been suggested as a way of measuring the energy spectra of astronomical objects at > 10s of TeV [148], [42]. At these energies experiments with large ESA are necessary as the flux of photons from such objects is small.

Unfortunately the ESA for gamma ray collection is similar to that for the hadronic cosmic ray background. The hadron flux can be larger than that from a gamma ray source by factors of several hundreds. Some method of distinguishing gamma ray Cherenkov events from the background needs to be applied if the experiment is to be a success.

A simple Cherenkov telescope will consist of three main components; a light collector and photon detectors placed on a steerable mounting system. A Cherenkov event happens in a very short time (~5ns) because atmospheric Cherenkov photons emanate from highly relativistic particles. This makes PMTs, with their fast rise times and high gains, the detectors of choice in Cherenkov telescopes. The choice of window glass and photo-cathode material can also be optimised for maximum sensitivity in the 300 - 500 nm range for Cherenkov light.

Several texts (e.g. [63], [158]) define a quantity, N_σ, which is the statistical significance, in number of standard deviations, obtained by viewing a source of gamma rays with spectral index α,

$$N_\sigma \propto \frac{A_\gamma \sqrt{T}\, E_T^{(0.8-\alpha)}}{\sqrt{A_h \Omega}}. \tag{4.5}$$

Hence the statistical significance may be enhanced by increasing the amount of observation time of the source, T, and reducing the energy threshold of the telescope, $E_T \propto S_{min}$. Minimising the solid angle of sky viewed by the telescope, Ω, can also increase N_σ although it must remain large enough to detect gamma rays. Recent detectors under development have fields of view with radii ~2° . The quantities A_γ and A_h are the effective collection areas for gamma ray and hadron showers. In a simple detector these areas are given by the size of the light pool at ground level and are equal for gamma rays and hadrons. However, the value of N_σ can be further increased by applying some form of analysis to the data which discriminates between gamma rays and hadrons. By removing hadrons from the data set and retaining gamma rays A_h can effectively be made smaller than A_γ. When the design of a Cherenkov telescope includes further methods of hadron rejection equation 4.5 includes a further term,

$$N_\sigma \propto Q\frac{A_\gamma\sqrt{T}\,E_T^{(0.8-\alpha)}}{\sqrt{A_h\Omega}}. \tag{4.6}$$

The quality factor Q,

$$Q = \frac{F_\gamma}{\sqrt{F_h}}, \tag{4.7}$$

is the increase in significance of a gamma ray signal when an analysis procedure retains fractions F_γ and F_h of the gamma ray and hadron data. Analysis techniques are discussed further in Chapter 6.

The sensitivity to Cherenkov photons of the telescope can be increased by running the photon detectors at a higher gain. However, this will cause a higher number of 'accidental' triggers due to the night sky starlight background rather than genuine Cherenkov events. A reduction in accidental triggers can be obtained by reducing the integration time, t, of the detectors, although in practice this may be difficult. Coincidence techniques can be used to allow the operation of the detector system at maximal gain whilst allowing an acceptable amount of accidental triggers. The technique requires signals from more than one paraxial optical/detector systems to pass a discriminator threshold within a narrow time interval, Δt, to trigger the telescope. The rate, R, at which a trigger condition requiring C detectors to pass a discriminator threshold is satisfied by chance is given by

$$R = C!\, n^{C}\, \Delta t^{(C-1)}, \tag{4.8}$$

where n is the count rate of each detector. Increasing C allows a reduction in E_T of the telescope by increasing its sensitivity to Cherenkov events whilst maintaining a constant rate of accidental triggers. The effect of Turver and Weekes discussed in section 3.6.1 may also lend a hand in increasing N_σ at lower primary particle energies.

As well as its effect on increasing N_σ a reduction in detectable threshold energy is scientifically very important to close the gap in the observed electromagnetic spectrum between ground and space based experiments.

4.4 Experimental Methods in Ground Based Gamma Ray Astronomy

The field of ground based gamma ray astronomy is a very active one with about a dozen research groups operating world wide. A summary of experiments currently in operation are shown in table 4.1. Only Cherenkov experiments which presented papers at the fifth 'Towards a Major Atmospheric Cherenkov Detector' Workshop at Berg-en-Dal, South Africa in 1997 have been included in the table (proceedings in [92]). Air shower arrays, which generally operate in the Extremely High Energy (EHE) range, at energies above ~100TeV, have not been included in the table. These experiments have been used for many years to observe the particles produced in EAS using a grid of plastic scintillators (usually ~$1m^2$ each). Reviews of the role of air shower arrays in ground based gamma ray astronomy are given elsewhere (e.g [121]).

There are currently two main techniques used in ground based gamma ray astronomy. The most popular of these is the 'Imaging Atmospheric Cherenkov Technique' (IACT) where Cherenkov photons are collected and focussed on to a pixellated detector. Background events are then rejected from the signal on the basis of the shape and orientation of the image in the camera. The 'Stereo' method uses at least two separated telescopes to view individual Cherenkov events. A trigonometric reconstruction of the EAS can be made, allowing an accurate determination of the primary particle origin and the height of air shower maximum. Elements of modern stereo arrays of Cherenkov Telescopes can also be used individually as IACT telescopes. This allows great flexibility of operating

Table 4.1: Various ground based Cherenkov experiments currently in operation, their geographical location and the experimental method used.

Experiment	Location	Lat.,Long. (°)	Altitude (km)	Method	Refs.
CANGAROO	Woomera, Australia	31.1S,136.8E	0.2	IACT	[149]
CAT	Targasonne, France	42.5N,2.0E	1.7	IACT	[77]
CELESTE	Targasonne, France	42.5N,2.0E	1.7	Solar	[133]
Durham Mk6	Narrabri, Australia	30.5S,150.0E	0.2	IACT	[37]
HEGRA	La Palma, Spain	28.8N,17.9W	2.2	Stereo	[51]
SHALON	Tien-Shan, Russia	42.0N,75.0E	3.3	IACT	[145]
STACEE	Albuquerque, USA	~35N,105W	~1	Solar	[122]
TACTIC	Mt. Abu, India	24.6N,72.7E	1.3	IACT	[14]
Whipple	Mt. Hopkins, USA	31.7N,110.9W	2.3	IACT	[161]

modes and forms the basis of many proposals for future experiments such as the VERITAS [162] and HESS [89] arrays.

A third group of telescopes are listed in table 4.1 as 'Solar'. In able to detect the lowest energy gamma rays an experiment must be able to detect the faintest of Cherenkov pulses. This requires a large detector area. 'Solar Farm' electricity generation plants consist of large numbers of steerable mirrors covering many hundreds of m^2 . Two prototype detectors, CELESTE [124], [133] and STACEE [122], have used these existing facilities to collect Cherenkov photons and focus them onto PMTs that each view an individual heliostat via secondary optics. Gamma/hadron discrimination is obtained on the basis of the shape of the measured LDF. The origin of the primary particle can be found by using the times of arrival of Cherenkov pulses at the PMT array to reconstruct the wavefront from the EAS. Presently the energy threshold for these experiments is estimated at ~50GeV.

4.4.1 Single Dished Telescopes and the Imaging Atmospheric Cherenkov Technique

The Imaging Atmospheric Cherenkov Technique (IACT) is operated by many research groups around the world and is considered by many to be the 'standard' method of observing VHE gamma ray sources. A single dished telescope, consisting of a large light collecting mirror (typically of order several metres in diameter) with a wide field pixellated PMT array at its focus, is used to observe Cherenkov radiation from EAS. The optical system is fixed on to a steerable mount to allow the tracking of a candidate source for long periods of time as it rotates through the sky during an observation. Observations are carried out during dark night periods, although some groups have used filters to allow limited operation under moonlight [8]. The detector package is triggered when some criterion, usually several adjoining PMTs passing a discriminator threshold, is satisfied and the signals from all the PMTs read out and stored. The threshold for gamma ray detection of a Cherenkov telescope depends on the minimum Cherenkov photon brightness which can be detected above background noise. This depends on a number of factors, such as the zenith angle, core location and the telescope's trigger and is complicated to calculate. The energy threshold for the Durham Mk6 telescope is discussed in section 5.1.6. Low energy events which trigger the telescope also need to be reliably separated from the hadron induced background which may outnumber the gamma ray events by 1000 to 1.

It was shown, in section 3.2.3, that hadron and gamma ray EAS develop differently in the atmosphere. The images of the two types of events have distinct appearances. Primary particles can be identified by fitting some mathematical model to the pixellated images and rejecting background hadron events that do not pass criteria based on the image's position in the detector field of view, shape and orientation. The 'gamma ray likeness' criteria can be based on detailed simulation studies of the telescope's response to different types of EAS or on the results of previous observations of a known, statistically significant, gamma ray source such as the Crab nebula. A very successful method of describing shower images over the last decade has been through the calculation of the 'Hillas parameters'. The Hillas parameters are the properties of an ellipse, produced by analysis of the image moments, which approximates (not fits) the image. This method is discussed in detail in Chapter 6. The characteristic size of Cherenkov images is 1-2° with a scale of meaningful structure measurable to $> 0.2°$ [158]. By the standards set by other branches of astronomy the optical quality of mirrors used for Cherenkov astronomy can be quite crude. This allows the use of PMTs of a few tenths of degrees diameter with mirror PSFs to match. The IACT has proved very successful over the last decade and improvements in hardware and analysis methods now allow hadron rejection of better than 99% and gamma ray energy thresholds below 300 GeV.

A summary of the characteristics of IACT telescopes currently in operation is shown in table 4.2. The longest established of these experiments is the 10m reflector of the Whipple collaboration. The Whipple group pioneered the IACT

Table 4.2: Characteristics of IACT telescopes. Where telescopes include different sizes of PMTs in their detectors only the numbers and resolution of the smallest have been shown.

Experiment	Mirrors		Detectors			Threshold
	Area(m^2)	PSF(°)	# PMTs	Resolution(°)	FOV(°)	(GeV)
CANGAROO	11	0.1	256	0.18	3.0	1500
CAT	18	0.1	546	0.125	4.8	250
Durham Mk.6	3×42	0.39	91	0.25	3.5	300
Whipple	75	0.15	331	0.23	4.8	250

in the 1980s and still uses its long serving optical reflector which was first used for Cherenkov astronomy in 1968 [157] (figure 4.2a). Its camera has increased in size and angular resolution since its initial configuration of 37×0.5° PMTS with a 3.5° field of view. The camera has recently been upgraded to comprise 331×0.23° PMTs with a 4.8° field of view [161]. The highest resolution camera currently used for Cherenkov astronomy is used by the CAT collaboration in France, a diagram of which is shown in figure 4.2b. It consists of 546×0.125° PMTs surrounded by a ring of 54×0.3° PMTs [137], [9]. The telescope uses nanosecond fast state of the art electronics and coupled with its high resolution this allows a low triggering threshold and excellent gamma/hadron discrimination. The CANGAROO telescope has an ex-lunar ranging mirror which was resurfaced in late 1997 to reduce the threshold by a factor of ~2 to its present value of ~1.5TeV. The detector uses square 0.18° PMTs arranged on a 16×16 grid.

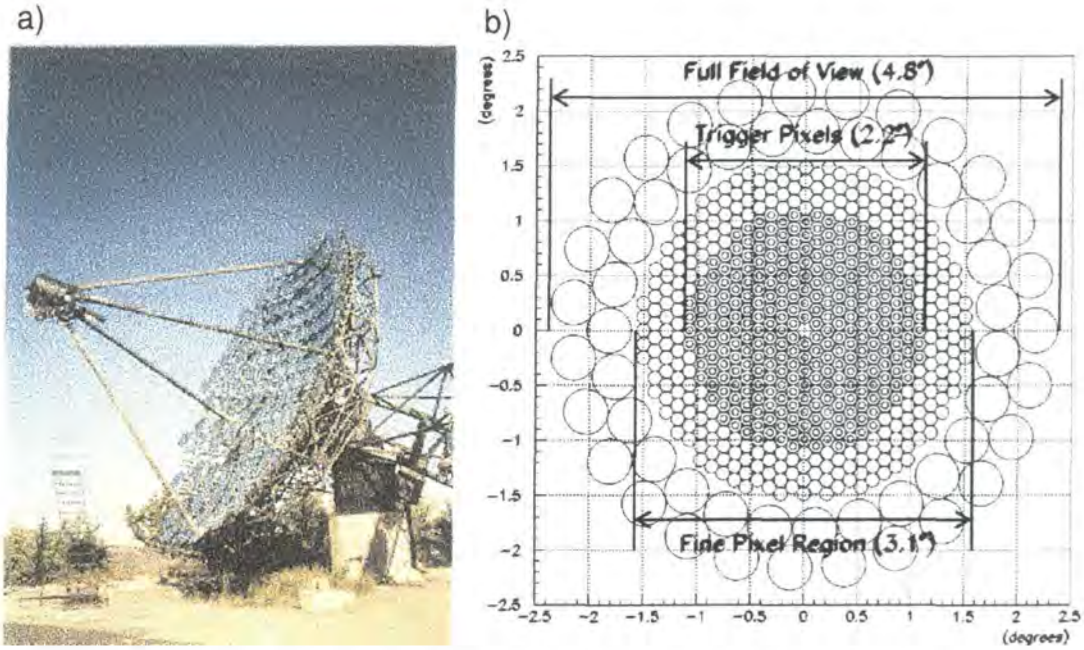

Figure 4.2: a) The 10m reflector of the Whipple observatory Cherenkov telescope (from Whipple 1999). b) The CAT collaboration imaging camera (from Barrau et al. 1998).

The collaboration plan to construct a new 7m mirror and large 512 element camera to reduce the threshold of gamma ray detection by an order of magnitude [114], [149].

The Durham Mk6 telescope is discussed in more detail in Chapter 5. Although the telescope uses the IACT it is different to other telescopes in that it has three 42m^2 reflectors. The central mirror focuses light onto a high resolution imaging camera and the telescope was designed so that the IACT could be used on the information from this detector. The outer two mirrors have $19\times0.5^\circ$ resolution PMTs which each view the same area of sky as a group of seven 0.25° PMTs in the central camera. The groups of overlapping PMTs are used for the basis of a coincidence trigger to allow the PMTs to be run at high gain, as shown by equation 4.8. The coincidence trigger gives the Mk6 telescope at sea level approximately the same threshold as the CAT and Whipple telescopes at mountain altitude. In addition the information from the low resolution 'Left/Right' detectors may provide extra information to that obtained by the central camera. In Chapter 6, ways of using this information to improve the telescope's gamma/hadron discrimination power will be discussed.

4.4.2 Stereoscopic Arrays

If two identical, well separated, Cherenkov telescopes are used independently to observe the same source using the IACT, then the amount of data recorded is increased by a factor of two. The effect of this on the value of N_σ in equation 4.6 is an increase by only a factor of $\sqrt{2}$ — a poor return for a 100% increase in financial cost. There will be no further improvement in gamma/hadron discrimination or energy threshold unless the telescopes can be operated together in some way. It was shown in equation 4.8 how operating detectors in coincidence allows a lowering in threshold energy. This method will create maximal improvement in N_σ when the fields of view of the two telescopes exactly overlap.

An improvement can be obtained by separating the telescopes, by several tens of metres, and trading off an increase in threshold energy for improved gamma/hadron discrimination. By operating coincidence trigger systems between the two separated telescopes high background rejection can be obtained *in hardware.* The large fluctuations and low photon density in a hadron induced Cherenkov event make it less likely that a hadron will trigger a widely separated system, where as the trigger rate for gamma rays will remain high.

Data which passes the trigger in a stereoscopic system can be used to provide a 'stereo' image of the same Cherenkov event. This allows a three dimensional reconstruction of the EAS to be made which provides an accurate calculation of the shower angle and core location (e.g [102]). Consider two similar Cherenkov telescopes, positioned at A and B, observing the same source position with good steering accuracy (figure 4.3a). The shower angle, $\surd(\theta_x^2+\theta_y^2)$, can be calculated by superimposing the Cherenkov images, described by the IACT, in the image plane. For accurately imaged EAS, with minimal development fluctuations, the shower axis will be projected onto a line coinciding with the image's major axis. The intersection of the superimposed extrapolations of the images' major axes gives the co-ordinates of the shower axis in the focal plane (figure 4.3b). The angular resolution of this calculation is limited by the uncertainties on the measurement of the images and requires accurate knowledge of the direction of the optic axes of the telescopes. A similar technique can be used to determine the shower's core location by extending the image major axes from A and B (figure 4.3c). The angular resolution of these methods becomes poor if the major axes of the images are approximately parallel.

For gamma ray EAS from a point source, in the absence of fluctuations in shower development and the imaging process, the shower angle ≈ 0. By assuming that the centre of the images describes the position of shower maximum in the image plane, measurement of the core location allows the height of shower maximum to be calculated. Figure 4.4 shows how the height of maximum of a gamma ray EAS could be determined (in one dimension). It is clear that the

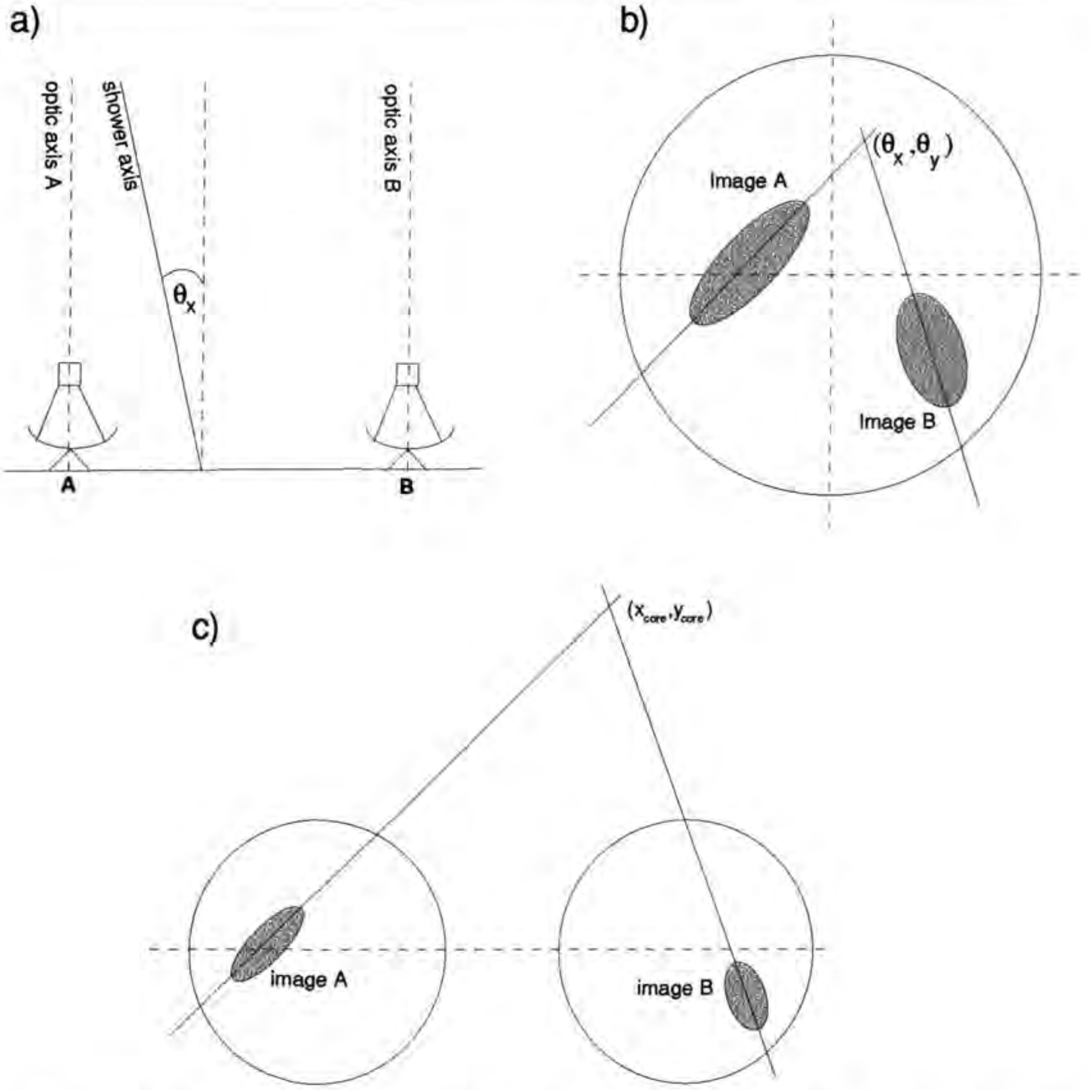

Figure 4.3: Stereoscopic imaging of EAS (after Kohnle et al. 1996). a) Two telescopes positioned at *A* and *B* image the Cherenkov light from the an EAS. b) The shower angle can be found by the intersection of the superimposed images' major axes. c) The core location can be found by a similar method.

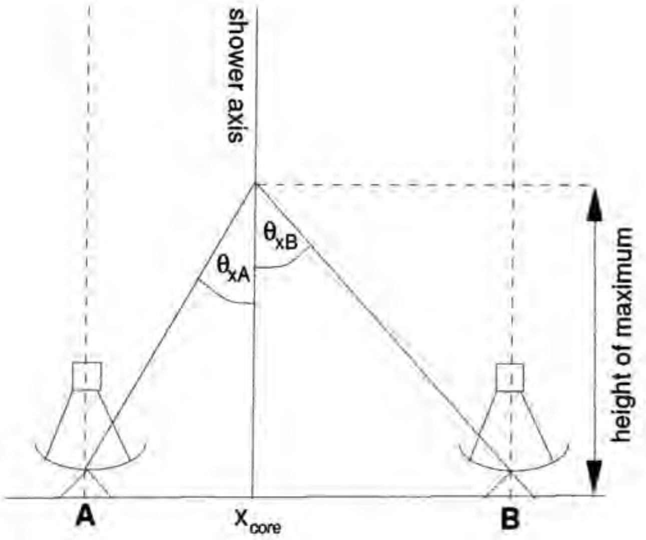

Figure 4.4: Stereoscopic determination of the height of shower maximum for gamma ray EAS.

height of maximum, h, is given by

$$h = \frac{A - x_{core}}{\tan\theta_{xA}} = \frac{x_{core} - B}{\tan\theta_{xB}} \tag{4.9}$$

where θ_{xA} and θ_{xB} are the angular distances of the centres of the Cherenkov images from the centres of the image planes A and B respectively.

Several research groups have experimented with the use of two Cherenkov telescopes to make stereoscopic measurements of EAS (e.g. [26], [36], [58]). The accuracy of the estimation of the shower angle can be improved if images from more than two telescopes are combined. The HEGRA IACT system, based on the Canarian Island of La Palma, has operated an array of four 8.5m^2 telescopes each with 271 × 0.25° pixels arranged in detectors with 4.3° fields of view (figure 4.5).

Three of the telescopes are positioned at the corners of a right angled iso-

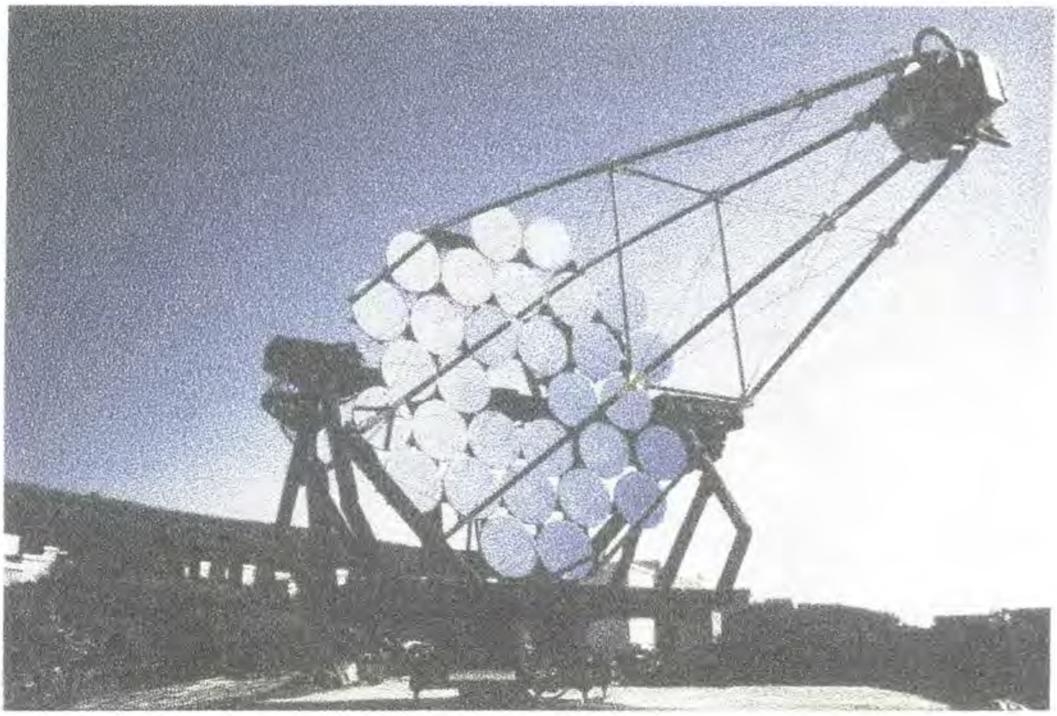

Figure 4.5: Element 'CT3' of the HEGRA IACT system (from HEGRA 1999).

sceles triangle, each ~70-80m away from the fourth telescope which is positioned at the mid-point of the hypotenuse of the triangle. The triggering criteria for the telescope varies, although a two stage coincidence configuration has proved successful in detecting a greater fraction of available gamma ray than hadron initiated events [24], [52]. The first stage requires that two neighbouring pixels in an individual telescope pass a discriminator threshold in a 12ns interval. The second requirement is that at least two of the four telescopes pass the first stage of the trigger in a 70ns interval. The HEGRA group have reported the ability to detect a significant gamma ray signal from the direction of the Crab Nebula in ~10h from the events triggering the array, without the need for any further analysis [51]. A single 'scaled width' parameter, depending on image brightness and position of the image centre in the camera, of images from individual telescopes can be used to increase the quality factor of a detection. The energy threshold of the system is estimated to be > 500GeV. At higher energies the group have made detailed calculations of the energy spectra of two AGNs, Mrk 421 and Mrk 501 up to ~20TeV [103].

The Durham Mk3 and Mk5a Stereo System

The Durham group have operated a pair of $3 \times 10\text{m}^2$ triple coincidence ACTs as a stereo pair. The Mk3a and Mk5a telescopes (figure 4.6) are located on an E-W line and separated by 100m at the Narrabri site and have been described in various texts [20], [22], [36], [143]. For an event to trigger either telescope it must cause a coincident signal in corresponding pairs of 0.7° PMTs in the outer detectors along any one of 19 1-inch PMTs (pixel size 0.5°) in the central camera. The signals must occur within 8ns for the coincidence to register. Each telescope has an energy threshold of ~200GeV and detects events at a rate of ~2 Hz at the zenith. Around 45% of all the events will be recorded simultaneously in both telescopes. These 'stereo' events are identified off line with the use of an accurate site wide time standard (Rb oscillator) which stamps a time to each event when it is recorded.

The medium angular resolution Mk3a and Mk5a telescopes used a variant of the IACT outlined in [34]. This involves calculation of the moments $\overline{x}, \overline{y}, \overline{x^2}, \overline{y^2}, \overline{xy}$ based on the selected signals from PMTs where a signal/noise threshold has been passed. A full discussion of the moments method of analysing IACT images is given in section 6.2.

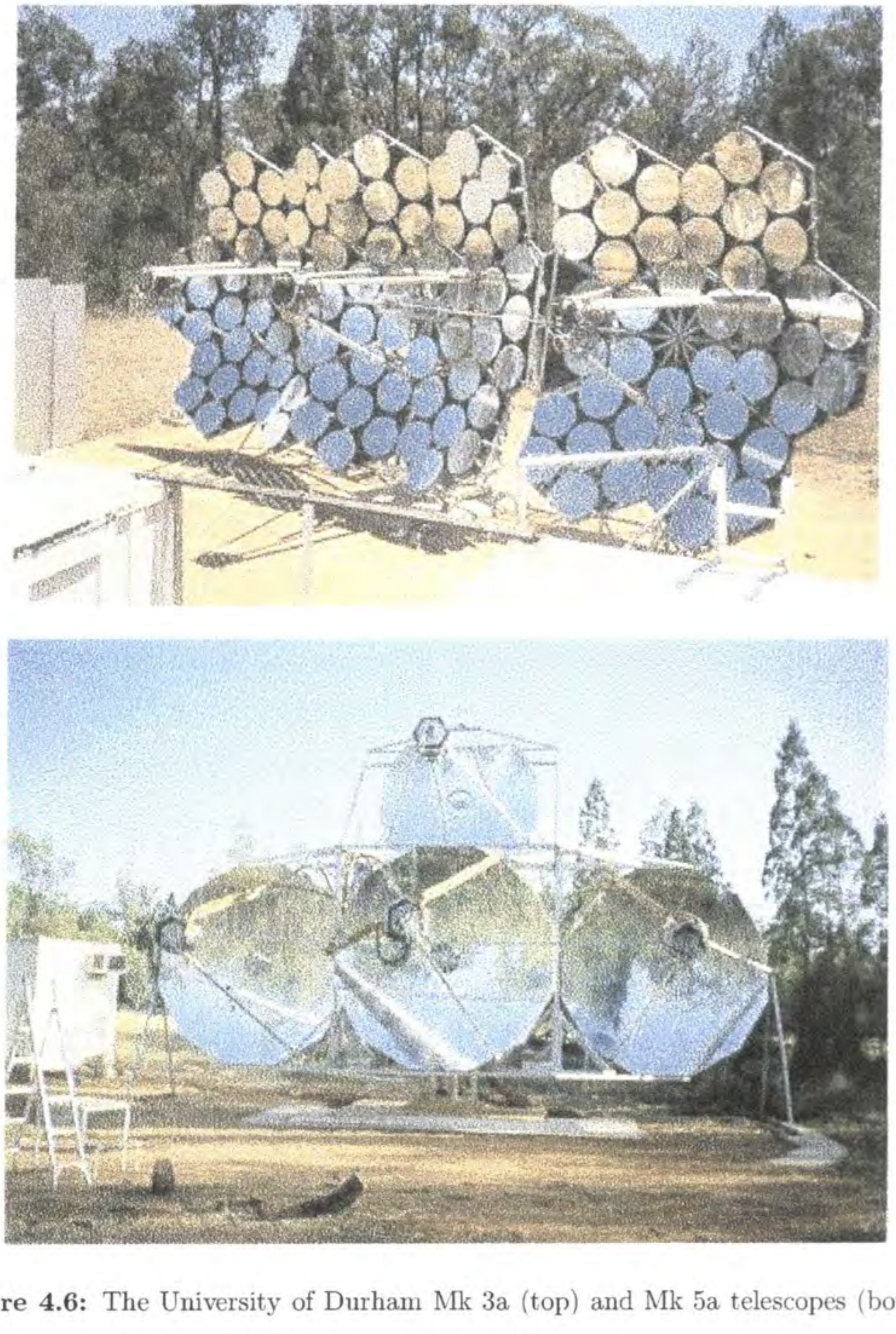

Figure 4.6: The University of Durham Mk 3a (top) and Mk 5a telescopes (bottom) at Narrabri NSW (from Durham 1999).

The height of maximum of gamma ray EAS was shown to vary less than it does for hadron EAS in section 3.2.3. The variance in the height of maximum of hadron EAS is further increased since the particles arrive at Earth at random angles rather than vertically as they do for gamma rays. The centroid, described by $(\overline{x}, \overline{y})$, of a Cherenkov image in the focal plane of a detector gives a line along which the maximum of the EAS lies. The intersection of such lines from two or more separated detectors gives an estimation of the height of maximum. The height of maximum parameter of EAS, H_c, was calculated using this method with the Mk3a and Mk5a telescopes. Due to measurement uncertainties in the centroid position the lines rarely intersect and it is necessary to use the point of closest approach of the lines. At a zenith angle of 30° the expected range of H_c for gamma rays is 8.8-11.5km [36]. A limitation of this method is that it takes no account of the variation of H_c with the primary energy of the gamma rays.

More use can be made of the available information if the primary energy of the EAS is known. The separation of the centroid of the Cherenkov image measured in one telescope and the position predicted by the measurement of the centroid in the other is known as D_{miss}. This quantity assumes that the Cherenkov image was caused by an axially falling gamma ray and uses an iterative method to calculate values for the core position and height of shower maximum. The core location is estimated by a line drawn from one telescope through the centroid of the Cherenkov image. Simulations are used to calculate the expected location of the emitting region of the EAS based on the core location estimate and a prediction of the primary energy (and hence height of maximum) of the shower based on its Cherenkov brightness. The line from the source to the emitting region is then used to calculate new values of the core location and emitting

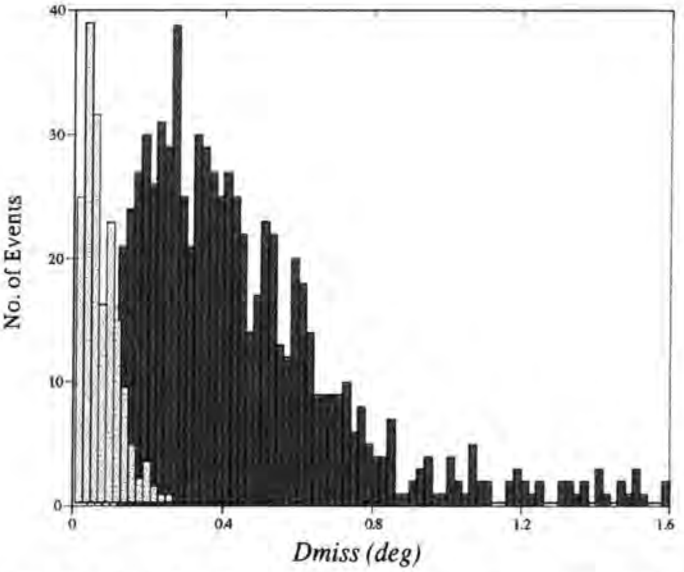

Figure 4.7: Simulated distributions of D_{miss} for gamma ray (light shaded) and hadron (dark shaded) primaries drawn from an energy spectrum between 300GeV and 1TeV (from Roberts 1999).

region. This is repeated until an emitting region position is found which gives a similar predicted centroid position to that observed in the first telescope. The final values for height of maximum and core location are used to suggest a centroid position in the second telescope. D_{miss} is the difference between the predicted and observed positions and is measured in degrees. Gamma ray EAS from a point source, which develop parallel to the telescopes' optic axes, will have a smaller value of D_{miss} than hadrons originating from a random, isotropic spatial distribution. The simulated distributions of D_{miss} for gamma ray and hadron events are shown in figure 4.7 and predict that for gamma rays $D_{miss} \approx 0$.

The third quantity which can be calculated is the variation in the estimates of the primary energy of the EAS from both telescopes, E_{Pratio}. The primary energy is estimated assuming that the Cherenkov light is from a gamma ray EAS characterised by;

1. small fluctuations in the azimuthal development of the shower,
2. a good correlation between the core distance and the centroid position and
3. a smooth lateral Cherenkov photon distribution.

The ratio of the primary energy estimates from both telescopes, calculated by the method outlined above for the calculation of D_{miss}, should be ~1 for gamma ray EAS. Since hadron EAS fall at random angles to the telescopes' optic axes, the centroid position does not provide a good estimate of the core location. This, together with much larger fluctuations in Cherenkov brightness, makes estimation of hadron primary energy uncertain giving a large spread to the distribution of E_{pRatio}. Simulated distributions of E_{pRatio} are shown in figure 4.8.

Observations of the cepheid variable AE Aquarii were made in 1993 with the Durham Mk3a and Mk5a telescopes [19]. A 4200s outburst of emission, pulsed at the second period of the white dwarf rotation period, was detected by each (but not both) of the telescopes. After analysis the chance probability of the pulsed emission was 6×10^{-7}. The data also comprised a set of 2786 events observed by both telescopes simultaneously. Before any attempt to enhance the signal was made 4.5% of the events where at the pulse period, a chance probability of 3×10^{-3}. The distributions of the pulsed signal strength for H_c, D_{miss} and E_{pRatio} are shown in figure 4.9. There is clearly an excess of events in the regions of the parameter values predicted for gamma rays by the simulations.

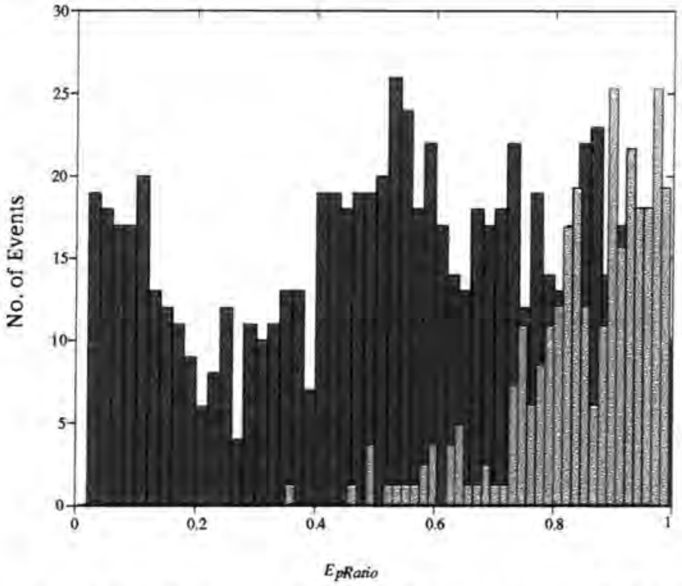

Figure 4.8: Simulated distributions of E_{pRatio} for gamma ray (light shaded) and hadron (dark shaded) primaries drawn from an energy spectrum between 300GeV and 1TeV (from Roberts 1999).

4.5 Summary of Recent VHE Observations

The first detections of VHE emission from astronomical objects were made in the early 1970s following observations of galactic objects (e.g. the Crab Nebula [61] and Cygnus X-3 [156]). The earliest detections were of low significance and often relied on detecting pulsed emission to identify a source. Coupled with the highly transient nature of many of the objects, such as the XRBs [119], it was difficult to confirm detections. Advances in ground based astronomy in the last ten years or so, led by the identification of the Crab Nebula as a standard VHE candle, have led to the creation of highly sensitive detectors and techniques. Table 4.3 shows a catalogue of sources which have been detected by the IACT at a significance greater than the 6σ level and published in a refereed journal. Included are

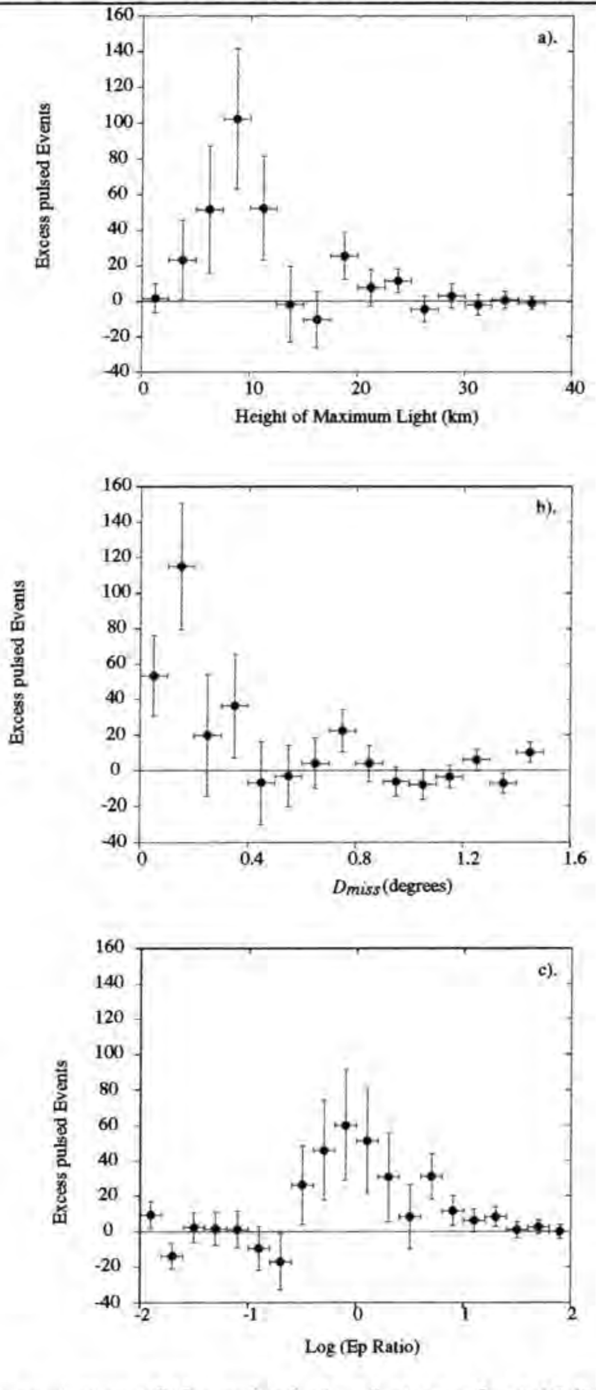

Figure 4.9: The variation of the pulsed signal strength at 16.5s for events selected on a) H_c, b) D_{miss} and c) E_{pRatio} (from Chadwick et al 1996).

Table 4.3: Catalogue of VHE emitting objects detected using the IACT. Key for object type: Plerion (Pl), X-ray selected BL Lacertae (XBL), High Mass X-Ray Binary (HMXRB), Cepheid Variable (CV) and SuperNova Remnant (SNR).

Object Name	Object Type	RA (°)	dec. (°)	Detection	Confirmation
Crab Nebula	Pl	83.52	+22.19	[160]	YES
Vela Pulsar	Pl	128.84	-45.18	[166]	NO
Markarian 421	XBL	166.11	+38.21	[132]	YES
Centaurus X-3	HMXRB	170.31	-60.62	[38]	NO
SN1006	SNR	225.58	-41.73	[150]	NO
Markarian 501	XBL	253.47	+39.76	[134]	YES
PSR B1706-44	Pl	257.39	-44.52	[97]	YES
PKS 2155-304	XBL	329.72	-30.22	[40]	NO
1ES 2344+512	XBL	356.	+51.4	[29]	NO

references for the first detection and whether the detection has been confirmed by an independent research group. Historical catalogues of VHE sources exist elsewhere (e.g. [110]). Many of the sources detected by first generation Cherenkov telescopes have not been detected using the IACT. In particular the XRB systems are notable in their absence from table 4.3, with only Cen X-3 detected [38]. The low significance and highly transient nature of the old galactic sources may indicate that their initial detection was subject to statistical fluctuations. It is also true, however, that VHE observations with sensitive IACT telescopes have concentrated on AGN in the Northern hemisphere, well away from the Galactic Plane (GP). Proposed large field of view IACT telescopes for the Southern Hemisphere, such as the HESS array of 16 telescopes [89], will be able to perform long survey observations of the GP and be better able to detect low brightness, transient sources.

Chapter 5

THE DURHAM UNIVERSITY MK6 GAMMA RAY TELESCOPE

5.1 Introduction

The Durham University Mk6 Atmospheric Cherenkov Telescope (figure 5.1) is the latest in a series of triple-dished VHE photon detectors made by the gamma ray astronomy group at the University of Durham and has been operational since 1996. It is located in Narrabri, New South Wales, Australia and sited on an East-West line joining the older Mk3 and Mk5 telescopes and is described fully in [6], [37].

The Mk6 telescope is of international importance as an operational, low threshold, Southern Hemisphere gamma ray telescope and is, with its three 42m^2 dishes, currently the worlds largest Cherenkov telescope. The telescope was designed to detect $\sim$200GeV gamma rays incident at Earth and to achieve good discrimination between gamma rays $>$ 300 GeV and the hadron background.

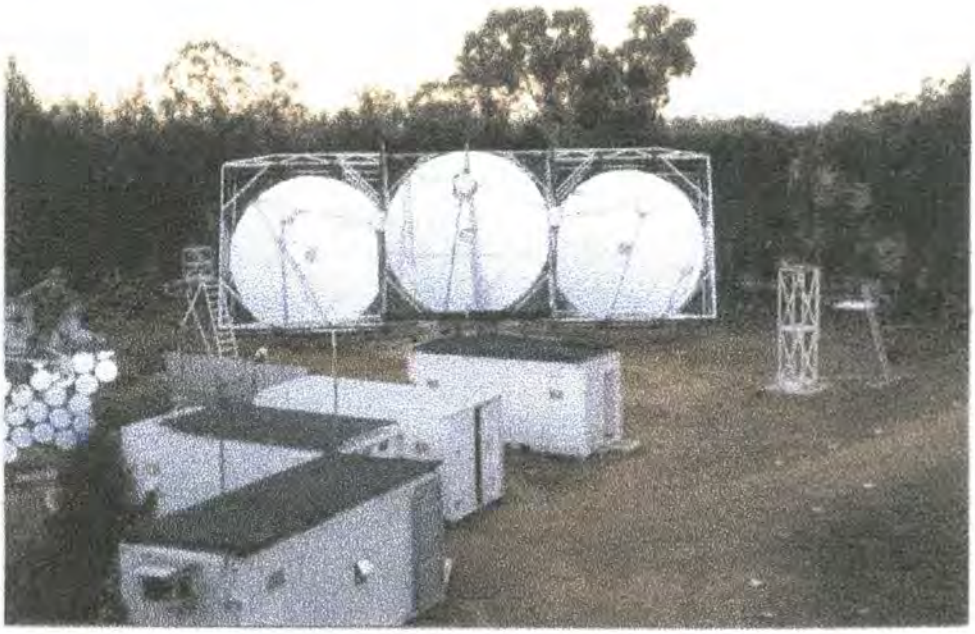

Figure 5.1: The Durham University Mk6 Gamma Ray Telescope currently deployed in Narrabri, NSW, Australia.

5.1.1 Advantages of a 3-Fold Coincidence System

The three-dished design of the Mk6 telescope involves a multiple pixel PMT array at the focus of each dish and was designed to; (i) increase the number of Cherenkov photons detected by allowing a factor of three increase in mirror area, (ii) to reduce the number of accidental (night sky) triggers by employing fast coincidence techniques between the detector packages and thus reduce the threshold of detectable gamma ray primary energy. This design has several other advantages; single cosmic ray muons emit Cherenkov light resulting in a narrow annulus of light at ground level which may trigger single dished ACTs. It is unlikely that the light from such an event landing near to the telescope will trigger a 3 dished telescope if the resolution of the detector arrays and distance between them is suitable. In addition it is impossible that the signal caused by a charged muon actually passing through a single detector will trigger a three-dished telescope. Another advantage is that the information about an event received by the telescope is potentially increased by a factor of three if all detectors have the same resolution PMT array.

5.1.2 Mirrors

Each of the light collecting dishes in the Mk6 telescope consists of 24 segments, which are manufactured from an Aluminium honeycombed material [53]. The honeycomb segments are backed with *Dural* sheet and have an anodised Aluminium sheet face which forms the reflective surface of the mirror segment, shown in figure 5.2. Aluminium mirrors of this construction are considerably lighter than glass mirrors of the same size and are an economic choice; not only is the material cost considerably less but the light weight of the aluminium means that savings can be made on telescope frame construction and steering power requirements. The mirrors have total reflectivity in the 300 - 500 nm range better than 80%. Similar mirrors have been used on previous Durham telescopes for ~10 years without any significant deterioration in reflectivity. The completed mirrors are paraboloid in form (chosen to be isochronous across the focal plane) and have a focal length of 7m and an aperture of $f/1.0$.

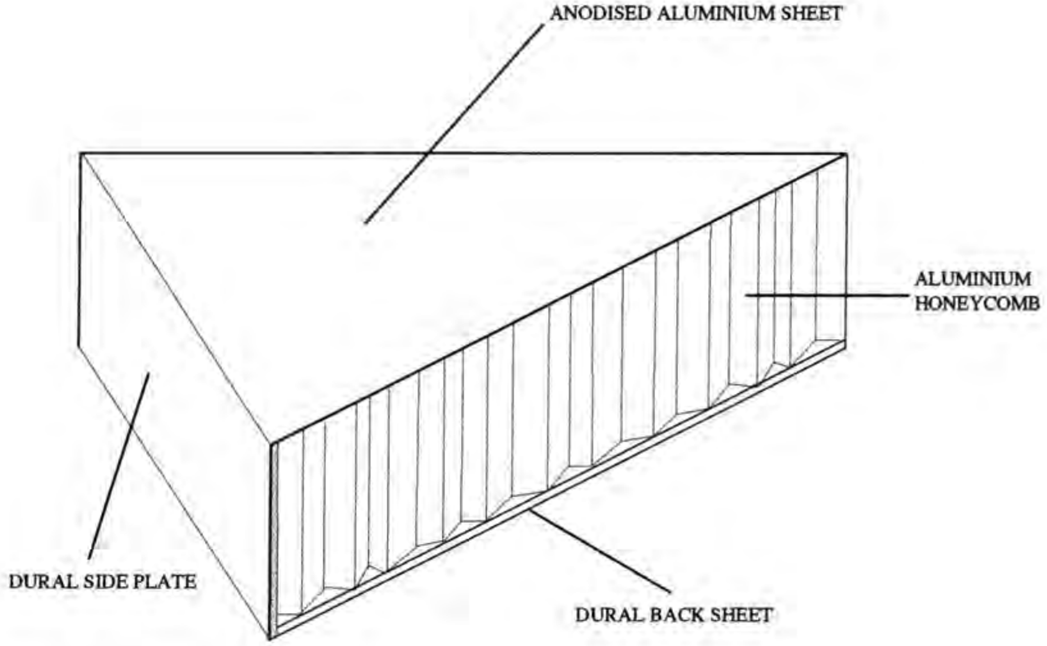

Figure 5.2: Cross-section of Aluminium honeycomb mirror segment (from Holder 97).

Point Spread Function

The Point Spread Function (PSF) of the Mk6 telescope's central dish has been measured by taking a CCD picture of a stellar image at the detector's focal plane. The PSF image is shown in figure 5.3 and has ellipticity (width/length) $> 90\%$. The best fit to a central cross-section of the image is found to be a two component gaussian curve of the form

$$f(x) = A \exp \frac{-x^2}{a} + B \exp \frac{-x^2}{b}, \tag{5.1}$$

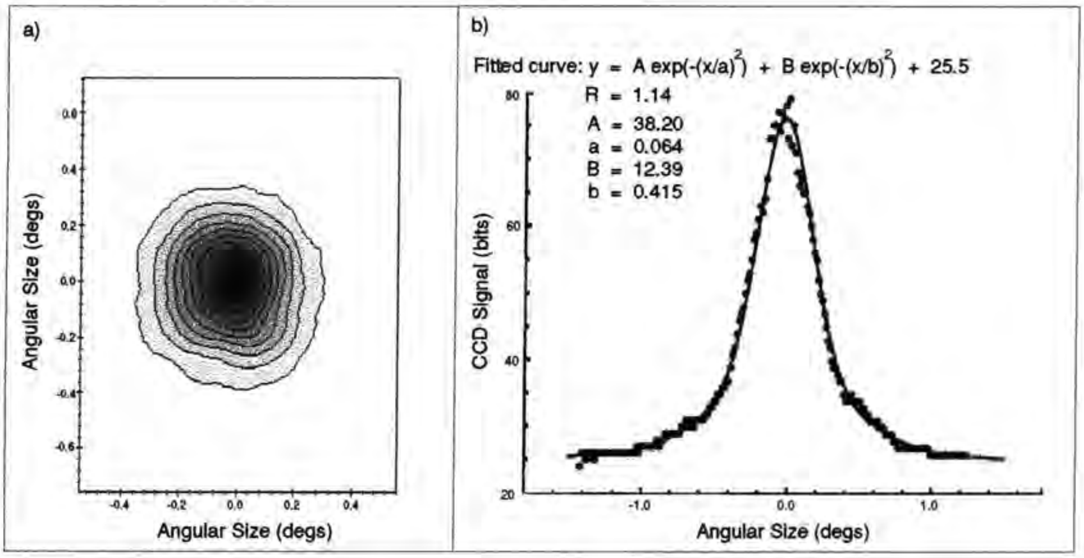

Figure 5.3: The Point Spread Function of the central mirror of the Mk6 telescope. a) A CCD stellar image recorded with the telescope, b) two component gaussian fit to a horizontal cross-section of the image.

where

$$\begin{aligned} A &= 38.20 \\ a &= 0.064 \\ B &= 12.39 \\ b &= 0.415. \end{aligned}$$

The angular size of each component of the PSF can be found simply from the standard deviation, $\sigma_a = |\sqrt{a/2}|$ for the central component and similarly for the outer component or 'skirt'.

The central component of the PSF is comparable to the resolution of the central imaging camera with standard deviation $\sim 0.18°$. The outer component, or 'skirt', has standard deviation $\sim 0.45°$ and the volume integral of the PSF suggests that $\sim 2/3$ of the light is contained within the skirt. The standard deviation, σ_{psf} of equation 5.1 can be found from the square root of the variance,

$$V(x) = \frac{\int f(x)x^2dx}{\int f(x)}. \tag{5.2}$$

Putting the values from the fitted components into the above gives σ_{psf} of 0.39° . 30% of the total light is contained within a 1-inch PMT radius of the peak of the PSF.

Mirror Performance

A disadvantage of the low weight Aluminum mirrors is that they are radiatively well coupled to the night sky. When observing near the zenith on cold, humid nights the surface temperature of the mirrors can drop below the dew point. The resulting condensation that forms in tiny droplets on the mirror surface severely reduces the reflectivity of the mirrors. To combat this the mirrors are sprayed with a solution of water and commercial rinse-aid at the start of observing runs when environmental conditions suggest that 'misting' may be a problem. This stops the formation of droplets of water which run off the mirror surface. A more difficult problem is that of freezing on cold winter nights, when moisture on the surface of the mirrors turns to ice and again severely reduces their reflectivity. These effects reduce the duty cycle of the telescope during the winter months when the nights are longer with generally better sky clarity than at other times of the year. At present experiments are being carried out with large gas heaters being used to slightly warm the mirror surface. Although relatively expensive to run the heaters have shown to be successful at reducing misting and hence freezing. An extra 2-3 hours of observing per night during the winter months could provide a 10% increase in logged data.

5.1.3 Steering

The three flux collectors are supported by an alt-azimuth mount to allow a source to be tracked through the sky and the attitude of the telescope is recorded in zenith and azimuth to a resolution of 0.022° . The position of the telescope is also calibrated via a coaxially mounted CCD camera which continually monitors the position and brightness of a guide star within the $2° \times 2°$ field of view, allowing absolute position sensing better than 0.008° . False source analysis to determine a source position is found to be better than 5 arc minutes and is discussed further in section 6.2.5.

5.1.4 Detector Packages

The telescope has three pixellated PMT array detector packages; a high resolution (0.25°) camera consisting of 91 1" and 18 2" PMTs mounted at the focus of the central dish and two medium resolution triggering detectors (0.5°) viewing the left and right hand dishes, each containing 19 hexagonal PMTs. Reflective light-collecting Winston cones are mounted in front of every PMT, apart from the 18 2" 'guard ring' PMTs of the central camera. The cones reduce the telescope's threshold of detectable gamma ray energy by increasing the amount of light collected and improving the temporal response of the triggering detectors. The central camera and one of the triggering detector packages are shown in figure 5.4

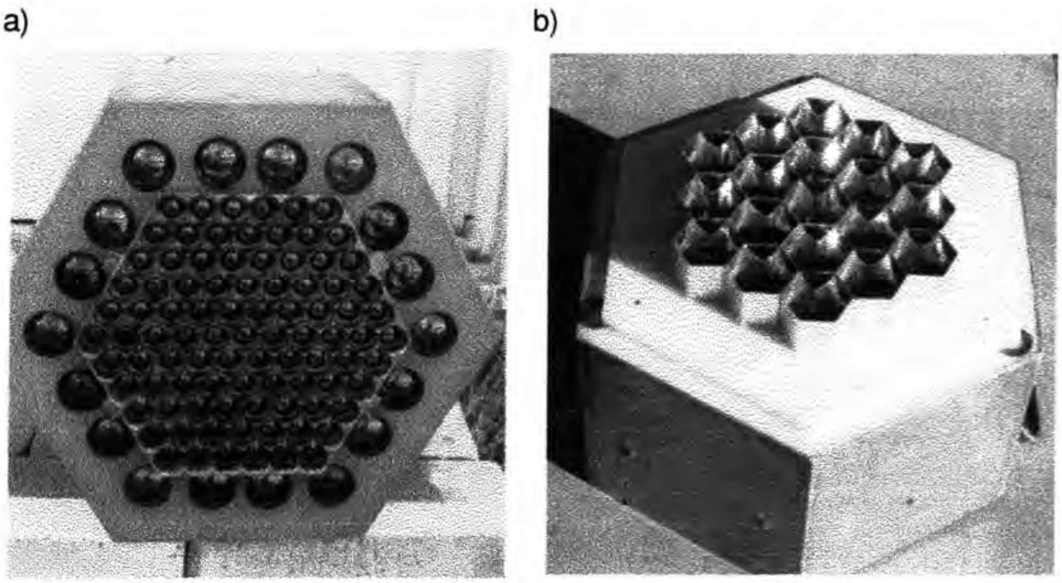

Figure 5.4: a) The central high resolution camera and b) one of the medium resolution detector packages are shown with their light collecting cones.

5.1.5 Triggering

The fields of view of the high resolution region of the central camera and the triggering detectors overlap with the PMTs arranged so that corresponding hexagonal tubes in the left and right detectors view the same area of sky as a group of seven 1" PMTs in the central camera. A four-fold temporal and three-fold spatial trigger is applied requiring both corresponding left and right PMTs plus any two adjacent 1" tubes from the appropriate group of seven to pass a discriminator threshold (figure 5.5). Very fast electronics decide on a trigger within 10 ns.

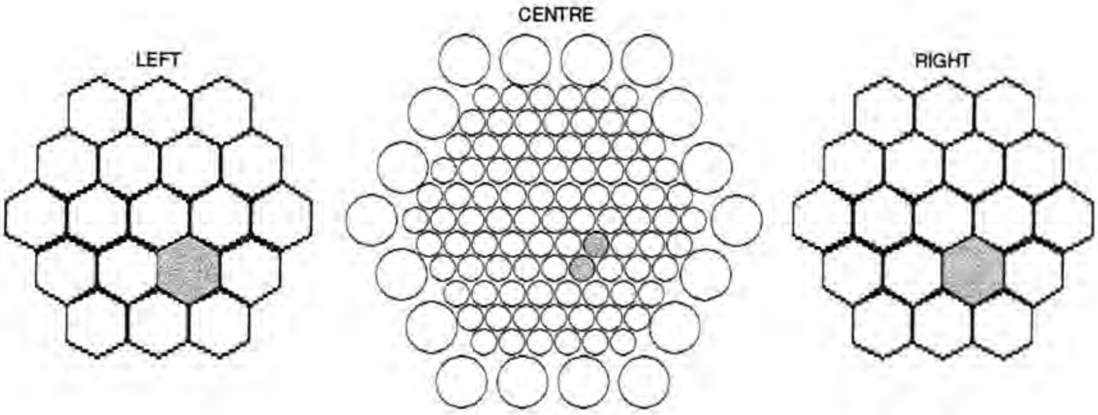

Figure 5.5: The Mk 6 telescope trigger requires three-fold spatial coincidence between two adjacent central camera PMTs and the corresponding hexagonal PMTs of the left and right detectors.

5.1.6 Energy Threshold of the Telescope

The Effective Sensitive Area (ESA) of a Cherenkov telescope was shown to depend on the distance the Extensive Air Shower (EAS) is away from the observer in section 4.3. Therefore the ESA is a function of primary energy and zenith angle. Simulations have been used to find the energy threshold of the Mk6 telescope at $\theta = 20^\circ$ [90]. The discriminator level in the modelled telescope electronics is adjusted so that the rate of simulated triggers from an assumed cosmic-ray spectrum matches observational data. The ESA of section 4.3 is a simplification assuming that all events are detected. In reality there is an efficiency attached to the trigger rate with the less Cherenkov bright, low energy events having a smaller probability of being detected. Once the model has been optimised to

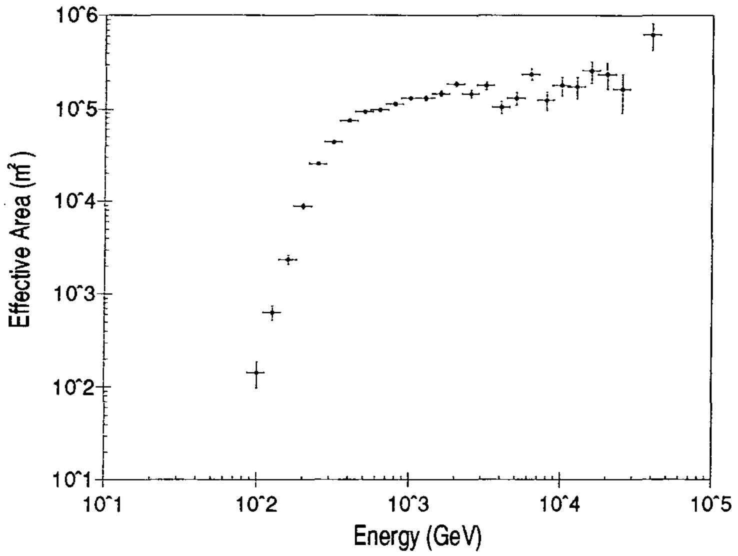

Figure 5.6: Simulated ESA of the Mk6 telescope as a function of primary energy (from Holder 97).

produce the same trigger rate as the observations it can be applied to a spectrum of simulated gamma ray events. The spectrum used in these calculations was a power law with differential index -2.4 with primary energies ranging from 100 - 10^5GeV. This spectrum is the same as the measured spectrum of the Crab Nebula in the VHE band [87]. Figure 5.6 shows how the ESA for gamma ray detection changes with energy when triggering efficiencies are considered.

The energy threshold of a Cherenkov Telescope is often defined as the the energy where the differential gamma ray flux is a maximum, i.e. the peak of the function created by multiplying the ESA as a function of energy with the differential source spectrum [3]. These calculations yielded a gamma ray threshold of (300 ± 100)GeV for the Mk6 telescope with the mean ESA above this threshold

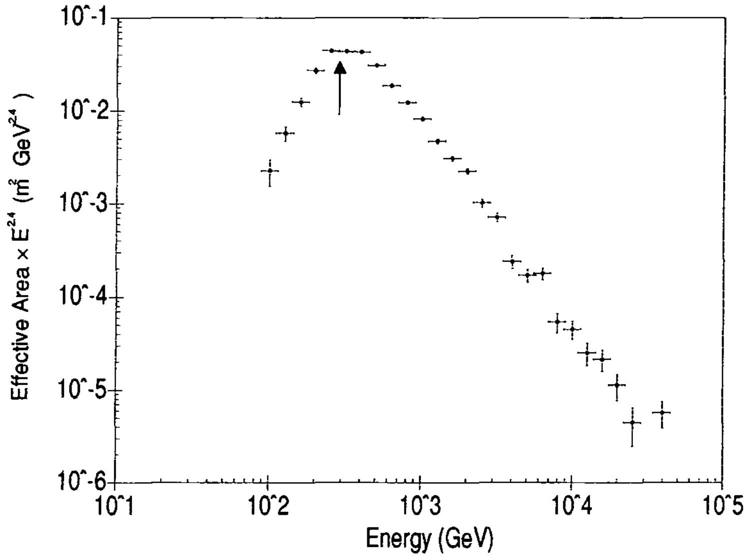

Figure 5.7: Simulated energy threshold of the Mk6 telescope (from Holder 97).

of 1.5×10^5. It should be noted however, that the telescope detects a significant fraction of events below this threshold. The values quoted here assume 100% retention of gamma rays. Because of the large flux of background cosmic-ray events further analysis of the data is necessary to improve the signal to noise ratio. A fraction of the gamma rays maybe lost during analysis which will reduce the ESA by the same fraction and hence increase energy threshold. These analysis methods are discussed in the next chapter. To accurately simulate how many gamma rays are lost requires very careful simulation of all aspects of the telescope's operating characteristics.

5.2 Operation of the Telescope

5.2.1 Observations

There are three different observing strategies which are used depending on the type of source observed, its previous gamma ray emission history and the need to observe a control area of sky.

Tracking Mode

Tracking mode follows a gamma ray source through the sky, maintaining its position at the centre of the telescope's field of view as it transits across the sky in right ascension. No control area of sky is observed, maximising the time and hence number of gamma rays detected. Thus this mode is only useful for observing sources displaying periodic gamma ray emission or where previous observations of a bright source have developed a robust analysis method which can reliably pick out gamma rays and reject all hadrons from a data set without the need for a control sample.

Chop Mode

Chop mode provides control observations of an area of sky away from the suspected source position to allow analysis routines to identify a gamma ray source by comparison with the control. The telescope tracks the source ('on-source') for a short period of time before observing a control region of space, separated from the source position by a few degrees, by returning to the same area of sky (in azimuth-zenith space) and tracking that for the same period of time ('off-source').

The Durham group currently chops in 15 minute sections. This ensures that the on and off source observations are separated enough so that the two fields do not over lap but are close enough together that a similar region of the sky is observed. 15 minutes is also short enough to minimise secular changes in count rate due to changing sky conditions. Observations are made in the order on-off-off-on or off-on-on-off so that adjoining on-off pairs counteract biases due to changing conditions such as sky clarity, temperature etc.

Drift Scan Mode

In Drift Scan Mode the telescope is set at a constant azimuth and zenith and the source region of sky is allowed to transit across the field of view. Observing equal angular regions either side of the source position can provide a control observation. Alternatively the method may be useful for surveying large regions of sky for transient events or observing interesting areas of space such as the galactic centre.

5.2.2 Timekeeping

A Rubidium oscillator is used to provide an accurate site-wide time standard at Narrabri and the times of individual events are recorded to relative accuracy of 1μs. This has allowed stereo analysis of events using combinations of the Mk3, Mk5 and Mk6 telescopes [143], [36]. The drift rate of the atomic clock is linear and measured by comparison to GPS [6].

5.2.3 Sky Clarity Monitoring

During an observation it is difficult to detect thin clouds with the naked eye which may affect the count rate of the telescope. The Durham Gamma Ray Group has pioneered the use of an $8 - 14\mu m$ FIR radiometer mounted on the telescope coaxially with the camera to continually monitor the radiometric temperature of the sky in the field of view [154]. A clear sky at the zenith has a temperature between -30 and -70 ° C, depending on the time of year [23]. This temperature increases with zenith angle and also with the presence of cloud or other obscuring matter. Figure 5.8 shows the radiometer measurement against count rate during an observation. The presence of a cloud in the field of view half way through the observation is clear. The radiometer provides a more sensitive probe of sky clarity than simply relying on the count rate of the telescope which is limited by statistics. Data segments with a poor radiometer trace are rejected from further analysis.

5.3 Calibration of PMT Data

5.3.1 PMT Pedestal Calibration

In the absence of a Cherenkov signal a PMT will detect random statistically fluctuating signals from the night sky background. In order that a small Cherenkov signal on top of a large negative background fluctuation can be measured the electronic units which measure the PMT signals are provided with an artificial positive DC offset. This offset is known as the pedestal and must be subtracted from the signal in order to perform an analysis of the data such as that which will

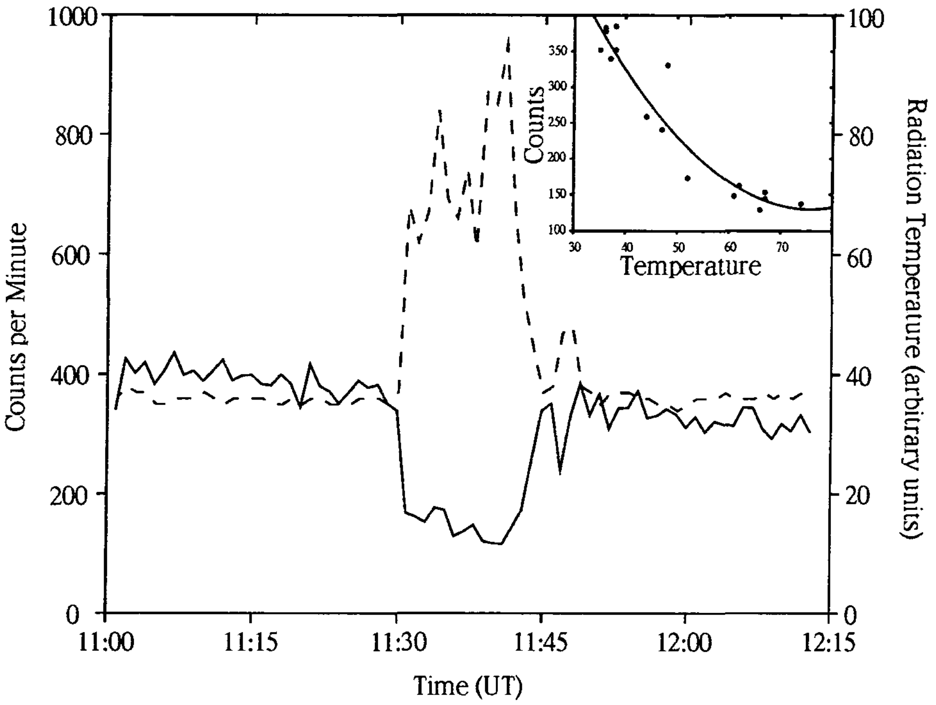

Figure 5.8: Radiometer measurement versus count rate. Inset shows correlation between count rate and radiometric temperature (from Turver 1997).

be discussed in Chapter 6. The pedestal is measured by triggering the telescope throughout an observation with a pulse generator. The pulse generator in use on the Mk6 telescope operates continually throughout an observation and triggers the telescope at random times with a mean rate of 50 per minute. Events recorded by the random trigger are unlikely to contain any Cherenkov photons and give a measure of the contribution to the recorded signal by the night sky background. The mean of the distribution of the measured random signals for each PMT gives a value for the pedestal for each data segment. In practice using the mean of this distribution as an estimate of a PMT's pedestal suffers from a systematic error which tends to over estimate the pedestal. This is because the random signal distributions contain complicated noise contributions from other sources such as the signal processing electronics and other sources of background light. Ideally the mode of the random signal distributions should be used as the value of the pedestal however in practice this is difficult to identify reliably. The mean has so far proved the most reliable estimate of the pedestal although it results in an over estimation of the value by a few percent. Work continues to identify better measures of this quantity.

5.3.2 PMT Sky Noise Measurement

An estimation of the noise on each signal recorded in a PMT is important in some methods of parameterizing events in the IACT. The standard deviations of the same random events used to identify the pedestals are taken as the noise of each PMT for each data segment in the presence of background illumination from the sky.

5.3.3 PMT Gain Calibration

The absolute gain of the PMTs and electronic channels is performed using light pulses from a radioactive ^{241}Am source contained within a plastic scintillator 'pill'. The pill produces ~3ns pulses of ~300 photons at a rate of ~1kHz and is placed at a fixed distance from each PMT in complete darkness. The pulse area spectrum is measured and allows the calculation of the absolute gains of the PMTs. During an observation, the relative gains within each detector are measured with respect to the central PMT of that detector. Throughout the observation a nitrogen laser produces randomly timed flashes of light at a mean rate of 50/min which illuminate a block of plastic scintillator. The scintillator provides short pulses of ~400nm radiation which is distributed to each dish via plastic optical fibre cable. A flashed opal diffuser at the end of each fibre produces a pulse of light which is uniform across the face of each detector and these calibration events are incorporated into the datastream and recorded as other events are. This method only allows a relative calibration to be performed as there is a variation in the number of photons per laser flash. In addition to a pulse-to-pulse variation laboratory tests have shown a decrease in laser pulse height of ~ 2.5% per °C increase [143]. An extra camera PMT is shielded from reflected light from the mirror and dedicated to viewing the laser. Pulses registered in the laser monitor PMT allows reliable identification of calibration events. This method allows the relative gains of all tubes within a 15 minute data segment to be measured to better than 2% accuracy.

5.4 Summary

The construction of the University of Durham Mk6 telescope was completed in March 1995 and the telescope has been fully operational since 1996. It consists of three aluminium mirrors, each viewing a PMT detector array, on a single alt-azimuth mount. The central detector consists of a 91 element 0.25° resolution camera arranged in a close packed hexagonal array and surrounded by a ring of 18 larger 0.5° resolution PMTs. The Left and Right detectors consist of 19 hexagonal PMTs which are view 0.5° across opposite flat sides. A complex intelligent coincidence pattern trigger is operated, requiring that a set of signals from spatially corresponding PMTs in all three detectors pass a discriminator threshold in a short time bin. Triggers due to the night sky background are minimised allowing the PMTs to be run at high gain. The telescope operates at a background count rate of ~1000/min (near the zenith) and simulation studies have suggested that a significant number of gamma ray events will be detected at 150GeV. The telescope uses the IACT to separate gamma rays from the hadron induced background on the basis of the appearance of the Cherenkov images in the central camera. This is done by the calculation of the Hillas parameters, which are discussed in Chapter 6. It was shown in section 3.6.2 that there are different scales of Cherenkov photon fluctuations seen from gamma ray and hadron EAS when they are viewed by two detectors separated by 10-50m. The Left and Right medium resolution detectors are separated by 14m and in Chapters 7 and 8 it will be shown how information from them could be used to provide some extra gamma/hadron discrimination power to that obtained from the central camera.

Chapter 6

CHERENKOV IMAGE ANALYSIS

6.1 Introduction

In the previous chapters the design and operation of a ground based gamma ray telescope were discussed. The different ways in which gamma ray and hadron EAS develop in the atmosphere means that their images appear differently when viewed by an optical system. A schematic of the formation of a Cherenkov image is shown in figure 6.1. The Cherenkov image can be described by an ellipse, the length and width of which estimate the longitudinal and lateral development of the EAS. The position in the field of view and exact appearance of the image depends on the core position. In particular the long axis of the Cherenkov image points towards the source of the initiating particle, allowing the identification of point sources of gamma rays. The signal to noise ratio of a ground based gamma ray telescope can be greatly improved if the gamma ray and hadron events can be separated using the recorded images. This requires the identification of Cherenkov photons over those caused by background noise and the parameterization of the images in an analysable fashion. A popular method of analysing the pixellated

Cherenkov images involves the calculation of moments. The moments can then be used to describe characteristics of the image. Several useful dimensions of the Cherenkov images, such as its width and length, are known as the Hillas parameters. This chapter deals with the analysis of Cherenkov event data from pixellated detector arrays, such as those in operation on the Mk6 telescope.

6.2 The Moments Technique

A moments analysis is a method of estimation which involves the calculation of image moments that would be induced at the origin by a body, I, made up of i elements of different densities, ρ_i, positioned at coordinates (x_i, y_i). The moments calculated give statistical estimators such as the mean, based on directions within the coordinate system. In general

$$\frac{1}{N}\sum_i x_i^r \tag{6.1}$$

is called the r^{th} moment of x for a body consisting of N elements. For most applications, including those in ground based gamma ray astronomy, the following moments are used;

$$\Omega = \sum_i \rho_i \tag{6.2}$$

$$< x > = \frac{\sum_i \rho_i x_i}{\Omega} \tag{6.3}$$

$$< y > = \frac{\sum_i \rho_i y_i}{\Omega} \tag{6.4}$$

$$< x^2 > = \frac{\sum_i \rho_i x_i^2}{\Omega} \tag{6.5}$$

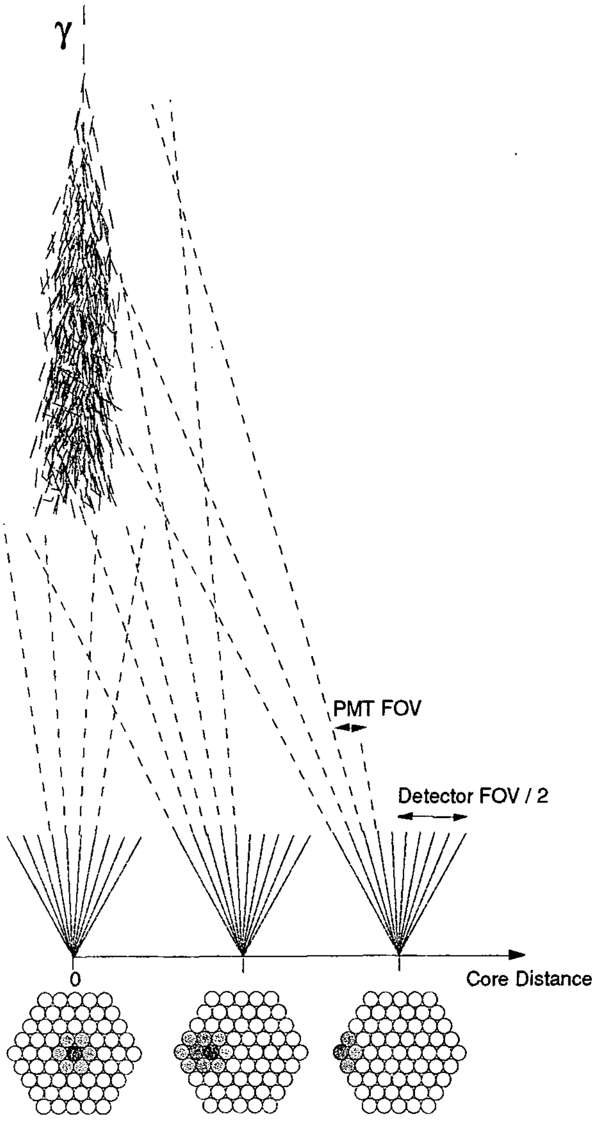

Figure 6.1: The formation of a Cherenkov image in a pixellated detector from a vertically falling gamma ray shower at various core distances. Shown are the fields of view of the individual PMTs in a line along the centre of the detector and, below them, the image (darker shading indicates brighter signals).

$$< y^2 > \; = \; \frac{\sum_i \rho_i y_i^2}{\Omega} \tag{6.6}$$

$$< xy > \; = \; \frac{\sum_i \rho_i x_i y_i}{\Omega}. \tag{6.7}$$

The variances in x, y and the cross term can be calculated;

$$\sigma^2(x) \; = \; < x^2 > - < x >^2 \tag{6.8}$$

$$\sigma^2(y) \; = \; < y^2 > - < y >^2 \tag{6.9}$$

$$\sigma^2(xy) \; = \; < xy > - < x >< y > . \tag{6.10}$$

The point $(< x >, < y >)$ is known as the 'centroid' and is measured with an uncertainty given by equations 6.8 and 6.9. If I was a solid body, then this position would describe the centre of gravity.

In gamma ray astronomy the above moments are used to produce an ellipse which describes the Cherenkov image. A pixellated PMT detector array at the focal plane of an optical system gives a density measurement of the numbers of Cherenkov photons per square degree in each PMT. Parameters describing the ellipse, such as its size and orientation can be obtained and are known as the Hillas parameters [83]. There is no reason why higher orders of moments should not be used although the uncertainties as r increases get large very quickly. If the quantity x_i has a measurement error of δx_i associated with it then the uncertainty in M_r is given by

$$\Delta M_r = r! \, \Delta M_1, \tag{6.11}$$

where ΔM_1 is the error on the first moment of x,

$$\Delta M_1 \approx \sqrt{\sum_i^N \delta x_i^2}, \tag{6.12}$$

if the δx_i are added in quadrature. The formation of images of Cherenkov events are discussed further in the next section.

The higher moments can be used to describe more abstract properties of the shower. One potentially useful gamma/hadron discriminating parameter based on M_3 has been investigated [63], [161]. In a high resolution camera, the peak brightness of a gamma ray Cherenkov image will lie somewhat nearer to the source position than the centroid of an ellipse created by the above method (see figure 6.1) [104]. This is a perspective effect; the angle between the source position and a point on the core axis of a vertically falling EAS is smaller at higher altitudes. Therefore the Cherenkov photons from high in the EAS tend to appear nearest to the centre of an imaging detector. The central PMTs view a greater spatial length of the shower than those at greater angles from the centre and therefore a larger angular density of Cherenkov photons. This is a somewhat simplistic explanation. In reality the numbers of Cherenkov photons produced at various heights in the EAS, and their angular distribution, varies with altitude and from shower to shower. The Whipple group have introduced the *Asymmetry* parameter, shown in figure 6.2, to reject hadron events which have survived their conventional 'supercuts' analyses [161]. The *Asymmetry* parameter is an attempt to quantify the skewness of the brightness profile of an image ellipse along its major axis. The success of this parameter requires a high resolution ($< 0.1°$) camera to precisely determine the brightness profile and a large ($> 4°$) field of view to ensure that the tails of events are not truncated by the edge of the camera

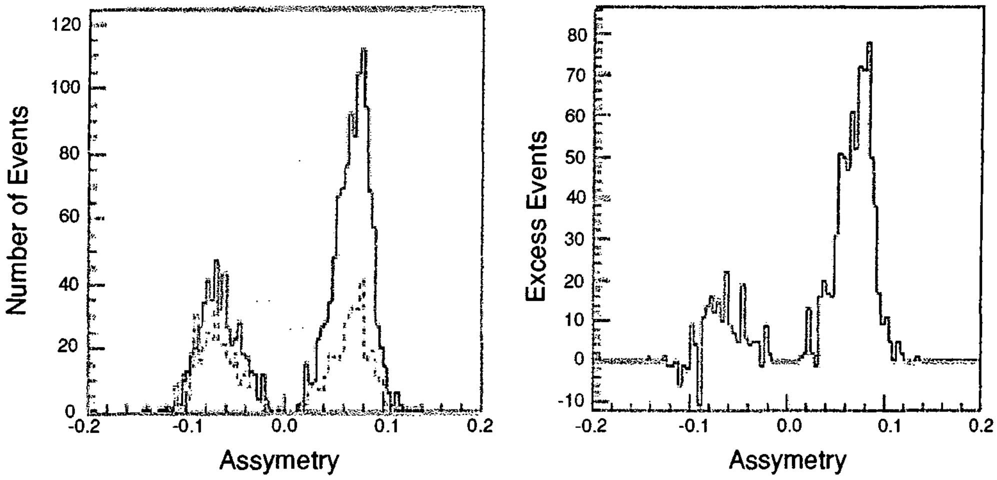

Figure 6.2: Asymmetry distributions for events passing the Whipple group's supercuts analysis. a) The On (solid line) and Off (dotted line) source distributions of the parameter are shown and b) the difference of the two plots (from Weekes et al. 1997).

[126].

6.2.1 The Hillas Parameters

Techniques of parameterizing and analysing Cherenkov events are largely due to the simulations of Hillas [83] although the idea of differentiating between gamma ray and hadron events by using their Cherenkov images was first proposed by Jelley and Porter in 1963 [95]. The Hillas parameters for the ellipse fitted to a Cherenkov event are shown in figure 6.3 and are defined as follows;

$$Distance = \sqrt{< x >^2 + < y >^2} \tag{6.13}$$

$$Width = \sqrt{\frac{\sigma^2(x) + \sigma^2(y) - z}{2}} \tag{6.14}$$

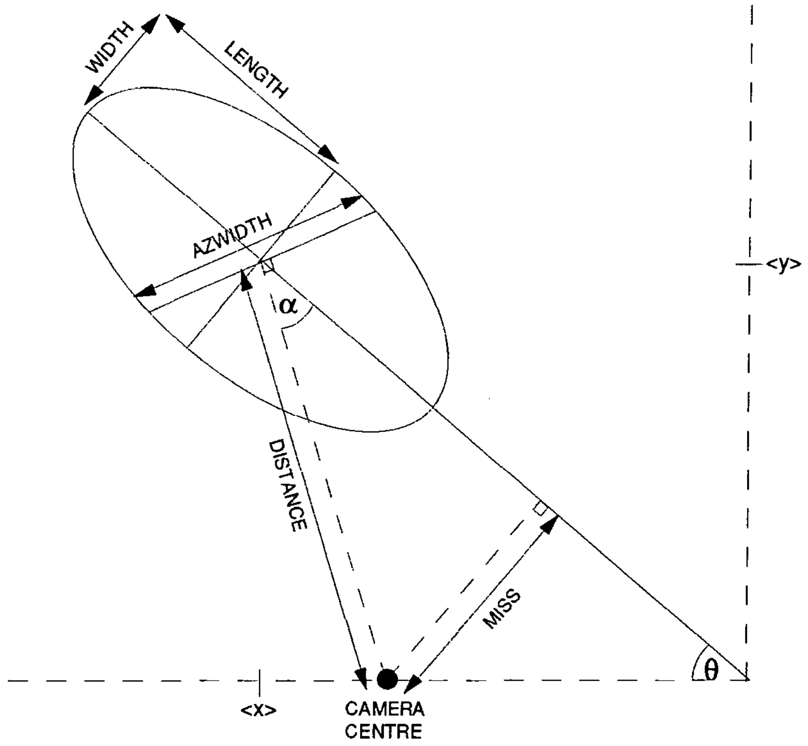

Figure 6.3: Schematic of the Hillas parameters for an idealised Cherenkov event.

$$
\begin{aligned}
Length &= \sqrt{\frac{\sigma^2(x) + \sigma^2(y) + z}{2}} && (6.15)\\
Miss &= \frac{b^2}{a^2 + 1} && (6.16)\\
Alpha &= \arcsin\left(\frac{Miss}{Distance}\right). && (6.17)
\end{aligned}
$$

The following coefficients used in the above equations have been revised in [136];

$$
\begin{aligned}
\Delta &= \sigma^2(y) - \sigma^2(x) && (6.18)\\
z &= \sqrt{\Delta^2 + 4\sigma^2(xy)} && (6.19)
\end{aligned}
$$

$$\begin{aligned} a &= \frac{d+z}{2\sigma^2(xy)} & (6.20) \\ b &= <y> -a <x> . & (6.21) \end{aligned}$$

It is important to stress that an ellipse created by the moments method and described by the Hillas parameters is not a fit to the Cherenkov image. The ellipse is the only solution to the collection of moments calculated from the available data.

6.2.2 Identification of Cherenkov Event Images

Noise fluctuations below the pedestal value of a PMT will lead to a negative signal being included in the moments calculations. It is important that only positive signals are used in calculating the moments as negative fluctuations can yield spurious results. To apply a moments analysis successfully to an IACT image it is necessary to identify which pixels contain signals dominated by Cherenkov light rather than background noise. The relevant pedestals are subtracted from each PMT so that (for a symmetrical noise distribution) the average signal recorded by a PMT during a random trigger should be 0 ± the rms noise. The noise can be used to identify the largest signals by setting some threshold level, in units of the noise, which must be passed for the pixel to be identified as part of the Cherenkov event. All pixels of an event that pass this primary criteria are known popularly as 'image' pixels. More Cherenkov light can be identified by defining 'border' pixels, which pass a dimmer selection threshold but must be adjacent to an image pixel. Image and border thresholds of 4.25 and 2.25 times the rms noise have been used by the Whipple group [62] and were optimised on observations of the Crab nebula [131]. The Durham group apply a further condition requiring that image and border pixels respectively register $> 37.5\%$ and $> 17.5\%$ of the light in the brightest pixel [6].

6.2.3 Software Padding

When observing in a chop mode the on and off fields may be of different star brightness and hence there will be different noise levels associated with events recorded from each field. The process of 'software padding' was developed by Cawley and works by comparing the same PMTs between an on/off pair and adding extra noise to the darker pixel until the noise levels match [31], [63]. This technique seems to be very efficient in removing bias induced by the starlight background without reducing Cherenkov sensitivity. All data taken with the Durham telescope is routinely software padded before analysis.

6.2.4 Gamma Hadron Separation using the Hillas Parameters

Unless a known, strong source of VHE gamma rays can be observed with a telescope it is difficult to predict how their images will appear using the IACT. Even then the gamma rays may be hard to identify due to the low signal to noise ratio and similar spectral energy distributions of the source and background events. Many groups operating the IACT have relied on Monte-Carlo simulations of their experiments to hone their analysis routines and predict their gamma ray sensitivity. A valid telescope model which accurately reproduces the images of background events is vital in achieving this successfully as it is the only test of how accurately the model may represent the gamma rays.

A schematic of the formation of an image of a gamma ray EAS by a pixellated detector was shown in figure 6.1. The shape of the image registered in the detector depends on the core distance. When the EAS core axis is the same as the optic axis of the detector array, the image is circular in appearance. As the detector is separated from the EAS core, the images appear more elongated until the core distance is so large that most of the Cherenkov photons from the shower miss the detector. The longitudinal and lateral development of the EAS gives the image its length and width. The different processes involved in electromagnetic and hadronic EAS make the two types of shower look quite different. An ellipse formed by the moments method and describing a hadron initiated Cherenkov event will tend to be wider than a gamma ray event and may also include extra light from muons passing close to the detector [86]. For observations of a point source of gamma rays, the most important parameter that can be used to reject a large proportion of hadron events is *Alpha*, the angle between the event's major axis and the line joining the event centroid with the supposed source position. The gamma ray images detected by a telescope observing a supposed source will tend to point towards the source position and hence have a small value of *Alpha*. This is a consequence of the initialising photons from a point source falling parallel to the detector's optic axis. Essentially the same effect is observed in meteor showers seen from Earth, such as the annual Leonid storms. The tracks made by the meteorites as they burn up in the atmosphere tend to point back towards their source, which is the dust tail of a comet coincident with the constellation Leo [50].

Hadron events can arrive from anywhere within the field of view and travel in random directions and can hence take any value of *Alpha*. Because *Alpha* retains information about the point of origin of the initial particle it can be used to form a map of the significance of any excess on source signal originating from a particular position on the sky. This can be done using a 'False Source' analysis which is discussed briefly in section 6.2.5. It has become accepted in the field of Imaging Cherenkov Astronomy to present results in the form of an 'Alpha plot', the histogram of *Alpha* for the total on and off source data set, showing an excess of on source events at low *Alpha*. By finding the numbers of events on, N_{ON}, and off, N_{OFF}, source that are below a cut off value of *Alpha* the significance of a detection, σ_{det}, can be found [126];

$$\sigma_{det} = \frac{(N_{ON} - N_{OFF})}{\sqrt{(N_{ON} + N_{OFF})}}. \tag{6.22}$$

Figure 6.4 shows the simulated parameter distributions of selected Hillas parameters for gamma ray and hadron events. Gamma-ray events tend to be smaller and have values of *Alpha* nearer to 0 than hadrons. There is also a large difference between the gamma ray and hadron *Azwidth* distributions; a cut of $Azwidth < 0.24$ yields a quality factor (recall equation 4.7) $Q = 1.8$. In comparison the best Q obtained with a *Width* cut is ~1.4 for $Width < 0.23°$. *Azwidth*, however, is not an effective gamma/hadron discrimination parameter since it retains hadron events that are gamma ray like. Figure 6.5 shows the *Alpha* distributions obtained after such data cuts. There is very little difference between the gamma ray and hadron *Alpha* plots after the *Azwidth* cut. Therefore it is difficult once an *Azwidth* cut has been applied to say anything about the origin of any excess events. In comparison a *Width* cut increases the relative signal strength and retains an excess of the signal at small values of *Alpha*.

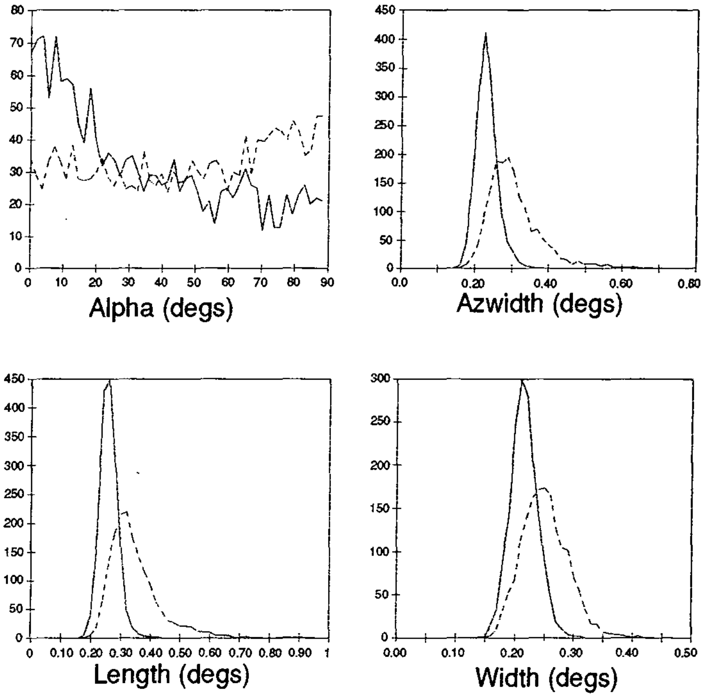

Figure 6.4: Simulated distributions of selected Hillas parameters for gamma ray (solid line) and hadron (dashed line) initiated Cherenkov events.

6.2.5 False Source Analysis

A useful method of showing that gamma ray events occur from a particular point on the sky has been shown by the CANGAROO collaboration [97]. A false source analysis divides an observation region into a matrix of positions and calculates the value of the Hillas parameter *Alpha* for shape selected events at every position in the matrix. The numbers of on and off source events with *Alpha* $< 30^\circ$ within each matrix element are recorded allowing a significance map to be produced which shows the most significant origin of the excess events. An example of a false source analysis plot is shown in figure 8.10.

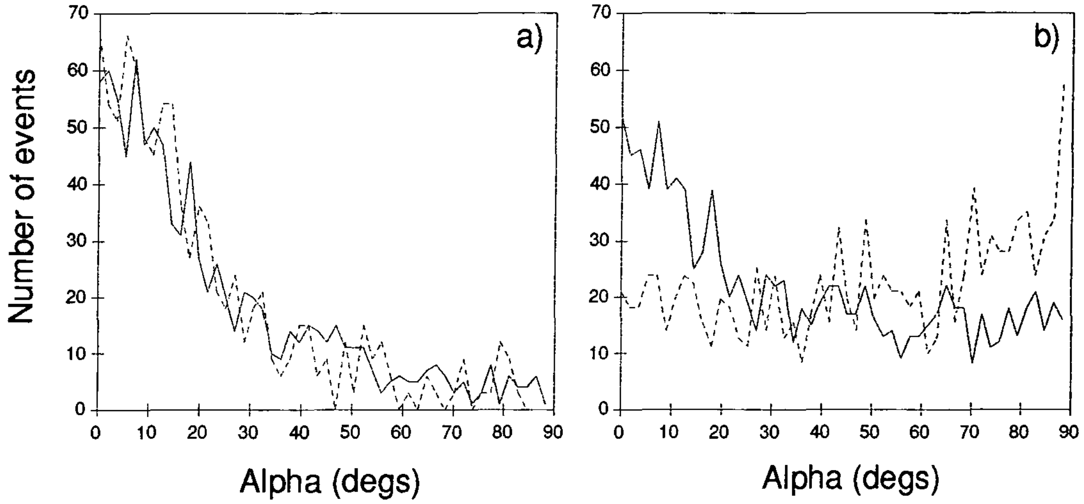

Figure 6.5: Alpha plots for simulated gamma ray (solid line) and hadron (dashed line) initiated Cherenkov images after events with a) *Azwidth* > 0.24° and b) *Width* > 0.23° were rejected. The hadron distributions have been normalised to the same area as the gamma ray distributions in each case.

6.3 Summary

The field of ground based gamma ray astronomy has benefited significantly from the construction of telescopes which can record high resolution Cherenkov images of EAS. IACT telescopes are sensitive and able to locate source positions to $< 0.1°$ accuracy. The key to this success has been in developing analysis techniques that exploit the differences between the development of gamma ray and hadron EAS based on the appearance of their images in pixellated detectors. In particular the Hillas parameters, which use the moments to construct an ellipse that describes the image, have proved successful at identifying gamma rays from the hadron background and identifying their origin.

Chapter 7

COMPOSITE CHERENKOV TELESCOPES

7.1 Introduction

The use of multiple Cherenkov telescopes to provide gamma/hadron discrimination was discussed in section 4.4.2. The 'stereo' method uses two or more telescopes separated by $\sim$100m and applies special analysis to events detected by both telescopes. Gamma/hadron discrimination can be achieved by making a trigonometric reconstruction of the shower, allowing determination of the height of gamma ray EAS maximum and making a more accurate location of primary particle origin than can be made with only one telescope. The stereo method has been successfully used by the Durham [36] and HEGRA groups [102] at energies > 200GeV and > 1TeV respectively. The technique forms the basis of several proposals for future experiments [162], [89]. In these methods, the separation of the telescopes is chosen to be large enough to allow the most accurate measurement of height of maximum whilst maximising the number of events seen simultaneously by both telescopes. This is done with separations comparable to or smaller than the size of the Cherenkov light pool. Related, non-imaging, techniques have been shown to be successful at detecting the Crab Nebula with two detectors separated by shorter distances, of the order ~20m, [152], [96]. The ability to make an accurate determination of the height of maximum is reduced with decreasing separation. Despite this, simulation studies have shown that the lateral distribution of Cherenkov photon density from hadron induced EAS fluctuate more than gamma ray events over scales of the order of 10m [49], [86], [144]. Gamma rays could, in principle, be separated from the hadron background by exploiting the larger fluctuations in Cherenkov density detected from hadron showers when viewed by detectors separated by ~10m or more.

The Durham University Mk6 Atmospheric Cherenkov Telescope's unique configuration with three pixellated detectors, was designed to provide a low energy threshold for gamma ray detection. It has been suggested however, that the two low resolution triggering packages (the Left and Right detectors) could be used to produce extra information about Cherenkov events due to their 14m separation. The 19 2-inch PMTs in the Left and Right detectors provide lower resolution information than the central camera does for imaging. However, the 14m baseline between the detectors coupled with the use of 'robust' (see section 6.2) simple low order moment parameters could be used to provide some information about Cherenkov events. This information would be complementary to that obtained from the central high-resolution imaging camera. Another feature of the telescope, which may add to its gamma/hadron discrimination power, is its large mirror area. The Left and Right detectors are identical in design and each view 7m diameter flux collectors. If a measure of an event could be made using the combined signal from both detectors then the number of photons available for analysis would be doubled. Of course the central detector could also be included in such a measure although a calibration would need to be made to account for the different angular resolution and tube responses. The following sections show the results of Monte-Carlo simulations and identify several potentially interesting gamma/hadron discrimination parameters.

7.2 Theoretical distributions of Left Right Parameters

The simulation data used for the work in this chapter was produced using the GENESIS56 code described in section 3.1.1. Primary particles were selected from an energy distribution with integral spectral index 1.6. Gamma rays and hadrons were created with energies > 150 and > 400 GeV respectively. 'Observations' were taken at 0° , 30° and 60° zenith angle. Table 7.1 gives the numbers of events simulated in each data set. A model telescope consisting of three adjacent 7m-diameter mirrors with 70% reflectivity imaged the resulting Cherenkov photons. An ideal detector was modelled at the prime focus of the mirrors with a spatial resolution of 0.01°. Figure 7.1 shows the angular distributions of Cherenkov photons from various primary particles at the image plane of one of the detectors. Note the relative compactness of the gamma ray images and the arcs of Cherenkov photons visible in the higher energy events from muons close to ground level. In these simulations primary hadrons and gamma rays travel parallel to the optic axis of the detector. Random angular offsets can then be added to the hadron initiated Cherenkov images to simulate an isotropic spatial distribution. The

Table 7.1: The numbers of simulated events passing the trigger criteria and used in studies of the Mk6 telescope

Zenith Angle (degrees)	gamma ray Events	Hadron Events
0	2820	1140
30	2910	1300
60	2950	2060

following sections are concerned with the response of the Left and Right detectors to the Cherenkov photons. The field of view of the detectors were approximated in this work as circular with a 1.3° radius. Different telescope models have been applied to the events to simulate the effects of the telescope optics and noise from background starlight photons.

7.2.1 Correlations in Cherenkov Brightness

A Gamma/Hadron discrimination method based on Left/Right correlations in Cherenkov photon brightness is attractive as it would be simple to calculate. By involving only the numbers of photons detected only the zeroth moment, M_o, is needed. Recall that although the lower order moments do not fully exploit the amount of information available they are more robust against the effects of noise (e.g. equation 6.11).

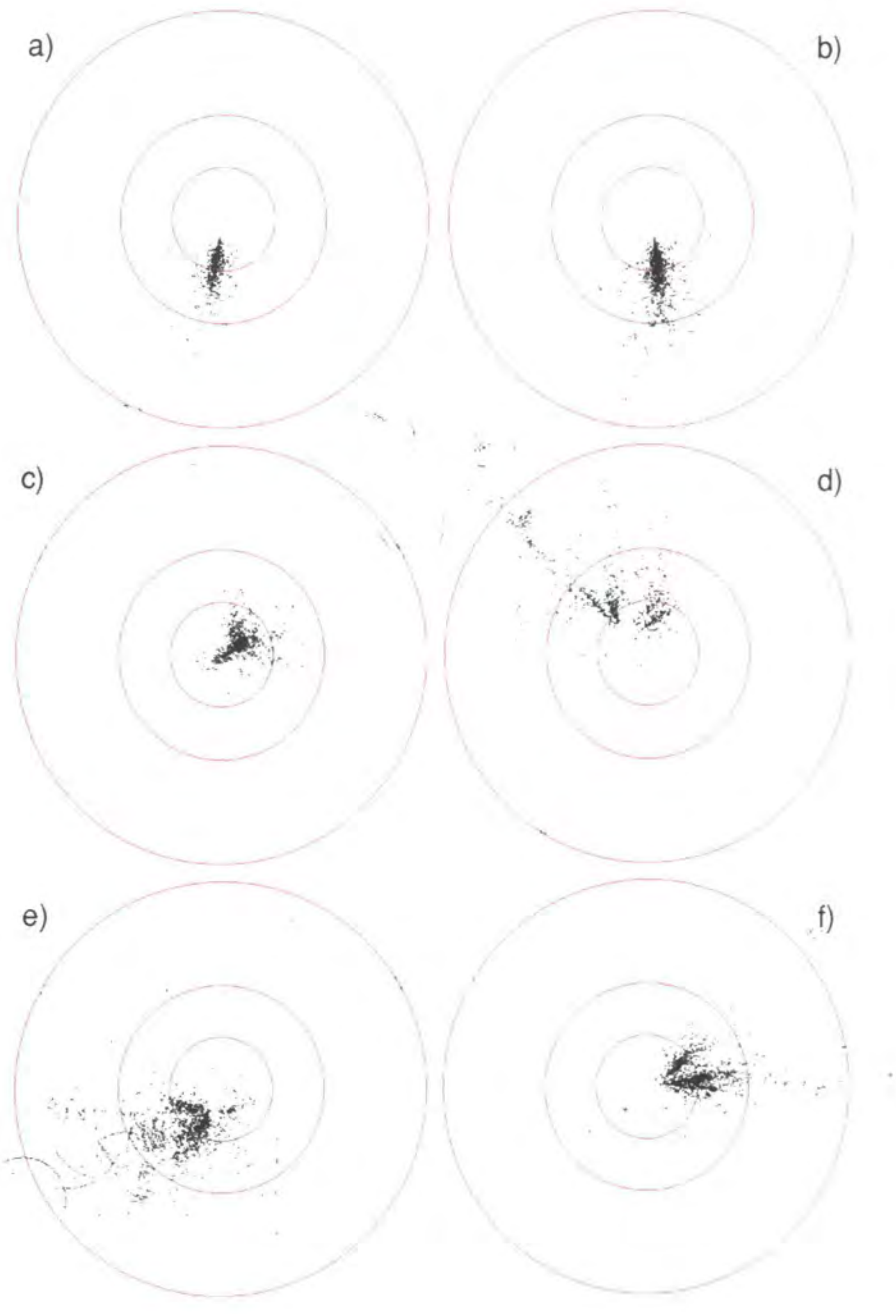

Figure 7.1: Simulated Cherenkov photons imaged by an ideal optical system from vertically falling primary particles; a) a 500 GeV gamma ray, b) a 1TeV gamma ray, c) a 1TeV proton, d) a 1.5TeV proton, e) a 3TeV proton and f) a 3TeV He nucleus. The circles show detector centred fields of view with 1, 2 and 4° radius.

Left/Right Photon Ratio - LRR

The simplest method of measuring photon brightness fluctuation is to record the total amounts of light recorded in each detector per event and find the ratio. The Left/Right photon ratio, *LRR*, is just this although the order of the ratio is adjusted so that $0 < LRR < 1$ is always true. The parameter is comparable to the E_{pRatio} used in studies with the Durham University Mk3/Mk5 stereo pair (see section 4.4.2). The smaller number of penetrating particles within a gamma ray EAS and their greater Cherenkov brightness should lead to a value of *LRR* near 1 for gamma rays and hadrons but with larger variance for hadrons. Figure 7.2 shows the distributions of LRR for simulated gamma rays and hadrons of varying primary energies.

The parameter would not seem to be good at separating gamma rays from hadrons, except at large zenith angles. Accepting events for analysis at 60° zenith angle with $\sim 0.75 < LRR < 1.0$ yields the maximum Q of 1.3 by rejecting ~60% of the hadron events whilst retaining ~85% of the gamma rays. The hadron *LRR* distributions are similar at all zenith angles while the gamma ray distribution is noticeably narrower at larger zenith angles.

Left/Right Photon Fluctuation - LRF

A method of using the size of Cherenkov photon fluctuations to increase the significance of a detection of the Crab Pulsar from the 2σ to 3.2σ level are described by Tümer et. al [152]. The experiment consisted of two 11 m diameter solar energy mirrors separated by 24m. Pairs of PMTs at the focus of each mirror viewed different areas of sky to allow the source and a control field of the sky to

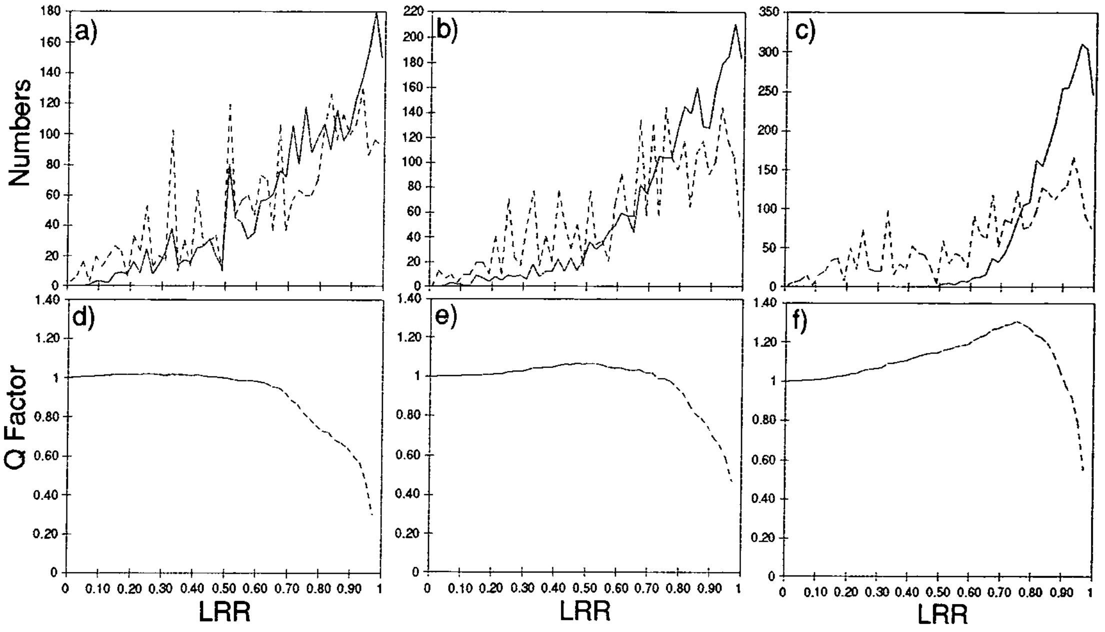

Figure 7.2: The distributions of *LRR* for simulated gamma rays (solid line) and hadrons (dashed line) imaged by an ideal optical system at zenith angles of a) 0° , b) 30° , and c) 60° . Shown in d), e) and f) are the Q factors obtained from the data in a), b) and c) when events with *LRR* less than a particular value are rejected.

be observed simultaneously by each dish. The experiment aimed to use the times of arrivals of Cherenkov events to identify gamma rays arriving periodically at the pulsar period of 33ms. It was found that the normalised pulse height difference, $(PH1 - PH2)/(PH1 + PH2)$ between PMTs viewing the same area of sky in dish 1 and 2, led to a broadly peaked distribution centred at 0 and ranging between ±1. Rejecting events with an absolute difference in this parameter > 0.4 led to the observed signal enhancement.

A similar method is investigated for the Mark 6 telescope; the Left Right

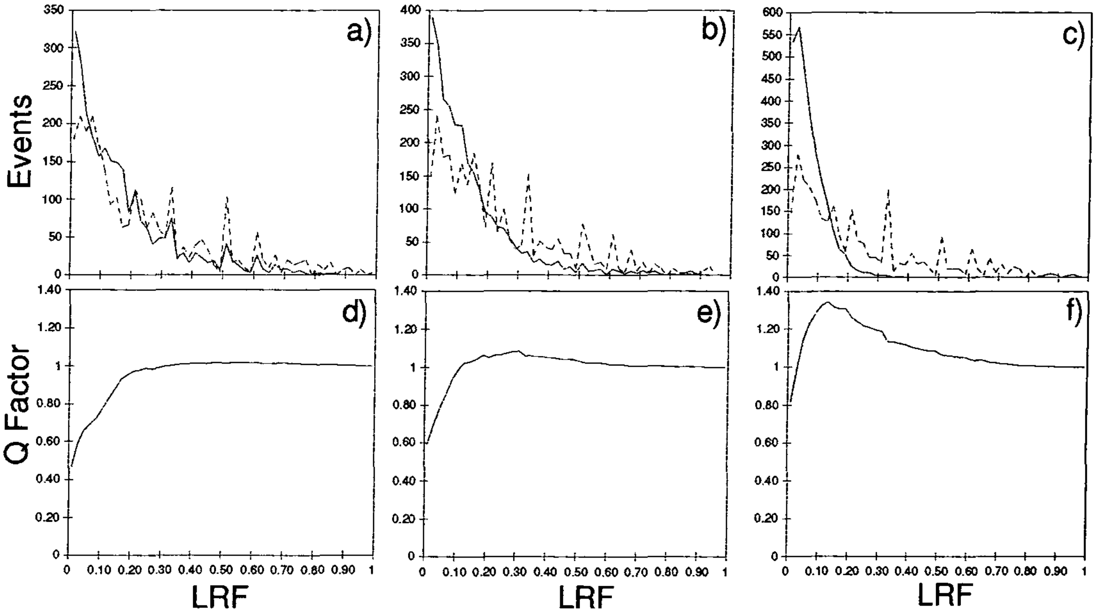

Figure 7.3: The distributions of *LRF* for simulated gamma rays (solid line) and hadrons (dashed line) imaged by an ideal optical system at zenith angles of a) 0° , b) 30° , and c) 60° . Shown in d), e) and f) are the Q factors obtained from the data in a), b) and c) when events with *LRF* greater than a particular value are rejected.

Fluctuation (LRF) parameter is calculated for the total light contained in the Left and Right detectors

$$LRF = \frac{|(\sum P_L - \sum P_R)|}{(\sum P_L + \sum P_R)} \tag{7.1}$$

where $\sum P_X$ is the sum of the number of photons in all the tubes in the Left or Right detectors. The similarity of *LRF* to the measure of Cherenkov photon density fluctuation shown in section 3.6.2 should be noted. The parameter is a different way of describing the same information used to calculate *LRR* and is not independent of it. The distributions of this parameter are shown in figure 7.3. Similarly to LRR, it would seem that any discriminating power obtainable by LRF is a maximum at lower elevations, giving a Q of ~1.3 if data with $LRF > 0.2$ is rejected.

7.2.2 Spatial Correlation of Showers - dDist

The position within a shower where the maximum of Cherenkov photons are emitted is described by the brightest part of a Cherenkov photon image. The centroid position is not necessarily in the same location as the peak brightness position; gamma ray events imaged by a very high-resolution camera would appear tear-shaped for example. Even so the centroid is a good approximation of the image centre and can be fitted reliably. For gamma ray showers the centroid is reasonably well defined and should appear in a similar position within the field of view of two detectors separated by a short distance. The shower maximum position for a hadron initiated event is not as well defined and the larger number of Cherenkov radiating particles reaching ground level can further increase the fluctuation in the determined centroid position of the event.

A Cartesian system of co-ordinates is defined to describe positions on the focal plane of the telescope's detectors from the optic axis in units of degrees. The centroid of an image has the co-ordinates $(\langle x \rangle, \langle y \rangle)$ which are found by calculation of the event's moments, M_1 and M_o, as described in section 6.2. The x axis is defined as the line joining the centres of the Left (L) and Right (R) detectors, with the y axis perpendicular to x and within the focal plane of both detectors. The parameters describing the differences in centroid position in each direction are defined as follows

$$xdDist = \langle x \rangle_R - \langle x \rangle_L \tag{7.2}$$

$$ydDist = \langle y \rangle_R - \langle y \rangle_L \tag{7.3}$$

The distributions of *xdDist* and *ydDist* are quite different due to the different amounts of parallax seen in the x direction, where the detectors are separated by 14m, and the y direction where there is no parallax.

The y direction - *ydDist*

The distributions of *ydDist* for simulated gamma ray and hadron initiated showers at different zenith angles are shown in figure 7.4. Both distributions are centred on the origin and are symmetrical about it. The distribution of *ydDist* is wider for hadron showers because of the greater fluctuations in their longitudinal development and the greater possibility of radiating particles close to the ground offsetting the centroid in one detector.

The x direction - *xdDist*

Simulated distributions of *xdDist* for gamma and hadron showers are shown in figure 7.5.

Unlike *ydDist*, the distributions for *xdDist* are not centred on the origin. The offset of the peak in the distributions is explained in figure 7.6. If a shower is viewed by two detectors separated by x it will be detected as long as the position of the shower maximum is within the field of view of both detectors. Because

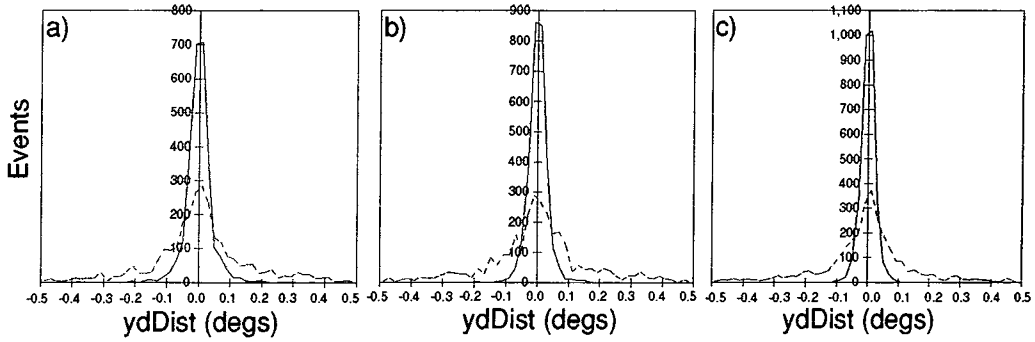

Figure 7.4: The distributions of *ydDist* for simulated gamma rays (solid line) and hadrons (dashed line) imaged by an ideal optical system at zenith angles of a) 0° , b) 30° , and c) 60° .

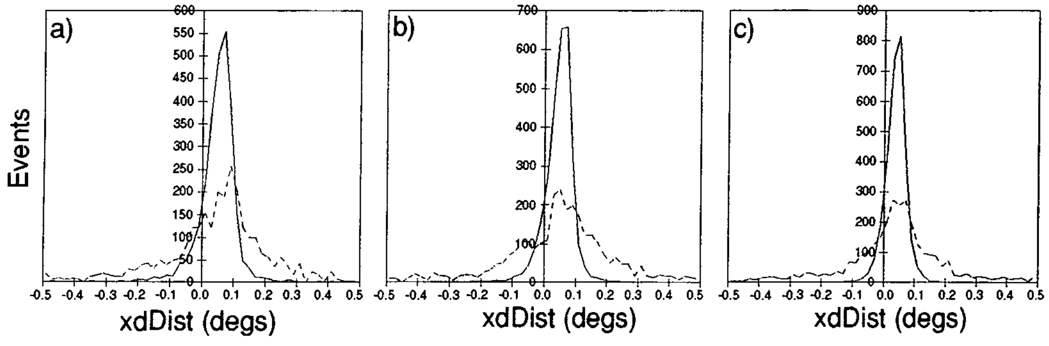

Figure 7.5: The distributions of *xdDist* for simulated gamma rays (solid line) and hadrons (dashed line) at zenith angles of a) 0° , b) 30° , and c) 60° .

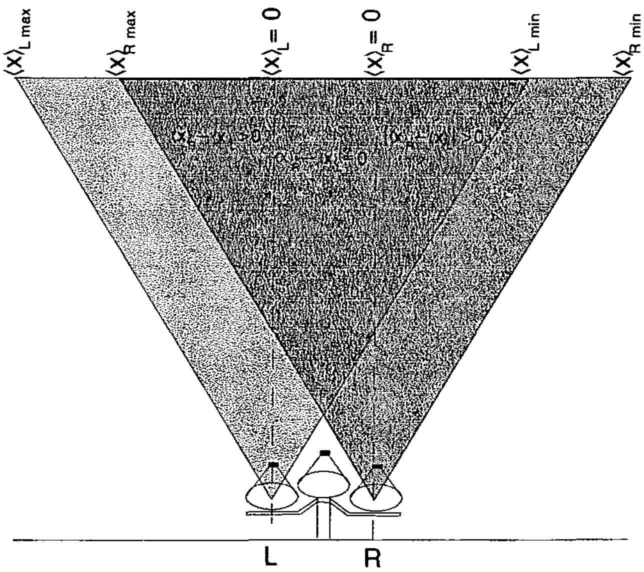

Figure 7.6: The offset in the peak of the *xdDist* distribution. The telescope will only observe Cherenkov events if they are observed where the fields of view of both detectors overlap (the darkest shaded area). The observed values of *xdDist* should always be ≥ 0 due to the separation of the dishes and the definitions of the $< x >$ origin in each dishes.

the detectors are separated and the angular position in each dish is defined with respect to the centre of that dish, an asymmetry is introduced in that;

$$|\langle x \rangle_{R\ max}| > |\langle x \rangle_{R\ min}| \tag{7.4}$$

and

$$|\langle x \rangle_{L\ max}| < |\langle x \rangle_{L\ min}| \,. \tag{7.5}$$

This effect leads to the observed offset of the peak of the *xdDist* distribution from the origin. In reality a spread in the distribution occurs because the exact same part of the shower will not be identified as the centroid in each detector due to noise fluctuations which also accounts for the spread in *ydDist*.

The angle *xdDist* can be used to give an approximate measure of the height of maximum; $h \approx x \tan(xdDist)$ where $x = 14$m. Taking the value of the peak of the gamma ray *xdDist* distribution, 0.07° , a height of maximum of 11km is found at 0° zenith angle. This is a somewhat arbitrary value in this case since a spectrum of events is being considered and the different energies within the data set will maximise at different heights. Figure 7.7 shows the height of maximum distribution for the events calculated within the air shower simulation programme. The uncertainty in calculating height of maximum using *dDist* based on only a 14m separation is large. The position of the peak of the *xdDist* distribution can be seen to move closer to the origin at larger zenith angles. This is because the density of the atmosphere scales as $\sec\theta$ and the height of maximum of the showers occurs further away from the observer at low elevation. A typical gamma ray shower may maximise after traversing 300g/cm^2 of atmosphere, a vertical height of 9km when the zenith angle is 0° . At 60° zenith the same shower will maximise at a vertical altitude of 13.5km, a distance away from the observer of 27km.

The gamma ray *xdDist* distributions are also noticeably skewed, especially at smaller zenith angle. The numbers of Cherenkov photons emitted by electrons in the shower rises steadily with depth until shower maximum when the average electron energy is ~80MeV. At this energy ionisation of the atmosphere by the electrons reduces their energy below the Cherenkov threshold energy (21MeV). This occurs soon after shower maximum and the Cherenkov emission ceases. The steep drop at large positive *xdDist* (low altitude) of the gamma ray distri-

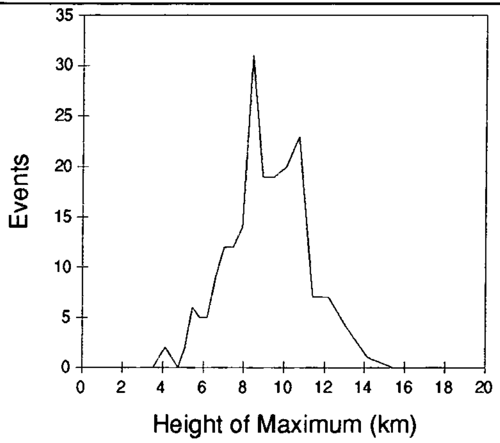

Figure 7.7: The height of maximum distribution for a spectrum of gamma rays at 0° zenith angle.

bution reflects the swift reduction in Cherenkov emitting particles after shower maximum. The hadron *xdDist* distributions do not exhibit the same asymmetry. The numbers of individual electromagnetic showers which make up a hadron EAS mean that their particle production rate does not rise and fall as smoothly as it does for gamma ray EAS and so their *xdDist* distributions are not as skewed. At large zenith angles the skewness in the *xdDist* distributions is less pronounced as the showers develop high up in the atmosphere where the atmosphere is more rarefied. Here the electrons reach the critical energy at a greater range of heights than they do at the zenith and the showers die out more slowly.

7.2.3 Combining xdDist and ydDist into dDist

The centroid of a Cherenkov image of a hadronic EAS is not as accurate an estimate of the height of maximum of the EAS as it would be for gamma rays originating from a point source. This is because the primary particles can originate from any position on the sky, travel non-axially to the telescope and exhibit

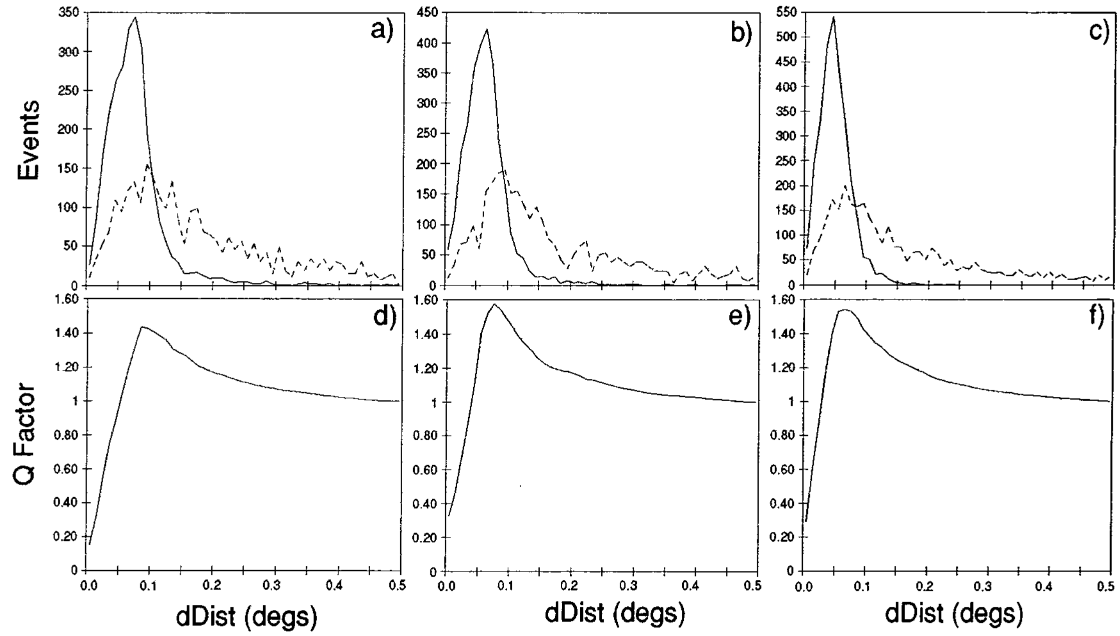

Figure 7.8: The distributions of *dDist* for simulated gamma rays (solid line) and hadrons (dashed line) imaged by an ideal optical system at zenith angles of a) 0° , b) 30° , and c) 60° . Shown in d), e) and f) are the Q factors obtained from the data in a), b) and c) when events with *dDist* greater than a particular value are rejected.

large fluctuations in their Cherenkov density. It is less likely for a hadron initiated event to have simultaneously small values of $xdDist$ and $ydDist$ than it is for an event caused by a high-energy photon. *dDist* (figure 7.8) is the angular separation of the two images and can be obtained by taking the vector sum of $xdDist$ and $ydDist$.

$$dDist = \sqrt{xdDist^2 + ydDist^2}. \tag{7.6}$$

This is a comparable parameter to D_{miss}, which was discussed in section 4.4.2

and used in the Durham observations of AEAquarii [36], and *DRO*, introduced by researchers at the Crimean Astrophysical Observatory [96].

These simulations show that *dDist* would seem to be a potentially good gamma/hadron discriminating parameter, especially at larger zenith angles. It is least effective at the zenith although an analysis cut at $dDist = 0.1°$ is still effective and retains ~2/3 of the gamma rays and $< 50\%$ of the hadrons.

7.3 The Effect of Pixellation on the Theoretical Distributions of Left/Right Parameters

The Left and Right detectors on the Mk6 telescope consist of tessellated hexagonal PMTs viewing 0.5° of sky across their flat-sided diameters. Model detectors consisting of 19×0.5° diameter circular PMTs arranged in a close packed hexagonal array have been applied to the simulated events of the previous section. A highly simplified trigger criterion has been applied requiring at least one photon to be registered in a spatially corresponding pair of PMTs in the Left and Right detectors before an 'event' is recorded. The Left/Right parameter distributions have then been recalculated. The pixellation of the detectors also makes it possible to introduce other parameters to the investigation.

7.3.1 Structural Correlation Parameter - χ^2

The structure of Cherenkov photon distributions within an event could be exploited as a gamma/hadron discriminator. It is expected that the images of a Cherenkov event recorded in the Left and Right detectors should be less well cor-

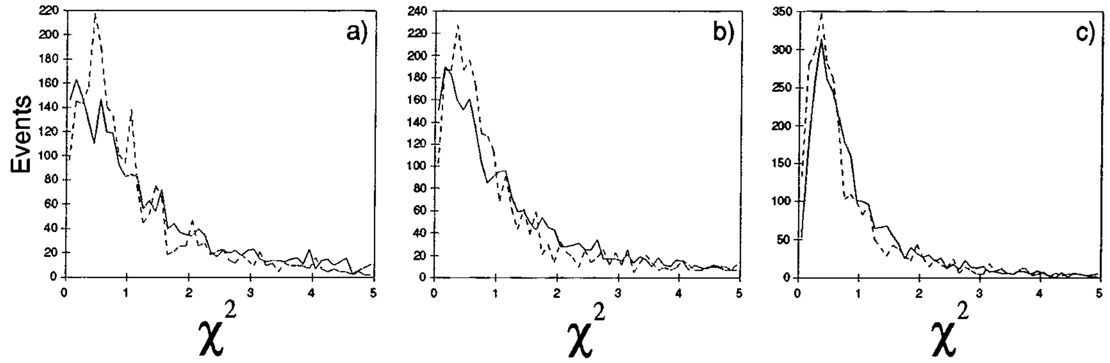

Figure 7.9: The distributions of χ^2 for simulated gamma rays (solid line) and hadrons (dashed line) at zenith angles of a) 0° , b) 30° , and c) 60° .

related for hadrons than for gamma rays. To quantify this correlation a statistical reduced χ^2 test has been adapted which uses the fluctuation in the signals L_i, R_i in N pairs of PMTs. The χ^2 test for data points x_i is defined as

$$\chi^2 = \frac{1}{N}\sum_{i=1}^{N}\frac{(x_i - f)^2}{\sigma_i^2}, \tag{7.7}$$

where f is some function describing an 'ideal' value of x_i and σ_i is the error on x_i. If we compare L_i against R_i and the total signals in the Left and Right dishes are similar then Poisson statistics apply and σ_i becomes $\sqrt{R_i}$. Hence the experimental gamma/hadron discrimination parameter, χ^2 , is defined

$$\chi^2 = \frac{1}{4N}\sum_{i=1}^{N}\frac{(L_i - R_i)^2}{R_i} \quad R_i \neq 0 \ . \tag{7.8}$$

Figure 7.9 shows the distributions for energy spectra of gamma ray and hadron events at various zenith angles. There is essentially no difference between the gamma ray and hadron χ^2 distributions. The parameter may fail as a gamma/hadron discriminator because the 0.5° pixel size masks structure within an image. There is no positional information used in the parameter and so its angular resolving power is limited to the pixel size. As a comparison, the moments method used to calculate *dDist* uses many signals at various points in the focal plane of the detector allowing fluctuations on a small scale to be measured. The χ^2 parameter, as defined here will not be considered further. A way forward may be to involve positional information in the parameter. At present two wildly varying PMTs on opposite sides of the detectors will give the same value of χ^2 as adjacent PMTs. Gamma/hadron discriminating power could be obtained by taking into account the correlation of signals, perhaps by fitting an ideal function to the images in the Left and Right detector [90].

7.3.2 Concentration Parameter - LRconc

The density of Cherenkov photons from a gamma ray EAS should be higher than that from hadrons of the same energy (section 3.6.1). Gamma ray EAS have a high Cherenkov yield which comes from a compact emission region and radiating particles within the shower travel very nearly along the primary photon trajectory. Hadron EAS contain particles travelling at comparatively large angles and on average yield a lower number of photons from a wider emission region than in a gamma ray EAS. For the purposes of these investigations the concentration parameter, *LRconc*, has been defined as

$$LRconc = \frac{\sum P}{8 \sum N}. \tag{7.9}$$

$\sum P$ is the total of Cherenkov photons detected in $\sum N$ PMTs in the Left and Right detectors. The parameter does not rely so much on making measurements

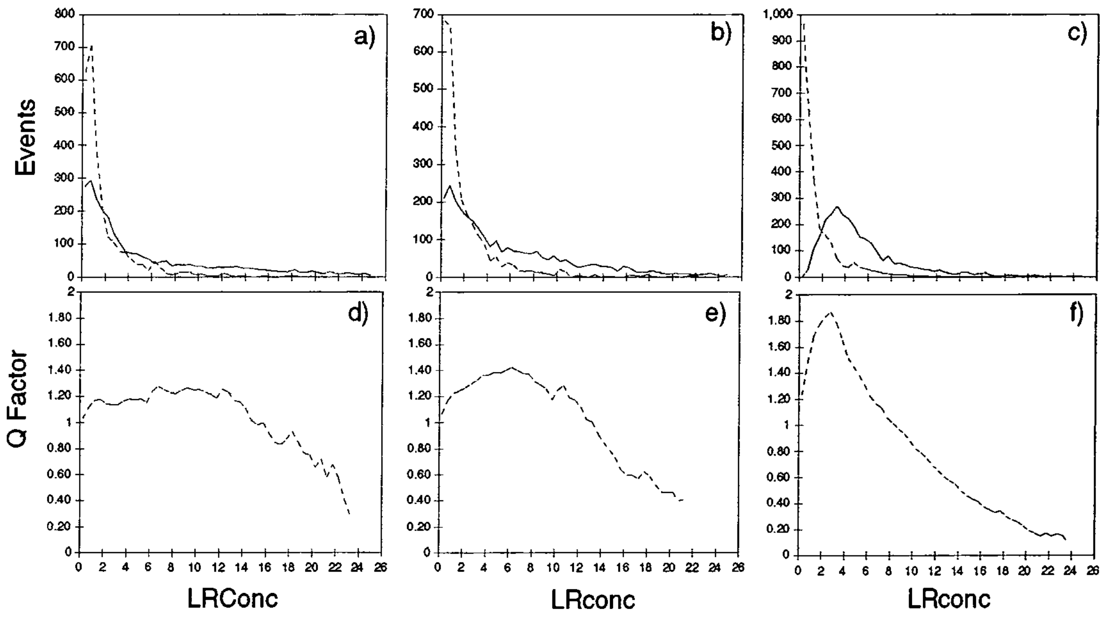

Figure 7.10: The distributions of *LRconc* for simulated gamma rays (solid line) and hadrons (dashed line) imaged by a pixellated optical system at zenith angles of a) 0° , b) 30° , and c) 60° . Shown in d), e) and f) are the Q factors obtained from the data in a), b) and c) when events with *LRconc* less than a particular value are rejected.

of fluctuations or differences measured over the 14m baseline as do the other parameters discussed previously. Instead the large combined area of the Left and Right detectors is used to collect large numbers of Cherenkov photons. The two 7m mirrors combined have approximately the same area as a single 10m mirror. The parameter could be considered as a variant on the 'Concentration' parameters used by the Durham and other groups [63].

The distributions of the parameter for gamma rays and hadrons and the accompanying values of Q for potential analysis cuts are shown in figure 7.10. There are large differences between the gamma ray and hadron distributions, especially at larger zenith angles. Rejecting events with $LRconc < 3$ when the zenith angle $= 60°$ yields $Q \approx 1.8$. Gamma rays have larger values of *LRconc* on average. This is as expected since gamma ray Cherenkov events are brighter and come from a more compact emission region than hadron initiated events. The mean value of *LRconc* for gamma rays increases with zenith angle. At large zenith angles gamma ray showers maximise at larger distances from the detector and have smaller images. The absorption of photons in the atmosphere increases with distance and reduces the Cherenkov brightness, however this is a smaller effect than the reduction in image size. The values of *LRconc* for hadron EAS are smaller reflecting their larger size and reduced brightness over gamma ray EAS.

7.3.3 LRR, LRF and dDist Distributions in Pixellated Detectors

Figures 7.11 - 7.13 show the effect of applying a model imaging system comprising $19 \times 0.5°$ PMTs, close packed in a hexagonal array, to the data from the previous section.

The effectiveness of *LRR* and *LRF* as gamma/hadron discriminators has been slightly reduced from the ideal case. Although the parameters require no spatial information a reduction should be expected as some detection area has been lost by using a hexagonal array of circular elements. The difference in area between a circular and hexagonal field of view with radius or half vertex to vertex length of 1.3° is $\sim$30%, including the gaps between the 19 circular close packed pixels.

Now let us consider *dDist*. Because the resolution of the detectors has been

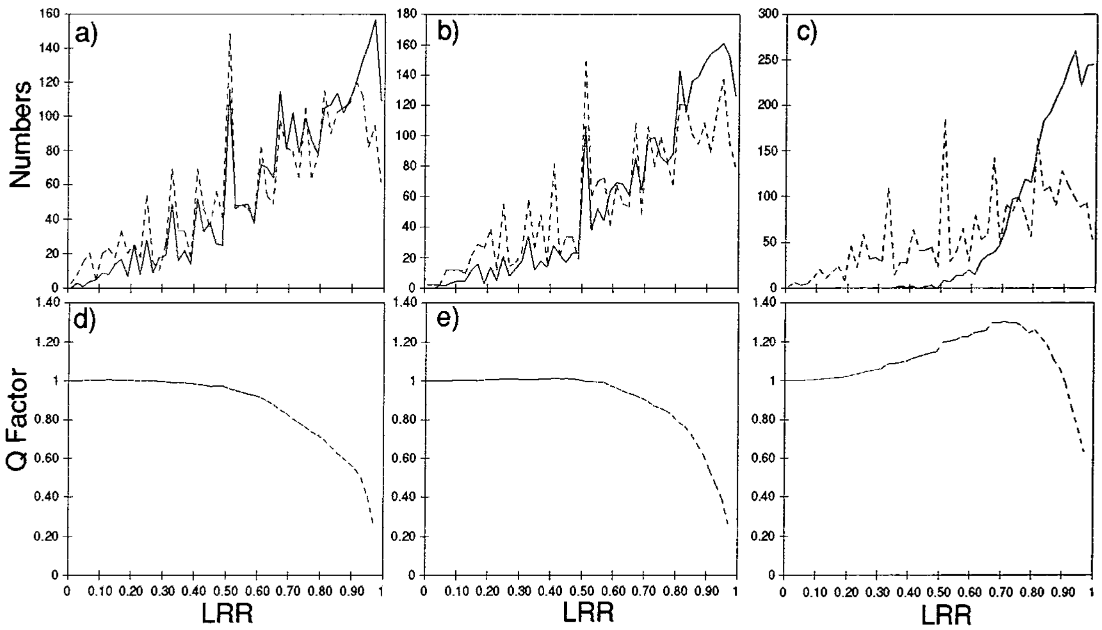

Figure 7.11: The distributions of *LRR* for simulated gamma rays (solid line) and hadrons (dashed line) imaged by a pixellated optical system at zenith angles of a) 0° , b) 30° , and c) 60° . Shown in d), e) and f) are the Q factors obtained from the data in a), b) and c) when events with *LRR* less than a particular value are rejected.

decreased from 0.01-0.5° it is harder to see differences between the centroid positions in the two detectors. The gamma ray and hadron distributions in 7.13 also appear more peaked at $dDist = 0$ than in the ideal case in figure 7.8. This is because small events occupying a single corresponding PMT in the Left and Right detectors have $dDist = 0$. Even so there are still noticeable differences between the distributions and the Q factors for $dDist$ ranges from $1.2 - 1.3$ over the range of zenith angles considered.

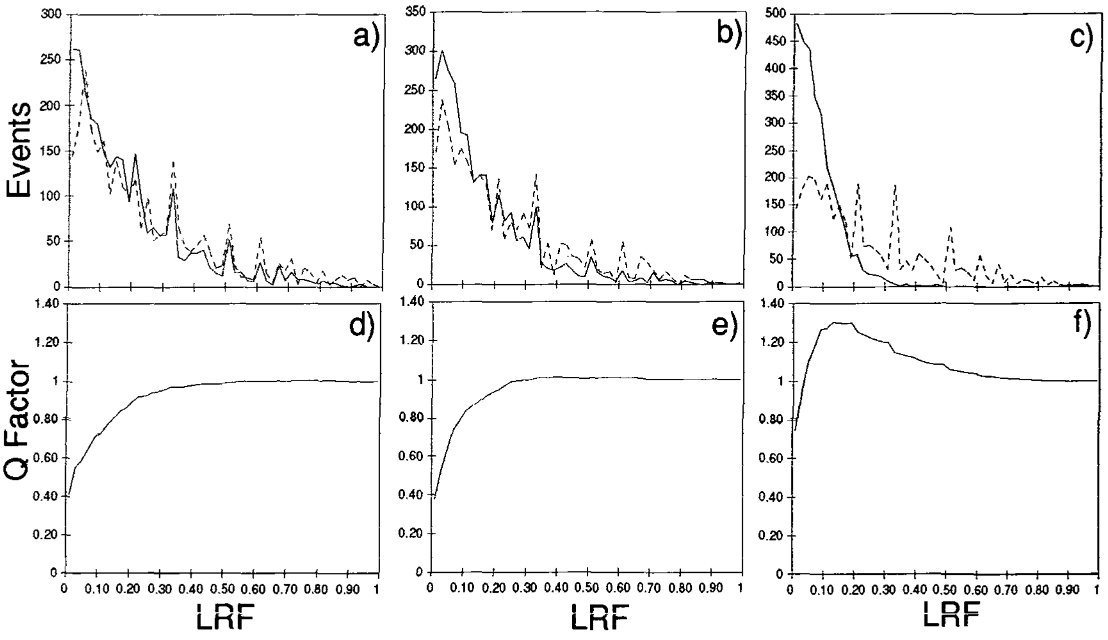

Figure 7.12: The distributions of *LRF* for simulated gamma rays (solid line) and hadrons (dashed line) imaged by a pixellated optical system at zenith angles of a) 0° , b) 30° , and c) 60° . Shown in d), e) and f) are the Q factors obtained from the data in a), b) and c) when events with *LRF* greater than a particular value are rejected.

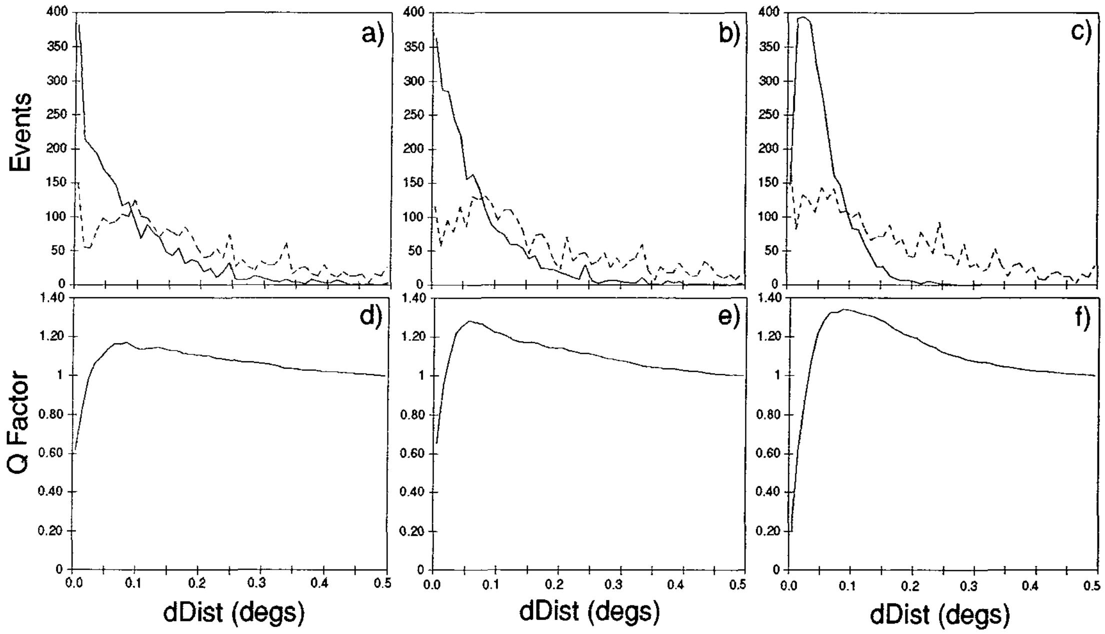

Figure 7.13: The distributions of *dDist* for simulated gamma rays (solid line) and hadrons (dashed line) imaged by a pixellated optical system at zenith angles of a) 0° , b) 30° , and c) 60° . Shown in d), e) and f) are the Q factors obtained from the data in a), b) and c) when events with *dDist* greater than a particular value are rejected.

7.4 The Effect of the Telescope Optics

The optical performance of the Aluminium mirror segments of the Mk6 telescope was discussed in section 5.1.2. Random numbers drawn from a two component gaussian distribution which describes the measured PSF of the central dish have been added to each of the simulated photons before being presented to the model pixellated detector packages. Again one would not expect this to greatly affect the non-spatially (M_o) dependent LRR and LRF distributions. However, similarly to when pixellation was applied, there will be a loss of detected light as photons from events near the edge of the detector are spread outside the detector. The distributions of LRR and LRF are shown in figures 7.14 and 7.15.

Since the size (standard deviation) of the PSF is comparable to the PMT radius *dDist* and *LRconc* remain effective gamma-hadron discriminators (figures 7.16 and 7.17). The peaks of the *dDist* distributions have moved away from the value of $dDist = 0$ seen in figure 7.13 as the spreading of the photons by the PSF makes it unlikely that all but the smallest events are completely contained within a single PMT. There is some evidence for a slight improvement in the Q factors obtained for *LRconc* with an optical PSF applied. This is because *LRconc* is more sensitive to spatial fluctuations than *dDist* since it is a function of number of PMTs hit by photons. If one photon moves to a previously empty PMT when optical spreading is applied it can affect the number of PMTs used in the calculation of *LRconc* by a reasonably large fraction. Since the Cherenkov images of hadron EAS are more spread out than gamma ray images it is more likely that optical spreading of photon positions will reduce *LRconc* for hadrons than gamma rays. As a general summary it would appear that the optical spreading of

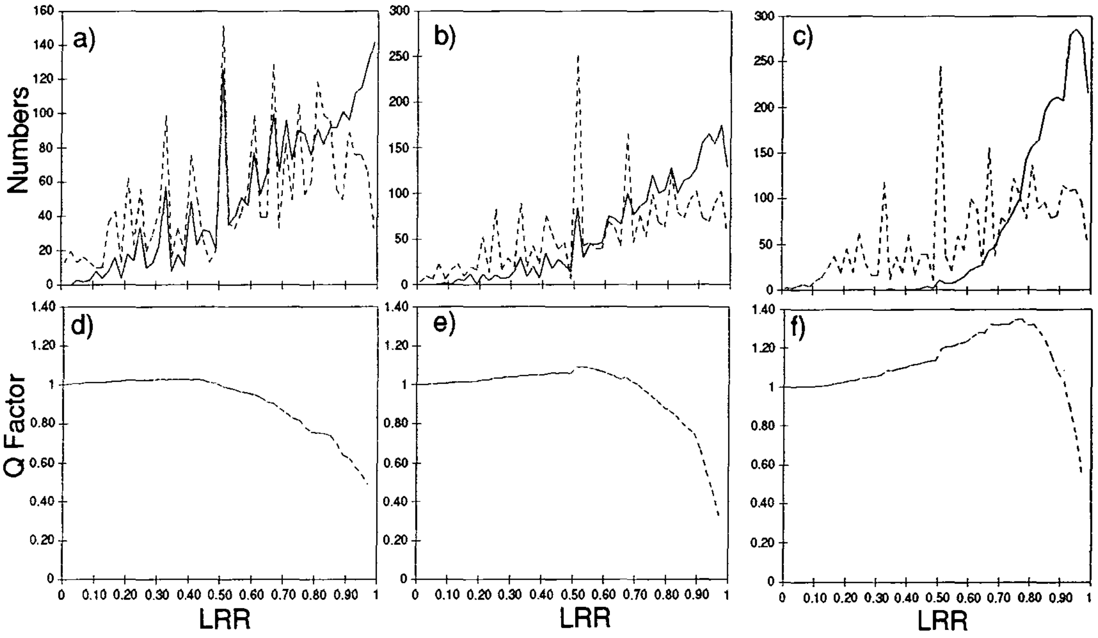

Figure 7.14: The distributions of *LRR* for simulated gamma rays (solid line) and hadrons (dashed line) imaged by a pixellated optical system with a point spread function of 0.39° width. Shown are events observed at zenith angles of a) 0° , b) 30° , and c) 60° . Shown in d), e) and f) are the Q factors obtained from the data in a), b) and c) when events with *LRR* less than a particular value are rejected.

photons is not large enough to overcome the 0.5° pixel size of the detectors. It is the detector resolution which is the limiting factor here in the effectiveness of the Left/Right parameters as gamma/hadron discriminators and not the telescope PSF.

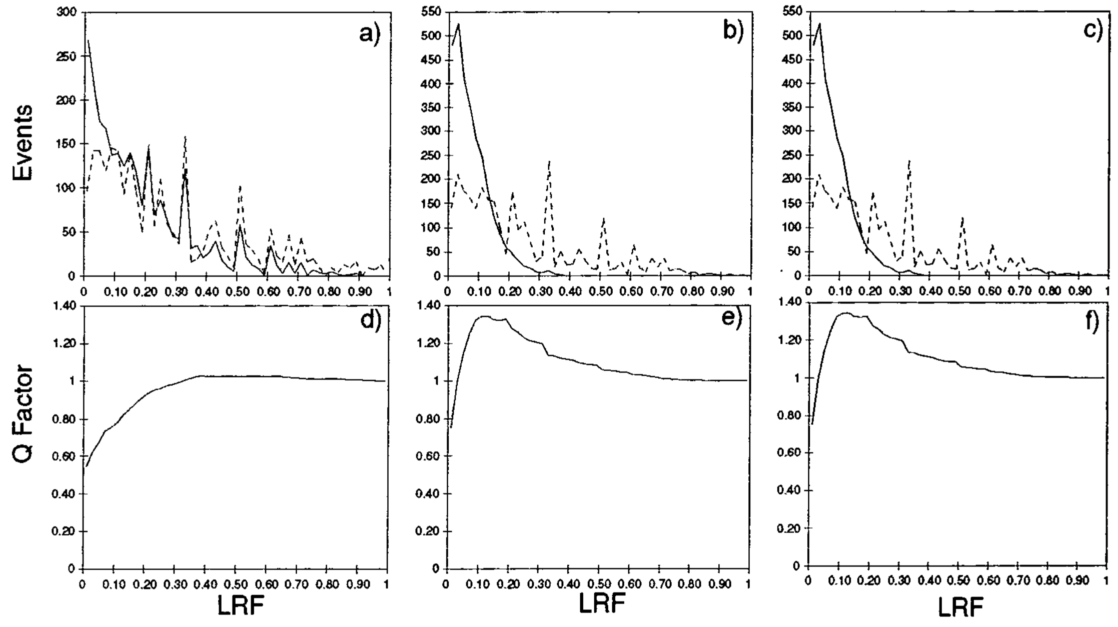

Figure 7.15: The distributions of *LRF* for simulated gamma rays (solid line) and hadrons (dashed line) imaged by a pixellated optical system with a point spread function of 0.39° width. Shown are events observed at zenith angles of a) 0° , b) 30° , and c) 60° . Shown in d), e) and f) are the Q factors obtained from the data in a), b) and c) when events with *LRF* greater than a particular value are rejected.

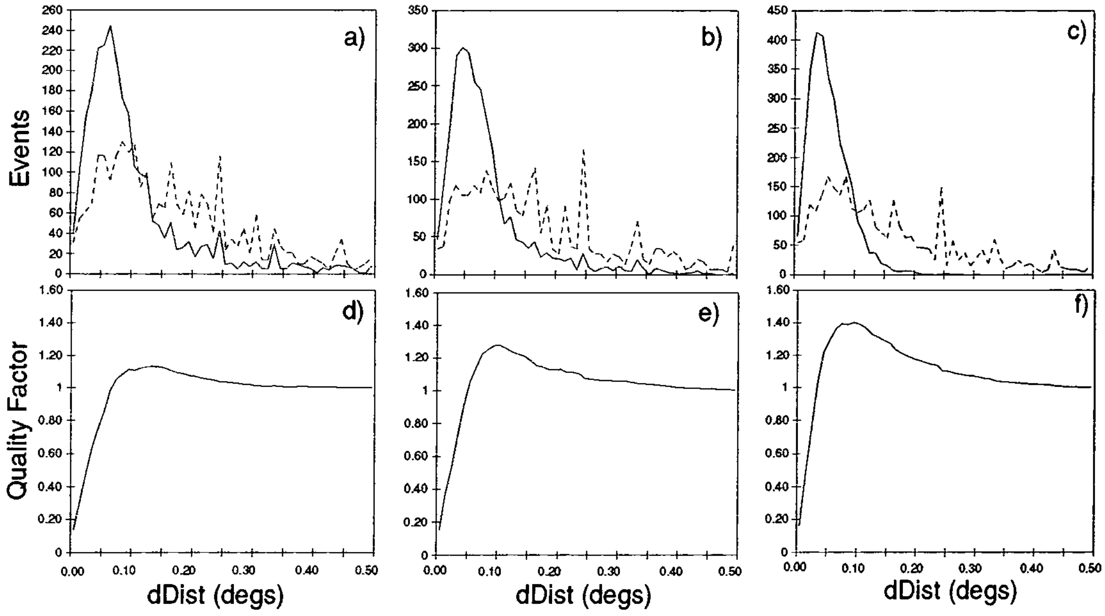

Figure 7.16: The distributions of *dDist* for simulated gamma rays (solid line) and hadrons (dashed line) imaged by a pixellated optical system with a point spread function of 0.39° width. Shown are events observed at zenith angles of a) 0° , b) 30° , and c) 60° . Shown in d), e) and f) are the Q factors obtained from the data in a), b) and c) when events with *dDist* greater than a particular value are rejected.

7.5 The Effect of PMT Noise on the Left/Right Parameters

Noise can be added to the simulations based on estimates of the numbers of background starlight photons that would be detected by the telescope (recall equations 4.2 and 4.3). The mean variation in background photon flux is estimated as ~12 photons/PMT/gate time for a Left/Right PMT in the Mk6 telescope. This value,

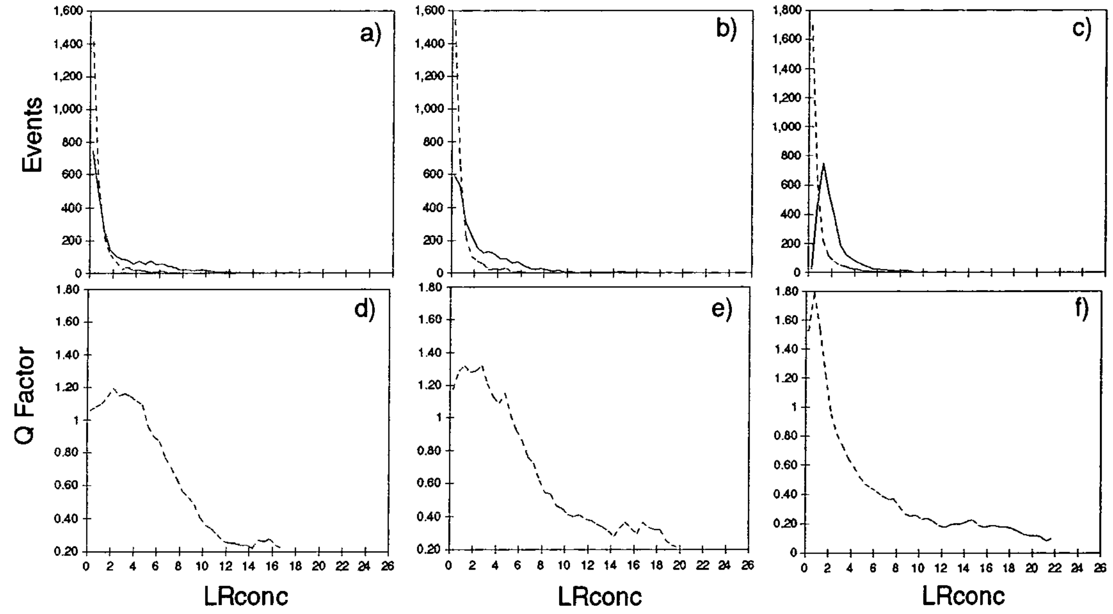

Figure 7.17: The distributions of *LRconc* for simulated gamma rays (solid line) and hadrons (dashed line) imaged by a pixellated optical system with a point spread function of 0.39° width. Shown are events observed at zenith angles of a) 0° , b) 30° , and c) 60° . Shown in d), e) and f) are the Q factors obtained from the data in a), b) and c) when events with *LRconc* less than a particular value are rejected.

which is not at odds with observations made with the Mk6 telescope, has been used as the width of a gaussian distribution from which random numbers were drawn and added to each PMT in the images. A gaussian distribution with a mean of zero is a good approximation to a poissonian distribution with a mean equal to the background flux. The moments are calculated simply since by adding random gaussian fluctuations to the images the PMT signals are effectively pedestal corrected. Shown in figures 7.18-7.21 are the distributions of the Left/Right

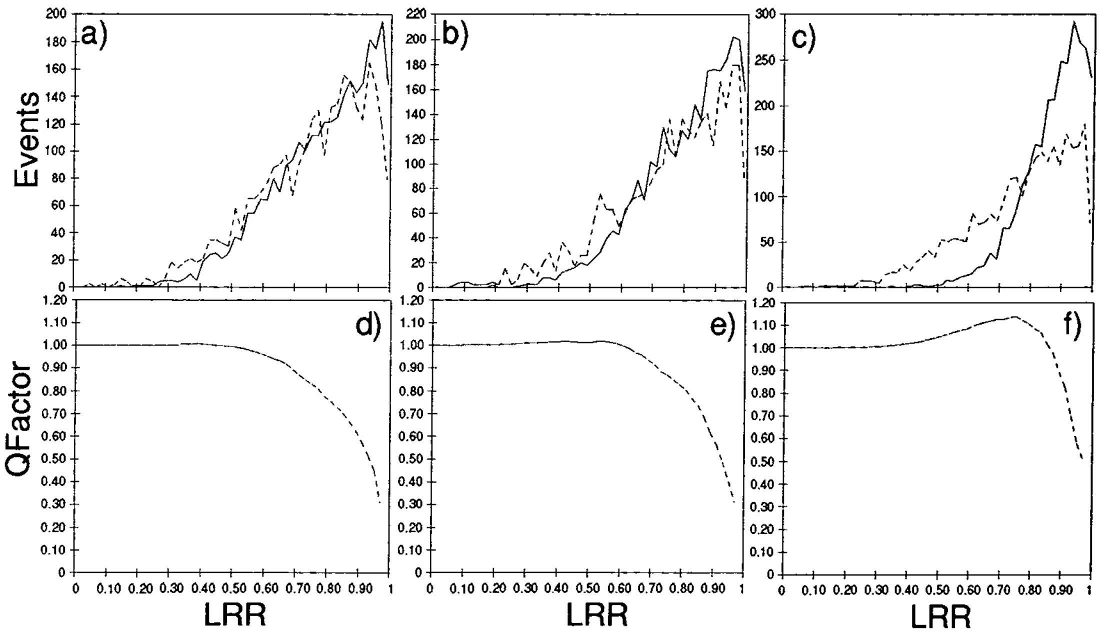

Figure 7.18: The distributions of *LRR* for simulated gamma rays (solid line) and hadrons (dashed line) imaged by a pixellated optical system against a random background flux of starlight photons. Shown are events observed at zenith angles of a) 0° , b) 30° , and c) 60° . Shown in d), e) and f) are the Q factors obtained from the data in a), b) and c) when events with *LRR* less than a particular value are rejected.

parameters with sky noise added.

Adding noise to the distributions of all of the Left/Right parameters severely reduces their effectiveness as gamma/hadron discriminators. Only at low elevations, where fluctuations in the parameters for gamma rays are minimised, do any of the parameters retain any effectiveness. When measuring fluctuations in Cherenkov events it is hardly surprising that adding another source of random fluctuations makes this measurement more difficult. If these simulations accur-

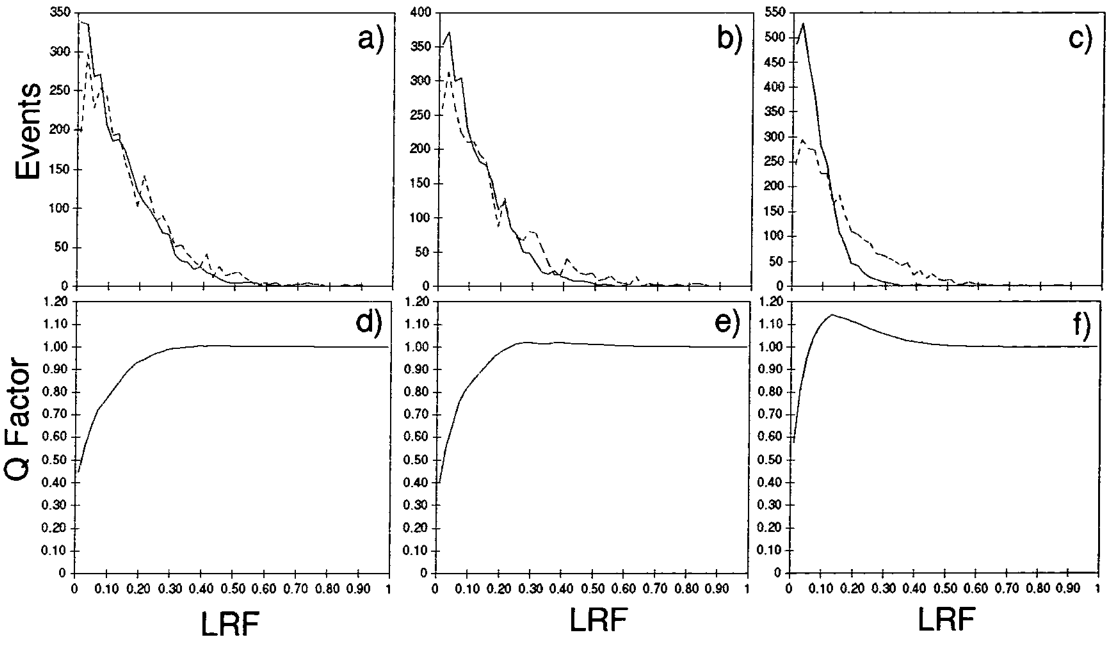

Figure 7.19: The distributions of *LRF* for simulated gamma rays (solid line) and hadrons (dashed line) imaged by a pixellated optical system against a random background flux of starlight photons. Shown are events observed at zenith angles of a) 0° , b) 30° , and c) 60° . Shown in d), e) and f) are the Q factors obtained from the data in a), b) and c) when events with *LRF* greater than a particular value are rejected.

ately reflect what actually occurs in the Mk6 telescope, then noise would be a serious problem to overcome. Consequences may be that the Left/Right parameters may only be useful when observing 'low noise' fields, away from the galactic plane and/or for the brightest events with maximum signal to noise ratio. In reality the PMT noise in the telescope is the combination of many individual sources of noise and not a simple gaussian. Further simulations taking account of this would be necessary to proceed further. However it may be possible to reduce

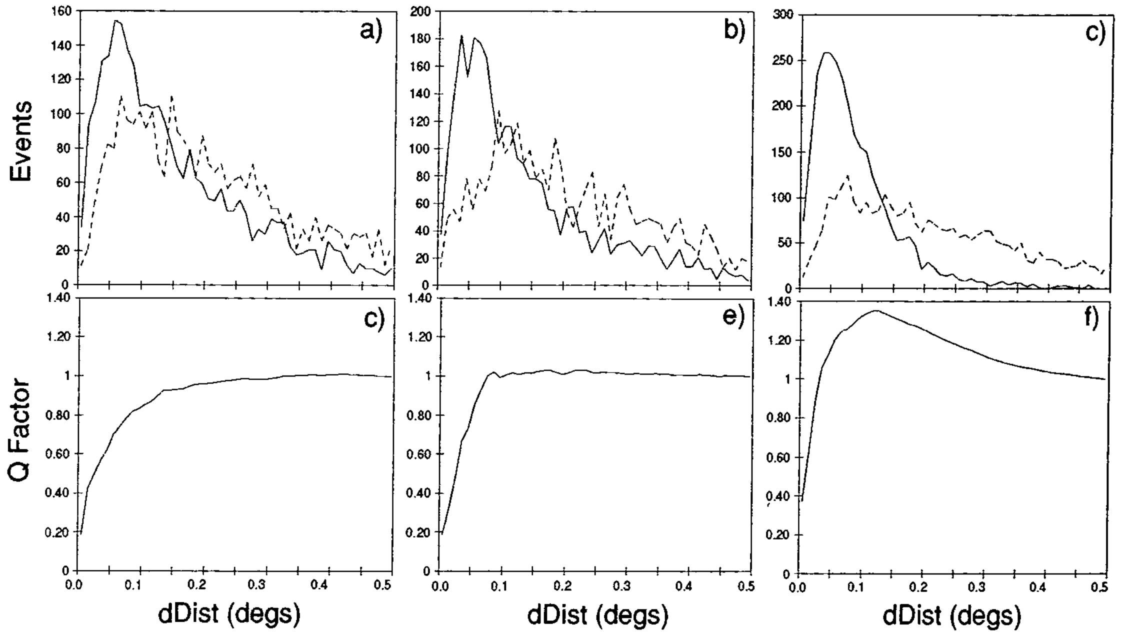

Figure 7.20: The distributions of *dDist* for simulated gamma rays (solid line) and hadrons (dashed line) imaged by a pixellated optical system against a random background flux of starlight photons. Shown are events observed at zenith angles of a) 0° , b) 30° , and c) 60° . Shown in d), e) and f) are the Q factors obtained from the data in a), b) and c) when events with *dDist* greater than a particular value are rejected.

the effects of noise for all events by selecting which signals to use in calculating the parameters on the basis of individual PMT signal to noise ratio.

7.5.1 Applying an Analysis Threshold

An attempt to counteract the effects of noise can be made by applying a selection threshold to the PMT signals. Figure 7.22 shows the Q factors obtained for the discussed Left/Right parameters, at 60° zenith angle, when only PMTs with

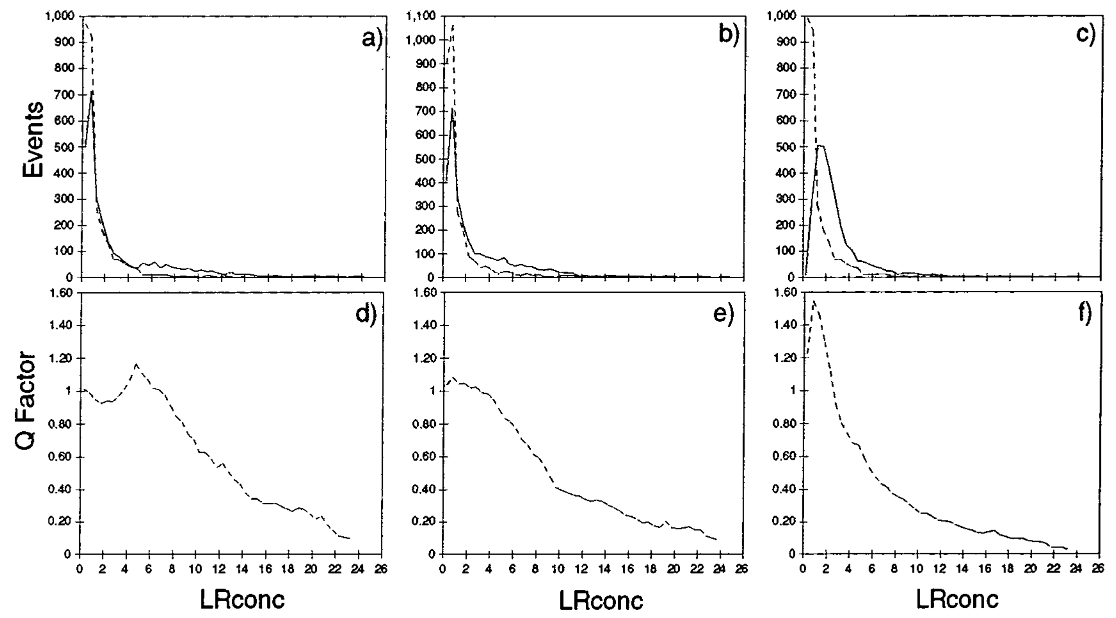

Figure 7.21: The distributions of *LRconc* for simulated gamma rays (solid line) and hadrons (dashed line) imaged by a pixellated optical system against a random background flux of starlight photons. Shown are events observed at zenith angles of a) 0° , b) 30° , and c) 60° . Shown in d), e) and f) are the Q factors obtained from the data in a), b) and c) when events with *LRconc* less than a particular value are rejected.

signals above a certain value have been included in the parameter calculations.

Applying an analysis threshold to the data does not affect the Q factors for *LRR*. This is understandable since the quantity is merely a ratio of photon numbers and since a symmetrical noise function is being added to the data the effect on *LRR* cancels out on average. The other parameters all show some improvement when a 6 photon threshold (50% of the noise function width) is applied to the data. It is supposed that making this selection identifies a reasonable fraction

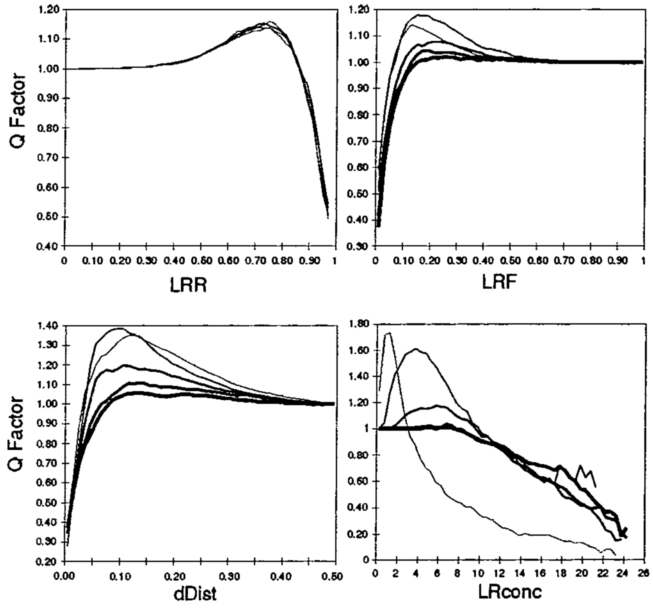

Figure 7.22: The effect of applying an analysis threshold on the Q factors of the Left/Right parameters when Cherenkov events, seen at 60° zenith angle, are superimposed on a background starlight flux (random gaussian with rms = 12photons)and imaged by pixellated detectors. The lines indicate analysis thresholds of 0 (thinnest), 6, 12, 24 and 30 photons (thickest).

of the genuine Cherenkov light and reduces the effects of noise. Above this selection threshold the Q factors for parameters reduce again. Too high a threshold starts to eat into the Cherenkov component of the image which increases the measurement errors on the parameters. Nevertheless this method may be used to slightly improve the effectiveness of *dDist*, *LRF* and *LRconc* as gamma/hadron discriminants after a more careful simulation of the telescope is performed.

7.6 The Effect of Image Brightness on the Left/Right Parameters

The measurable quantity in a Cherenkov image which relates to the gamma ray primary energy is the brightness of the image. The yield of Cherenkov photons from various primary energy radiation was shown in 3.6.1. If the measures of fluctuation or concentration are functions of primary energy then this may need to be considered in any analysis method based on them. Scatter plots of all the parameters described in this chapter against the number of Cherenkov photons, N_L, detected in the left dish are shown in figure 7.23. 1000 simulated events from showers incident at a zenith angle of 30° have been considered in each plot.

The parameters, LRR and LRF, are 'photon count based' — that is that they depend only on numbers of detected photons (M_o) and no spatial information. The scatter plots of LRR and LRF against N_L appear roughly as reflections of each other in the N_L axis for both gamma rays and hadrons. Scatter in the distributions is largest for dimmer events and there would appear to be some clustering of the events at both large LRR and small LRF for the brighter gamma ray initiated events. We would perhaps see the most effective gamma/hadron discrimination when the brighter Cherenkov images are considered. Even so, on their own neither of the photon count based parameters would appear to be very highly effective gamma/hadron discriminators.

There is larger scatter in the value of *dDist*, similarly to the photon based parameters, for the dimmest events. This is true for both the gamma ray and hadron initiated events although the scale of the spread is larger for the hadron

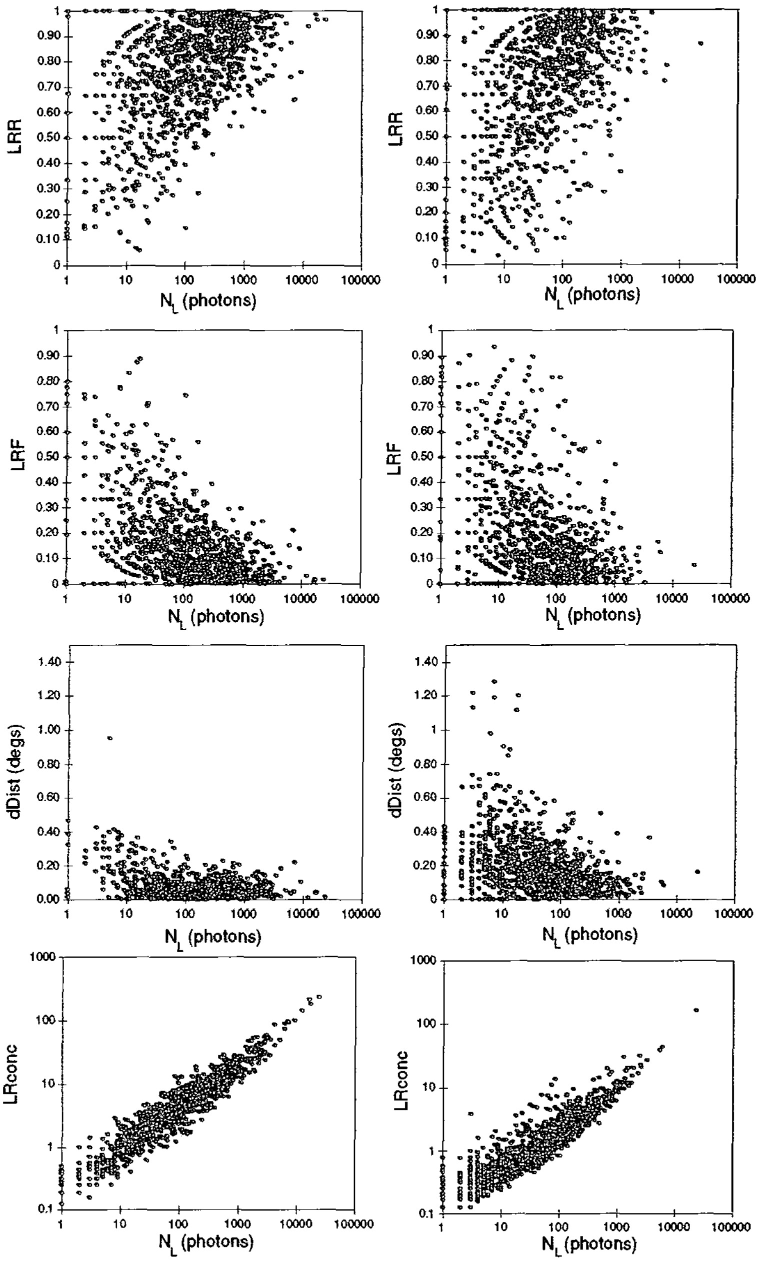

Figure 7.23: Scatter plots of various Left/Right parameters against the image brightness recorded in the left detector. The results of 1000 simulated events imaged by a pixellated detector are shown with gamma rays shown on the left and hadrons on the right.

events, especially at low energies. The parameter appears to be most effective as a gamma/hadron discriminator for the dimmer showers. It must be remembered however that these scatter plots are for events simulated without PMT noise. The previous section suggested that noise was a major obstacle to making *dDist* a successful gamma-hadron discriminant especially for events of lower brightness.

LRconc is a heavily dependent function of the image brightness. This is hardly surprising since it is a measure of the angular photon density which rises with primary energy. At the same value of N_L gamma ray events have a higher value of *LRconc* than those from hadrons. The effectiveness of *LRconc* as a gamma/hadron discriminator could be improved by defining a new parameter which has a brightness dependent term in it so that a single value of the parameter could be used for all events.

7.7 Summary

Several parameters, *LRR*, *LRF*, *dDist* and *LRconc* have been presented that may be useful in distinguishing between gamma rays and hadrons. All of these parameters show the most difference between their gamma ray and hadron distributions at large zenith angles with *dDist* and *LRconc* being the only ones to show differences at higher elevations. In all of the parameters the improvement seems to come with a changing of the shape of the gamma ray distributions with increasing zenith angle, the hadron distributions seem to remain largely the same shape.

Fluctuations in gamma ray showers seem smaller at larger zenith angles as they occur further away from the observer, as more atmosphere is traversed, and on average maximise at roughly the same altitude. The narrowing of distributions of parameters describing spatial fluctuations is due to perspective; a more distant object subtends a smaller angle than a nearer one. In addition the fluctuations in showers are dominated by low energy particles late in the shower (i.e. low altitude) which have undergone many Coulomb scatterings. These particles will cause some fluctuations in the gamma ray showers and will be more common in events from the zenith where the amount of atmosphere traversed is a minimum. For these electrons to reach the ground in events at low elevation the primary photon energy must be much higher.

Primary hadrons penetrate much further into the atmosphere before interacting and the resulting showers continue further towards ground level. In addition, to get the same Cherenkov photon density at ground level, a primary proton must be $\sim$3 times more energetic than a primary gamma ray. The hadron showers continue deep into the atmosphere giving more of the highly fluctuating low altitude Cherenkov radiating electrons as well as muons with very high penetrating power. Hence the gamma ray events appear more correlated than the hadron events which have intrinsically higher fluctuations, are randomly oriented on the sky and continue to emit Cherenkov photons deep into the atmosphere.

These simulations have been conducted up to a maximum primary energy of 20TeV, higher energies may contribute greatly to further fluctuations in gamma ray showers at low elevations. However the spectra of TeV sources are likely to follow power laws and photons of tens of TeV will be rare except for very powerful objects.

The effects of telescope optics and background starlight photon noise have been considered for a simple model of a pixellated detector. Adding noise to the events greatly reduces the ability of the parameters to discriminate between gamma ray and hadrons. However applying an analysis threshold to the data may go some way to retrieving the maximum Q factor. To see how these parameters could contribute to current analysis procedures it is necessary to construct a more complicated telescope model which takes full account of noise contributions and critically the calibration of event sizes and image correlations in all three detectors.

Chapter 8

MODELLING OF CHERENKOV IMAGES IN THE MK6 TELESCOPE

8.1 Introduction

The investigations of the previous chapter have shown a number of parameters describing the measurements that could be made to discriminate between gamma ray and hadron EAS using the Left and Right triggering detectors of the Mk6 telescope. However the effectiveness of such measurements may be limited by selections made on events using the central camera. When a more thorough treatment of the contributions from the night sky background, electronic noise etc. are included the parameter distributions are likely to change. In particular any gamma/hadron discrimination shown to be obtainable by using information from the separated Left and Right detectors may not be as powerful over a 14m baseline as that which can be obtained from the central high resolution camera. It is likely that Left/Right analysis would be most useful when applied to data already analysed using information from the central high resolution camera. Therefore it is important that the images simulated in all three detectors agree well with observed parameter distributions. A new telescope model has been made to simulate the parameter distributions for events measured in all detectors.

The ideal method of assessing how well gamma ray simulations represent what is actually detected with a telescope is to compare the simulated image parameter distributions with known gamma ray events from a known source. In the Northern Hemisphere this can be done by observing the Crab Nebula, which has been shown to be a dependable standard candle at VHE energies [64]. As yet, no such object has been discovered in the Southern Hemisphere. Hadrons however are in abundance. A telescope model can be validated by comparing real detected background cosmic ray events with simulations. If the same code is used to generate the hadron and gamma ray showers and the hadron parameter distributions agree well with observations, then at least some confidence can be ascribed to the gamma rays. The gamma ray EAS only differ from the hadrons because of their lack of strong interactions and their directionability.

A detector model has been constructed which relies as much as possible on measured quantities describing the telescope. These include the point spread function, background noise distributions and the gains of the tubes. Data taken with the Mk6 telescope from a clear night has been compared against simulation data at a similar zenith angle.

8.2 A More Accurate Noise Model for the Telescope

Many methods of simulating the PMT noise inherent in a Cherenkov telescope assume a particular shape of distribution from which to draw random fluctuations [83]. In real telescopes this may not be correct since the noise distributions of individual PMTs and channels of electronics will not only have different widths but in some cases different shapes as well. Figure 8.1 shows a typical noise distribution from a single electronics channel in the Mk6 telescope with a gaussian curve plotted against it. The noise distribution is complicated and departs significantly from the gaussian at larger numbers of digital counts. There are many sources of noise in a PMT [25]. A single photon striking a PMT has a probability of producing a photoelectron given by the quantum efficiency of the photocathode material, which depends on the wavelength of the initial photon. Thermionic emission of electrons from the photocathode also occurs randomly. The primary photoelectron is able to produce any number of photoelectrons, between 0 and a maximum given by the ratio of primary energy to the energy required to produce an 'electron-hole' pair, within the PMT dynode chain. The observed number distributions of photoelectrons vary depending on the dynode used in different PMTs. Most of the distributions fall within a class limited by the poissonian and exponential distributions [118], [54]. The Polya distribution can be used to describe this set of distributions [128];

$$P(n,b) = \frac{\mu^n}{n!}(1+b\mu)^{-n-1/b} \cdot \prod_{j=1}^{n-1}(1+jb), \tag{8.1}$$

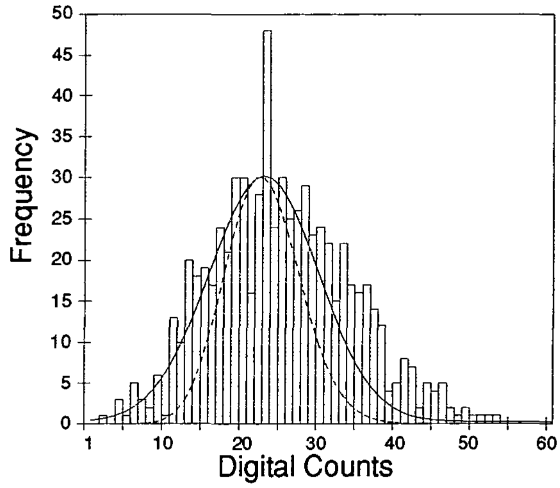

Figure 8.1: A single PMT noise distribution measured with random triggers of the Mk6 telescope (histogram) plotted against a gaussian curve, $y = 30\exp(-(x-23)^2/(2\times 7^2))$ (solid line) and a poissonian curve with mean$= 23$ (dashed line).

where $P(n,b)$ is the probability of observing n photoelectrons, μ is the mean of the distribution and b is a parameter which controls the shape of the distribution. The shape varies from a Poissonian at $b = 0$ to an exponential shape at $b = 1$. Measurements have suggested that $b \approx 0.4$ for the 1-inch Hamamatsu R1924 PMTs used in the central camera, although similar measurements have not been made on the other PMTs used in the Mk6 telescope [123]. The signals recorded by each PMT may also be subject to small fluctuations caused during the transmission to and processing of the signals by the telescope's electronics.

With the Mk6 telescope random triggers are applied throughout an observation to measure the noise distribution for each PMT and find the pedestal added to the signals. These measurements can be used as a basis for adding noise to the simulations. By applying noise formulated from these measurements to the simulations an accurate noise model can be applied to every PMT and will include contributions from all noise sources, namely the sky, the PMT photocathode fluctuations and all other electronic noise. This should lead to better agreement between measured and simulated parameter distributions than a noise model based on random noise fluctuations drawn from a theoretical distribution of an assumed shape and width.

Figure 8.2 shows the integral of the noise distribution shown in figure 8.1 with its height normalised to 1. Random noise of the exact same form as the initial distribution can be found by choosing a random number between 0 and 1. The number of digital counts of noise to add is then found where the value of the integral is equal to the random number. This is a standard method of choosing a random value from an arbitrary distribution [129].

By continually drawing random numbers in this way and adding them to the simulated Cherenkov signal the same noise conditions that act on the comparison observation file are reproduced. The amount of noise added to the observed data is not totally described by the randomly triggered background distributions, which are caused by photon count fluctuations in the night sky background and variations in the instantaneous PMT gain. The amount of noise rises with the brightness of the incident Cherenkov signal. This increase can be approximated using another feature of the Mk6 telescope's normal operating conditions. A Nitrogen laser is randomly flashed into a scintillator during an observation and, via optical fibres and an opal diffuser, provides a light source used to flat field the PMT gains. The single PMT pulse response histograms from the laser pulses give wider distributions to those from the randomly triggered ones.

The laser flashes in the Mk 6 telescope are triggered randomly at a rate of

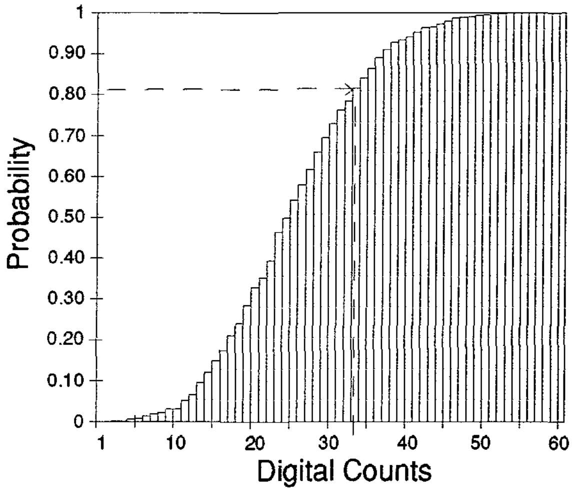

Figure 8.2: The integrated form of a single PMT noise distribution measured with random triggers of the Mk6 telescope can be used to form a probability distribution. A uniform random number from 0 to 1 can be used to find noise to add to simulations which accurately reproduces the observed noise.

50/min and vary in intensity from flash to flash. A mean flash intensity for the observation can be found for each detector by averaging the sum of signals from all its PMTs for each flash (~700 flashes in a 15m observation). The ratio of the mean flash intensity to the intensity of each single flash is then calculated. This ratio is used to normalise the response of each PMT to a given flash, allowing the creation of a distribution of the relative signal response seen by each PMT during the observation. Finding the width of the distribution gives an estimate of the noise added when an averaged bright signal is recorded. The noise found by this method should be due largely to the fluctuations in PMT response and not the variation in laser flash intensity. Assuming a linear relation between the standard deviations and the flash brightnesses of the random and laser flash

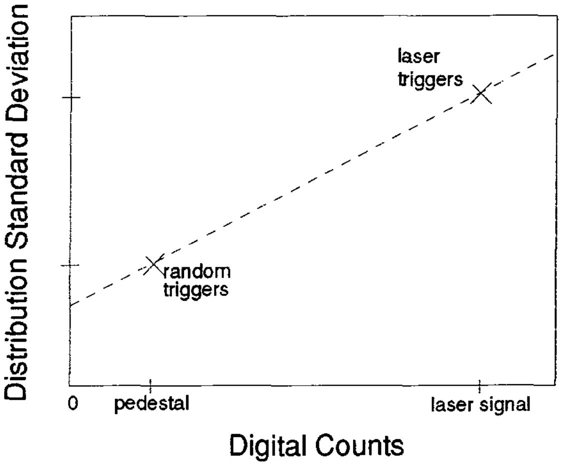

Figure 8.3: An estimate of the increase in PMT noise with rising Cherenkov signal.

distributions gives an estimate of the noise as a function of Cherenkov signal (figure 8.3). The gradient of this graph gives a ratio by which noise chosen from the random trigger pulses can be scaled according to the brightness of the Cherenkov signal in a particular PMT. Measurements suggest that the gradient of the standard deviation v signal brightness curve ranges from 10-20% depending on the particular PMT involved.

8.2.1 Point Spread Function

The PSF of the Mk6 telescope's central mirror has been measured by tracking a bright star with the telescope and using a CCD camera to take an exposure of the stellar image projected at the prime focus. The results of one of these measurements was shown in section 5.1.2. Similar measurements of the PSFs of the Left and Right mirrors have not been made. However, all three mirrors were constructed at the same time from the same vacuum mould and this work assumes each mirror has identical PSFs.

Table 8.1: Calibration factors for Mk6 telescope PMTs found using a radioactive light pulser.

PMT	PMT Name	Calibration (dc/γ)
Center	Hamamatsu R1924	1.1
Guard ring	Burle 8575	0.1
Left/Right	Philips XP3422-SG4	0.55

8.2.2 PMT Gain

The Cherenkov photons which hit a particular PMT's photo-cathode create photo-electrons, the number of which increase as they cascade in the PMT's dynode chain. The resulting signal is transmitted as a fast analogue signal to the telescope's triggering electronics. If triggered, the signal is stored as digital counts. A calibration constant is required to convert the Cherenkov photons simulated with the GENESIS program to digital counts. A small 'pill' of plastic scintillator containing a dissolved α particle source (^{241}Am) has been used for absolute calibration of all PMTs. The pill produces pulses of ~300 photons at a rate of 700Hz which gives (283.3 ± 0.5)dc in the 1-inch PMTs of the central camera [143]. Further measurements on the other PMTs used in the Mk6 telescope are shown in table 8.1.

8.2.3 Triggering

A simple trigger criterion has been applied to the simulated data requiring that the integral signal in corresponding Left and Right PMTs passes a set threshold. The value of this threshold is set by measurements of the minimum triggered signal in observational data. Inspection of the brightest pair of corresponding Left and Right PMTs in each event for observed data with more than 200dc detected in the central camera has suggested that at least one pair of triggering PMTs should detect more than ~30dc. The 200dc selection was applied to ensure measurable image parameters in the central camera, rather than the very dimmest events. This arbitrary selection does not lead to a good representation of telescope at the minimum energy threshold of its operation. Simulations to find the energy threshold and effective area of a Cherenkov telescope to a high precision would require a full consideration of the spectral and temporal responses of all the PMTs. However, the primary interest here is the appearance of the imaged parameter distributions and this simple trigger allows reductions in computational requirements. The parameter distributions shown in figures 8.5 and 8.6 have involved a pre analysis requiring that the central camera image brightness of the events is greater than 1000 digital counts. Events of this size are expected to have a maximal chance of triggering the telescope, based on measurements of the peak of the image brightness distributions of observed events. Below this size the simulations show a paucity of events with small values of size and shape parameters.

8.3 Comparisons of Observed and Simulated Hadron Events

Model parameter distributions are shown against those obtained from an observation in figures 8.5 and 8.6. The modelled distributions show the results of simulating an integral primary energy spectrum ($\alpha = 1.6$) of hadronic cosmic rays at 30° zenith angle. The observed data was taken from observations at a similar zenith angle to the simulations. A number of calibrations have needed to be made to account for certain differences in the data and are described below. The data used comprises ~3600 simulated and ~1100 observed events. The simulations agree well with the observed data for many of the parameters shown. Image parameters are displayed in the following figures as 50 bin histograms.

8.3.1 Correction for Detector Sensitivity

There is a slight difference in the sensitivity to Cherenkov light of the two triggering detectors of the Mk6 telescope due to the relative performances of the PMTs in each detector. On average the right detector is less sensitive than the left by $\approx$ 15%. This is because the PMTs installed in the Left and Right detectors were decided by manufacturer's batch number, with a less sensitive batch of PMTs being installed in the Right detector. To counter act this effect the total amount of light detected per 15 minute data segment is found for each detector and the gain of each PMT in the less sensitive detector multiplied by a normalisation factor equal to the ratio of the response in the detectors. Any fluctuation in an event's brightness between the two detectors averages out over the thousands of

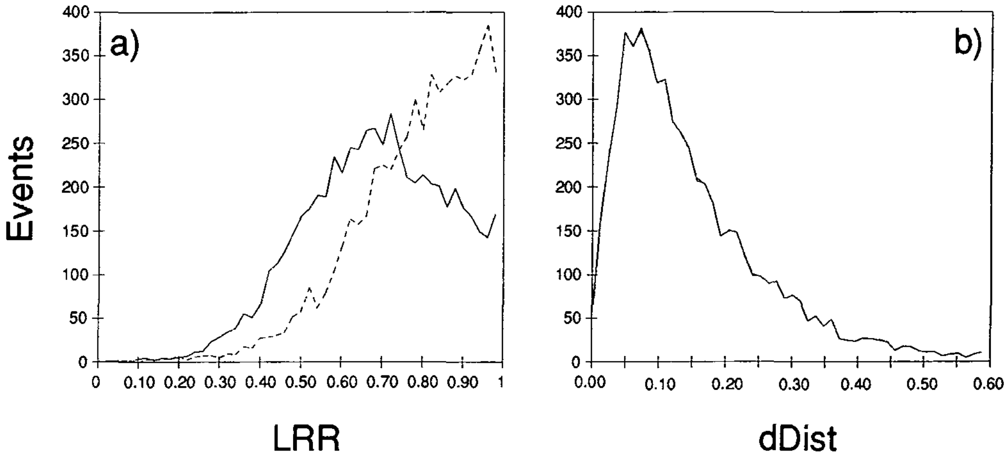

Figure 8.4: The effect of 'balancing' the gains of the Left and Right detectors on a) *LRR* and b) *dDist*. Both graphs show the data from the same 15 minute observation before (solid line) and after (dashed) balancing.

events in a data segment. This correction, known as 'balancing', is important when measuring quantities based on the calorimetric energy content of the EAS such as *LRR* and *LRF*. It is important to point out that this correction in no way affects the determination of the centroid of an image in the detector (see figure 8.4).

8.3.2 Correction for Optic Axis Alignment

Great care was taken during the construction of the telescope to ensure that the optic axes of all mirrors and detector systems were aligned to allow the efficient operation of the three fold spatial trigger system. The alignment between the Left and Right optic axes is true to better than 0.1° . In addition, the telescope is a particularly sturdy structure; as the telescope steers from the horizon up to the zenith the divergence of the Left and Right optic axes caused by flexing of the structure is small, of the order a few hundredths of a degree. When attempting to accurately measure fluctuations in the centroid position of events measured in both detectors it is important that any misalignment, even on this small a scale, is included in the moments calculation. For example the parallax difference in a shower maximising at 12km altitude imaged by two detectors separated by 14m is $\approx 0.08^\circ$. Differences in the alignment of the optic axes can be monitored for each data segment by finding the average centroid position in each detector of every event in a pre-analysis data segment. Any fluctuations on an event by event nature will cancel out if large numbers of events, which will be mostly due to the isotropic cosmic ray background, are averaged. This process returns offsets which can be applied when calculating the first order moments in one of the triggering detectors. The effect of this is to shift the *xdDist* and *ydDist* distributions so that their means are at the origin.

For the Cen X-3 data used in this study the offsets were found to be -0.11° and 0.04° in the x and y directions respectively. When comparing simulations of *dDist* with observed data, offsets were applied to ensure that the the *xdDist* and *ydDist* distributions had means at the origin. These were found to be -0.03° and 0.0° in the x and y directions respectively. There is no detectable difference in the the *xdDist* offset between gamma ray and hadron simulations.

8.3.3 Discussion of the Simulated and Observed Parameter Distributions

In general the simulated high resolution camera parameter distributions agree well with the observations. An exception is seen in *Ellipticity* which indicates that the simulated hadron events appear on average slightly 'rounder' than the observations. The mean of the observed *Ellipticity* distribution is (0.656 ± 0.04)° compared with (0.694±0.02)° for the simulations. The standard deviations of the two distributions is ~0.140° . This seems largely to be due to a slight shortening of the mean *Length* of the events since the *Width* distributions agree very well. Improving the agreement between the *Length* distributions can be achieved by adjustment of the noise and optical models. However this is at the expense of the excellent agreement of the *Width* and other distributions. This may suggest that the problem lies at the shower generation stage of the simulation.

The *Length* of a Cherenkov image describes the longitudinal development of the shower. An over dense or under transmissive atmosphere model in the simulation code could lead to shortening of the mean *Length*. There is also a small excess of simulated events with small values of *Alpha* which has proved difficult to resolve. This effect would be expected if the initial hadrons did not come from a spatially isotropic distribution. The genesis code used for these simulations was extended to randomise the positions of the hadron images within the detector focal plane by more than 2 times the telescope's field of view (at the expense of event acception efficiency !). This should be more than enough to fully randomise the hadron arrival directions. A note that should be added is that the uncertainty in the measurement of *Alpha* is a function of *Ellipticity*. The complicated algebra required to prove this statement will not be discussed here. However it is obvious that measuring the pointing direction of an event gets harder as *Ellipticity* increases, until the point where the event is circular and *Alpha* is undefined. It is possible that the discrepancy between the simulated and observed *Ellipticity* distributions may, if not responsible, be linked to the

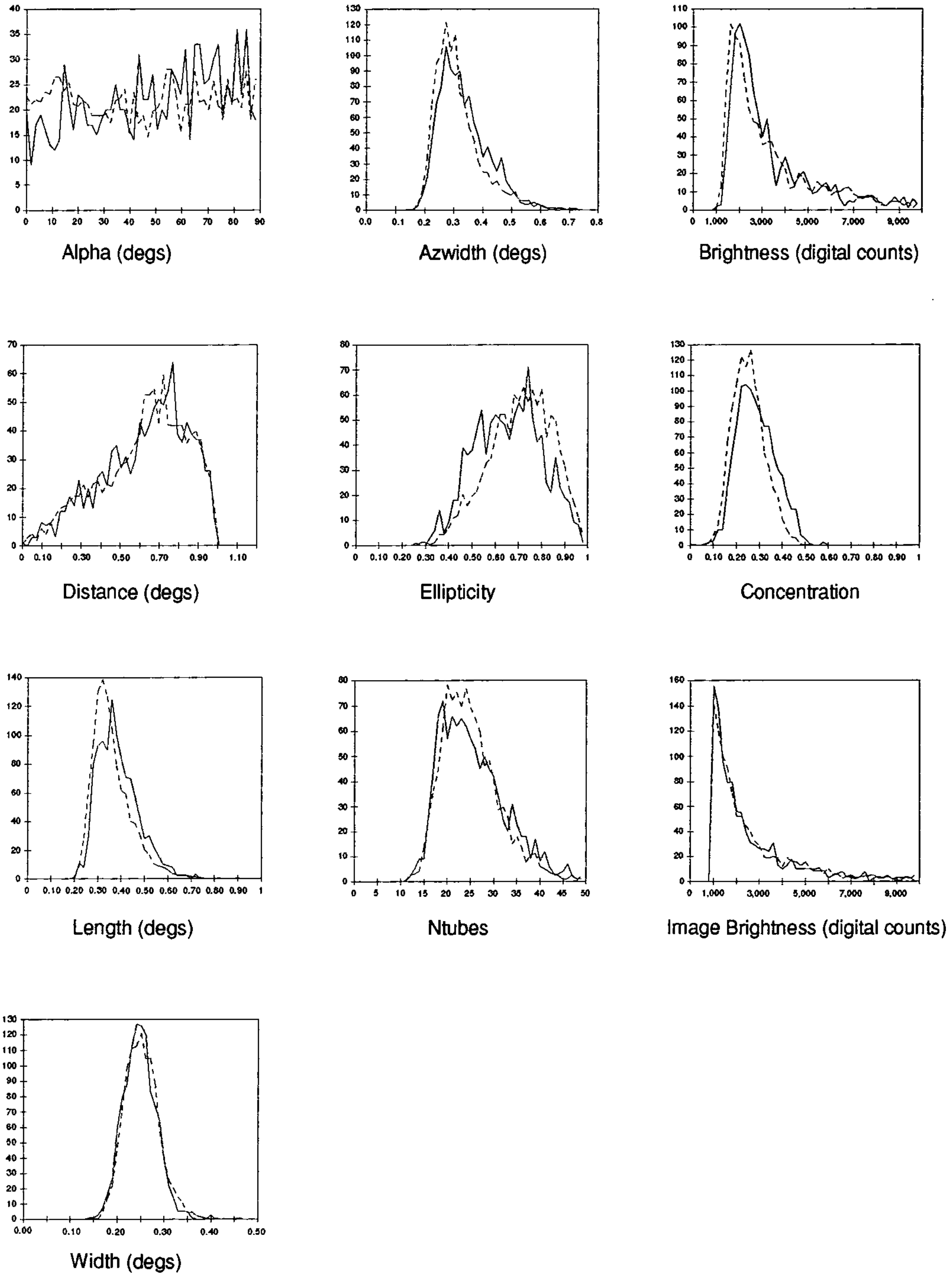

Figure 8.5: Comparisons of central camera image parameter distributions for simulated (dashed) and observed (solid) hadron events.

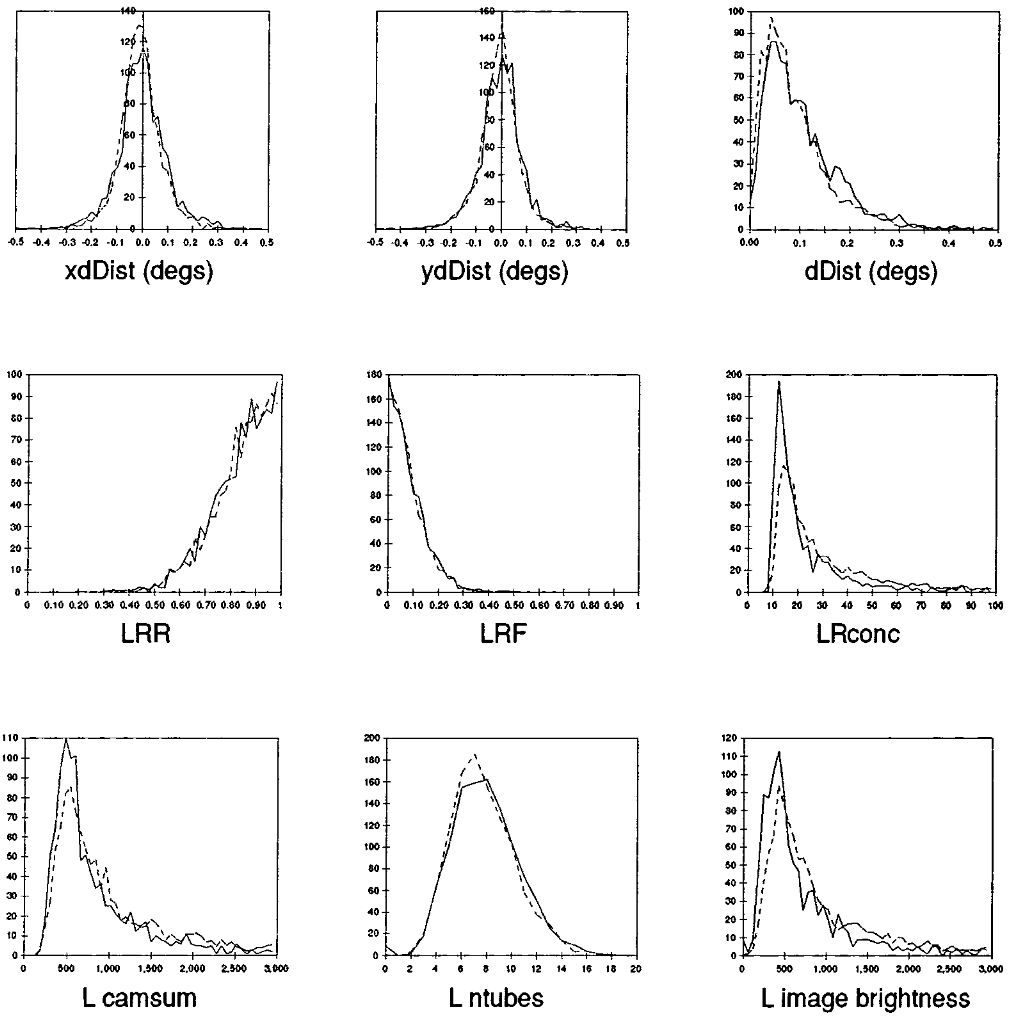

Figure 8.6: Comparisons of Left/Right detector parameter distributions for simulated (dashed) and observed (solid) hadron events.

excess of simulated events with small *Alpha*.

The simulated Left/Right distributions compare very well with the observations although there are some deficiencies in the simulated data at lower brightnesses. There are two main assumptions which have been made in the modelling of these parameters which should be borne in mind:

The first is that the optical performances of the Left and Right mirrors are the same as each other and have been described by the same profile used for the centre mirror. This is probably reasonable since the mirrors were manufactured and installed to the same specifications. In addition the pixel size of the Left and Right detectors is 2 times that of the central camera and so accurate modelling of the PSF here should not be as important as it is for the central camera. None of the parameters, except perhaps *LRconc* which is effectively a measure of the ratio of light contained within and outside of selected 'image' PMTS, are heavily dependent on the PSF. However it is still true that the PSFs of the Left and Right mirrors have not been independently measured and included in this model.

The second assumption is that applying a very simple triggering criterion backed up with a central camera *Brightness* cut is adequate. A more accurate model would need to take account of the three-fold coincidence trigger system, relying on information of the Cherenkov photon arrival times and the telescope pulse response. If modelled successfully a differential trigger in the simulations should improve the success of the model for low *Brightness* events.

The model discussed here appears to describe the performance of the telescope fairly accurately for hadron initiated events of mid-large brightnesses. These events will now be used to suggest an analysis routine for Cen X-3 data.

8.4 Simulated Estimation of Data Cut Values

Shown in figures 8.7 and 8.8 are the simulations of gamma ray and hadron induced Cherenkov events. The central camera parameters which show differences between the gamma ray and hadron events are the familiar Hillas parameters of section 6.2.1, such as *Length*, *Width* and *Alpha*. *Azwidth* has been shown for interest only; although it would appear to be a useful gamma/hadron discriminant it retains hadron events that are very 'gamma like'. The differences in the *Alpha* distributions of events surviving an *Azwidth* cut is not as significant at small values of *Alpha* as those for events selected by other methods (recall figure 6.5).

There would not seem to be much discriminating power to be obtained from any of the Left/Right parameters. This is not as disappointing as it first appears as the events are still very much in a raw state with only the required condition that they all contain $>$ 1000 digital counts in the camera image. The plots of figure 8.8 merely tell us that the Left/Right detectors pairing is not as sensitive a gamma-hadron discriminator as the centre high resolution imaging camera. To further assess the effectiveness of the Left/Right parameters it is necessary to investigate whether they offer any further discriminating power after a standard analysis based on central camera parameters has been performed. The simulations will first be used to provide a set of cuts which can be compared with analysis procedures used on observations of the HMXRB Cen X-3.

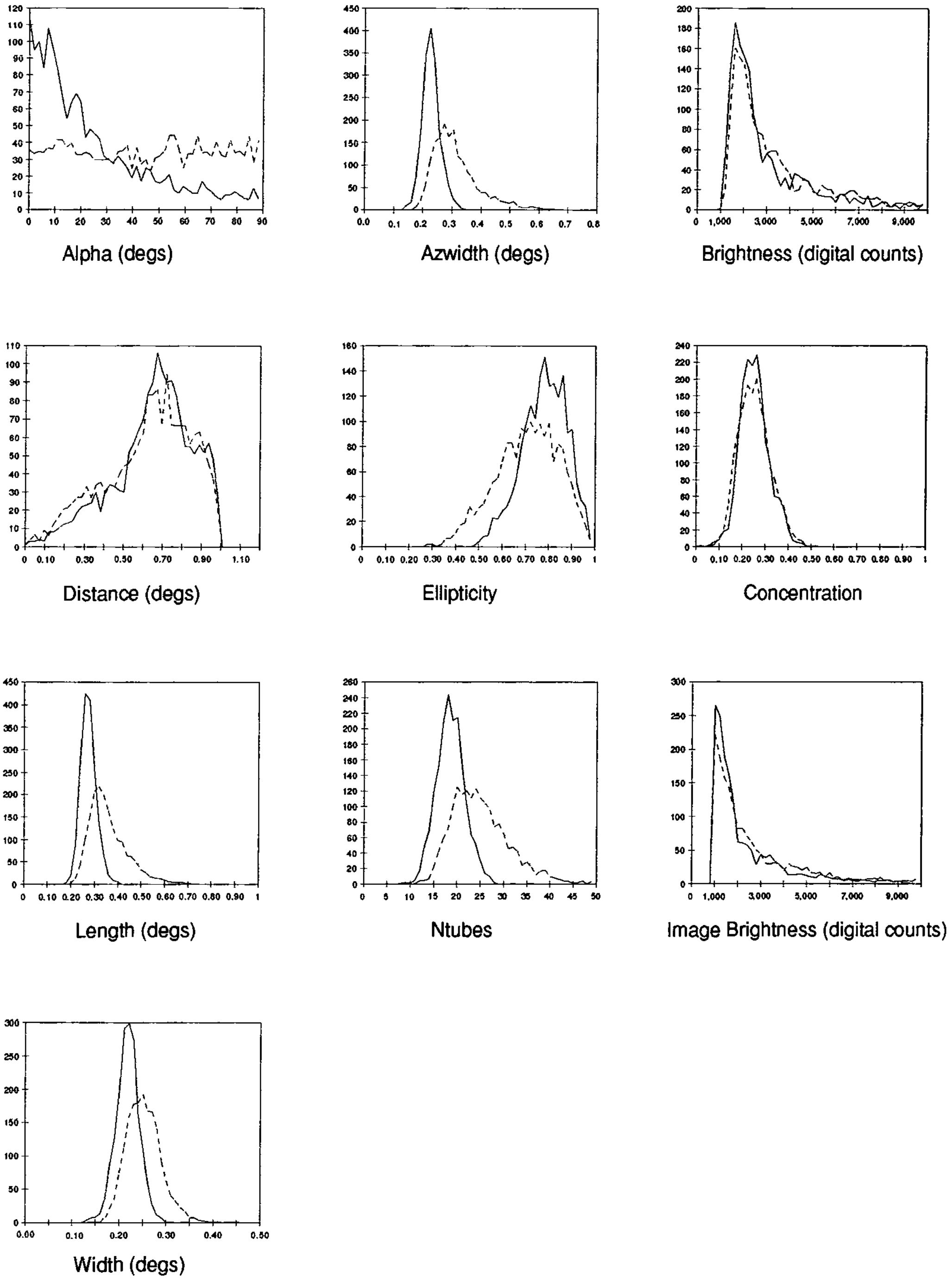

Figure 8.7: Comparisons of central camera image parameter distributions for simulated energy spectra of hadron (dashed) and gamma ray (solid) Cherenkov events.

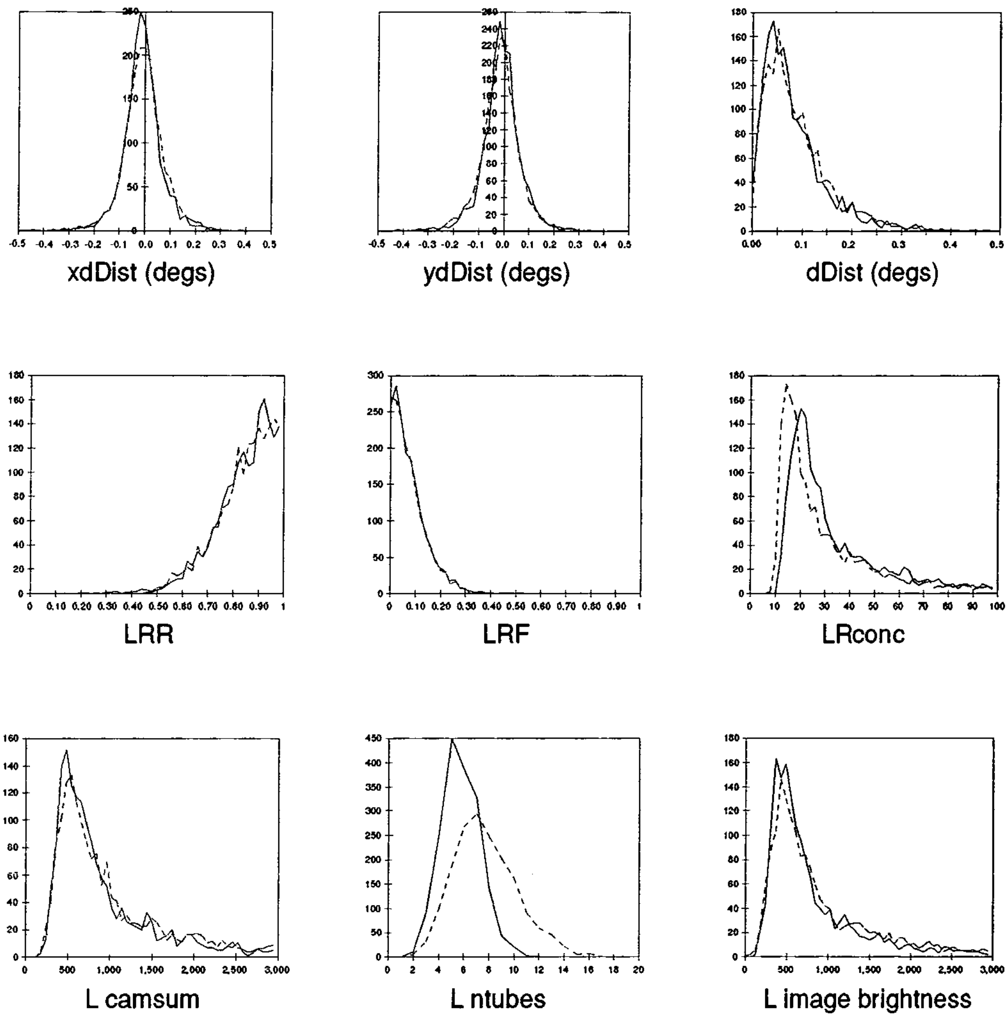

Figure 8.8: Comparisons of Left/Right detector parameter distributions for simulated energy spectra of hadron (dashed) and gamma ray (solid) Cherenkov events.

8.4.1 Analysis of Cen X-3 Data

Observations made during March and June 1997 with the Mk 6 telescope of the HMXRB Cen X-3 have found emission of VHE gamma rays [38]. An initial analysis of the data removes images of very low brightness and events which fall near the edge of the central detector. After these selections there remains 64713 and 65171 events in the on and off source data sets respectively. The significance, defined as

$$N_\sigma = \frac{N_{ON} - N_{OFF}}{\sqrt{N_{ON} + N_{OFF}}}, \qquad (8.2)$$

of the difference between the on and off source data sets is 1.3σ. Further analysis is applied to the events using the IACT. The values of the image parameter cuts used in the analysis of this source follow.

1. $800 < Brightness < 20000$ digital counts (corresponding to greater than ~400GeV of primary gamma ray energy),
2. $0.3° < Ellipticity < 0.85°$, required to enable *Alpha* to be measured without large uncertainty,
3. $0.35° < Distance < 0.75°$, required to allow gamma ray images to appear far enough away from the camera centre to be elongated but not too near the camera edge,
4. $Width < 0.28°$,
5. $dDist < 0.07°$, the approximate angle expected to be subtended by gamma ray showers maximising at ~11km distance when viewed by two detectors separated by 14m.

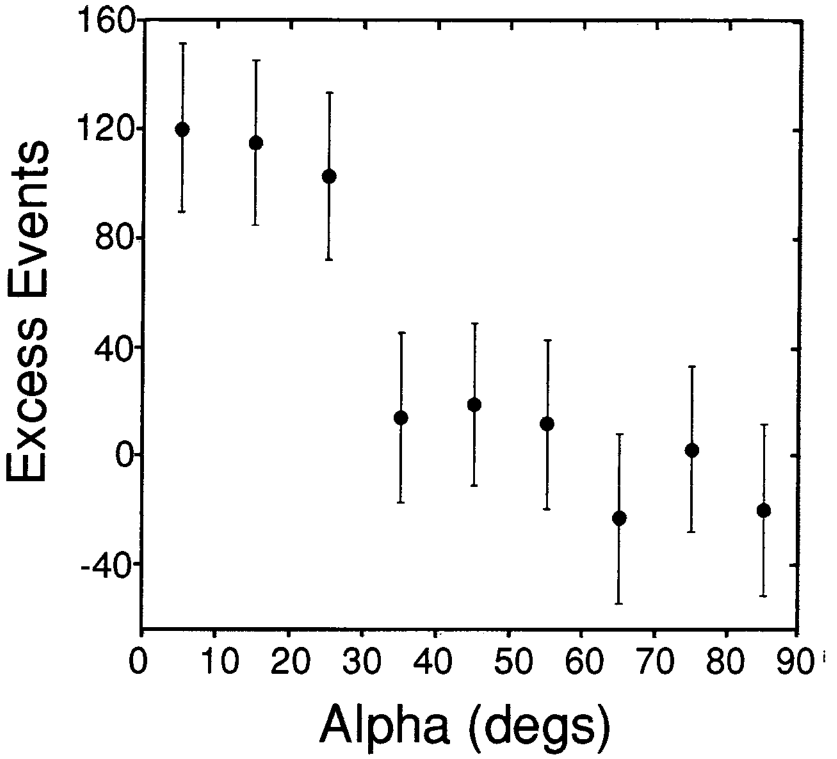

Figure 8.9: The difference in the on and off source *Alpha* distributions.

After these selections a 3.7σ significant excess of 342 events is observed in the on source data set which contains 4429 events. The difference in the on and off source *Alpha* distributions is shown in figure 8.9. It is clear that the majority of the excess at small values of *Alpha* $< 30^\circ$. Cutting the data at *Alpha* $= 30^\circ$ give 1546 and 1208 events in the on and off source data sets, significant at the 6.4σ level (figure 8.9). A false source analysis can be used, following the same analysis procedure, for a matrix of points in angular space around the expected source position. Figure 8.10 shows the plot of the false source analysis for the data considered here and shows that the excess of on-source events are clearly co-located with the position of Cen X-3.

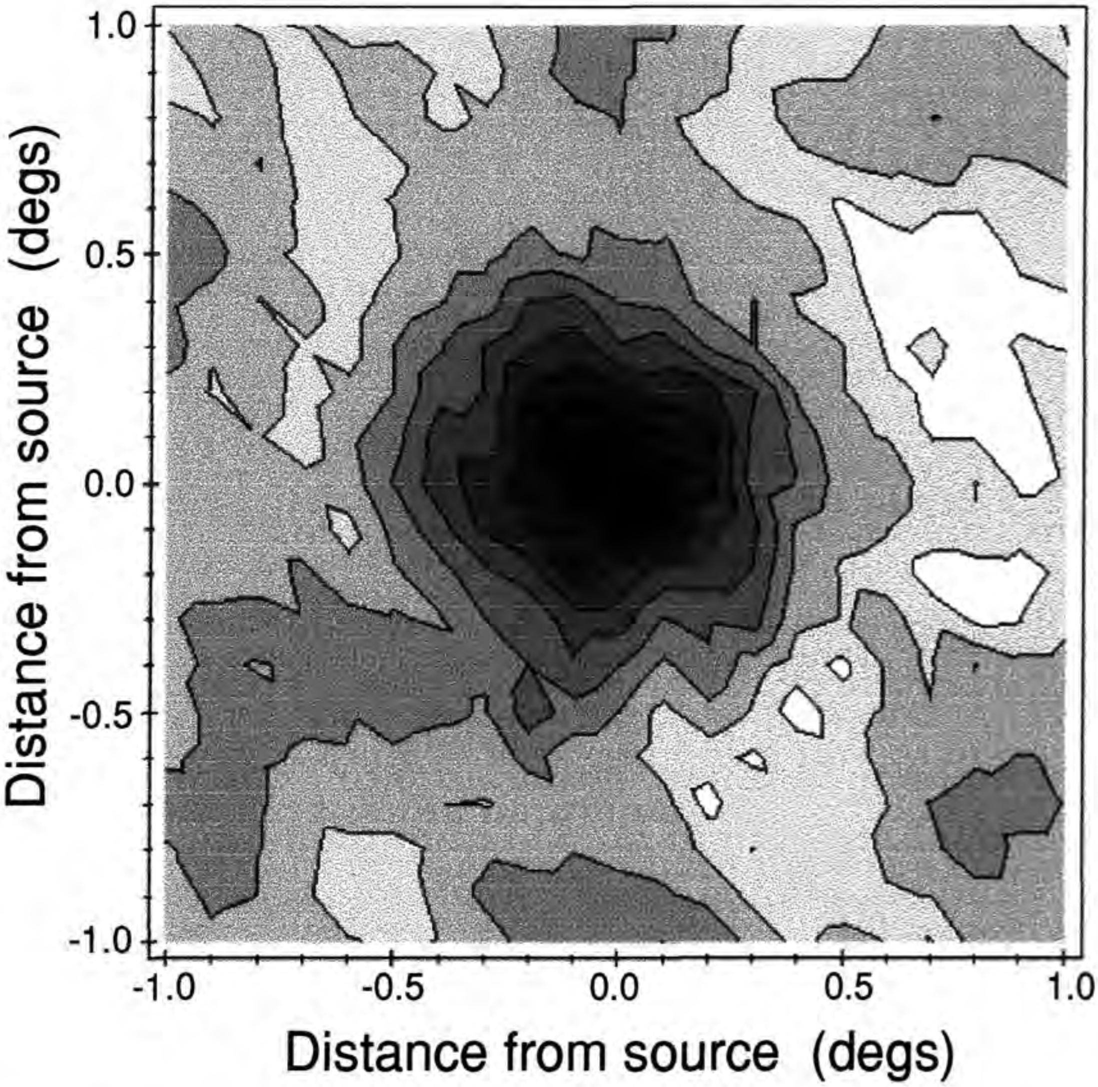

Figure 8.10: False source analysis for excess events with *Alpha* less than 30° . The contour map indicates the significance of a gamma ray signal arriving from each direction in 1σ contours. Black indicates a probability $> 6\sigma$ and white $< -3\sigma$.

8.4.2 Maximization of Simulated Gamma Ray Signal using Centre Camera Parameters

The simulated images of gamma ray and hadron induced Cherenkov events have been used to produce a series of cut values for each of the parameters used in the analysis of data from Cen X-3. The initial three cuts in the Cen X-3 analysis are designed to improve the quality of the data rather than as gamma/hadron discriminators. It is this philosophy which is followed here:

1. $1000 < Brightness < 20000$ digital counts,
2. $0.30° < Ellipticity < 0.84°$, the upper cut on this parameter has been increased by the difference in the means of the simulated and observed *Ellipticity* distributions,
3. $0.35° < Distance < 0.75°$.

These cuts retain 637 gamma ray and 1099 hadron events and the 'cleaning' cut or 'cleaned' data set will be referred to from now on as these analyses or events.

The simulations of figure 8.7 suggest that gamma rays have smaller *Widths* than hadrons. Figure 8.11 shows the quality factor obtained by rejecting events with *Width* above a certain value. The peak quality factor is 1.6 obtained for $Width < 0.23°$ retaining 554 of the gamma rays and 334 hadrons. The Cen X-3 data analysis used events with $Width < 0.28°$. Almost all (635) of the gamma rays are within this *Width* selection compared with 844 of the hadrons, a quality factor of just over 1.1. If the simulations are accurate then the analysis applied to

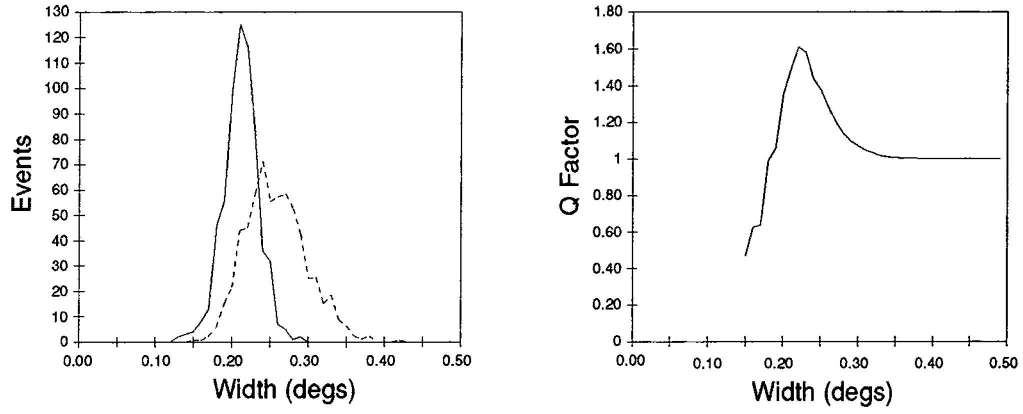

Figure 8.11: (a) The distributions of *Width* for gamma ray and hadron events surviving the initial cleaning cuts. (b) The quality factor function for a *Width* cut on the data.

the Cen X-3 data set preserves the richness of the gamma ray signal but does not maximise the signal to noise ratio. When observing a candidate source of VHE gamma rays a cut which maximises the quality factor, and thus the significance of the detection, is desirable. For observations of a known source of gamma rays, to make measurements of its energy spectrum for example, it may be more useful to have the maximum possible numbers of gamma ray events remaining from the cut.

The events identified by the analyses of this section will now be used to determine if the Left/Right parameters can be used to further improve the simulated signal.

8.5 Gamma Hadron Discrimination Using Left/Right Parameters

The simulated gamma ray and hadron events have been cleaned using the methods outlined in section 8.4.2. The analysis now follows two routes to allow the prediction of the maximum signal which may be obtained with the Left/Right parameters. The signal to noise maximising ($Width < 0.23°$) and signal preserving values ($Width < 0.28°$) of $Width$ suggested above have been used along with an $Alpha < 30°$ requirement, as used in the Cen X-3 analysis. The remaining events are summarised in table 8.2. For reference these two data sets will be known as 'W28' and 'W23' from hereon. Although the aim of these investigations is to maximise the sensitivity of the telescope by increasing the quality factor of the cuts, the W28 data has also been considered. This is for two reasons; firstly the $Width < 0.28°$ is the cut actually used in the Cen X-3 analysis and secondly the W23 hadron data set contains only ~100 events in. The ~3× more events in W28 will allow slightly better statistics on any distributions plotted.

These events have then been subjected to various combinations of analysis using the Left/Right parameters suggested in Chapter 7. The first of the following sections discuss the effects of *dDist*, *LRR*, *LRF* and *LRconc* on W28 and W23. These are then followed by an investigation into applying a selection criteria to the signals used in calculating the parameters, similar to that shown in section 7.5.1. A final discussion of the effectiveness of these analyses is given in section 8.6. The quality factors for the cuts outlined above are not very large when compared with those quoted for other IACT telescopes. For example the Whipple collaboration

Table 8.2: Remaining simulated events after the cleaning cut outlined in section 8.4.2 have been applied along with *Alpha* $< 30°$ and two *Width* cuts. The Quality factor of the cutting the cleaned data are shown.

Name	*Width* cut	Gamma-Ray Events Remaining	Hadron Events Remaining	*Q* factor
W28	<0.28°	492	315	1.4
W23	<0.23°	384	112	1.9

claim to be able to remove 99% of their background events to retain a quality factor of > 5 with their 'supercuts' technique [105], [117]. It should be noted that these numbers include the rejection of muon events from the data. Unlike single dished telescopes the three-fold coincidence trigger of the Mk6 telescope does not trigger on muon events and may achieve some gamma/hadron discrimination with its trigger. Therefore the initial data set for the Mk6 telescope is smaller and a larger fraction of the events is retained by the analysis cuts thus reducing the quality factor. Improvements to the Durham analysis routines have also been made by varying the selections made on the basis of the size of the image. The simulated data set used in this work is not large enough to consider such an analysis.

8.5.1 Effects of Left/Right Parameter Cuts on the W23 and W28 Data Sets

The distributions of the Left/Right Parameters for the events described in table 8.2 are shown in figures 8.12 and 8.13. The results for both the W23 and W28 data sets are disappointing with no clear difference between the distributions for all but *LRR*. The value of *LRR* for hadrons dips significantly below the gamma ray distribution near 1. However the peak quality factor that would be obtained by rejecting events with values of $LRR < 0.9$ is only just above 1. This is due to the large numbers of gamma ray events that would be lost with such a cut.

8.5.2 Selecting PMTs for Parameter Calculation based on Signal to Noise Ratio

Investigations were performed on the initial simulations in section 7.5.1 in the presence of a flux of background photon noise, but with no optical spreading. It was indicated that an improvement to the effectiveness of the Left/Right parameters may be obtained by selecting which PMT signals to include in the calculation of the parameters on the basis of their brightness. This method has been used on these simulations by only including signals above a certain threshold set in units of the RMS widths of the individual PMT's random noise distribution (see section 5.3.2). The results of using this method are shown in figures 8.14 and 8.15

In both the W28 and W23 data an improvement is seen in the quality factor obtained from *dDist* and *LRconc* cuts. In both cases the best quality factor is

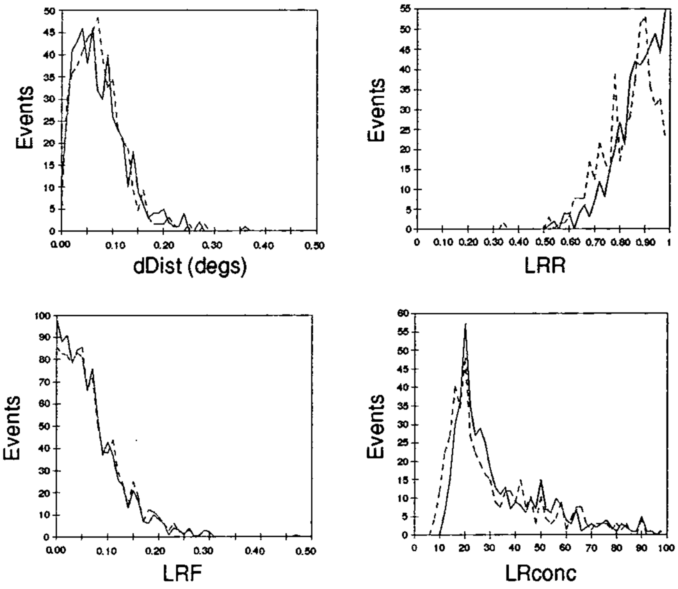

Figure 8.12: (a) The distributions of Left/Right parameters for gamma ray (solid line) and hadron (dotted line) events surviving the W28 analysis.

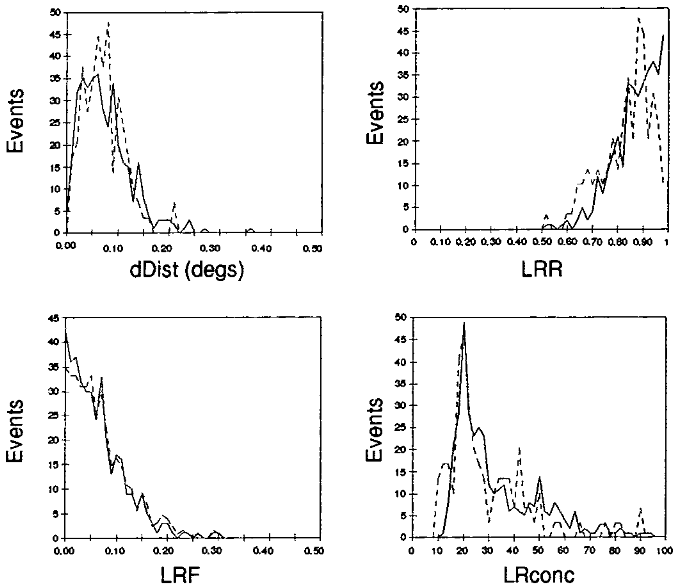

Figure 8.13: (a) The distributions of Left/Right parameters for gamma ray (solid line) and hadron (dotted line) events surviving the W23 analysis.

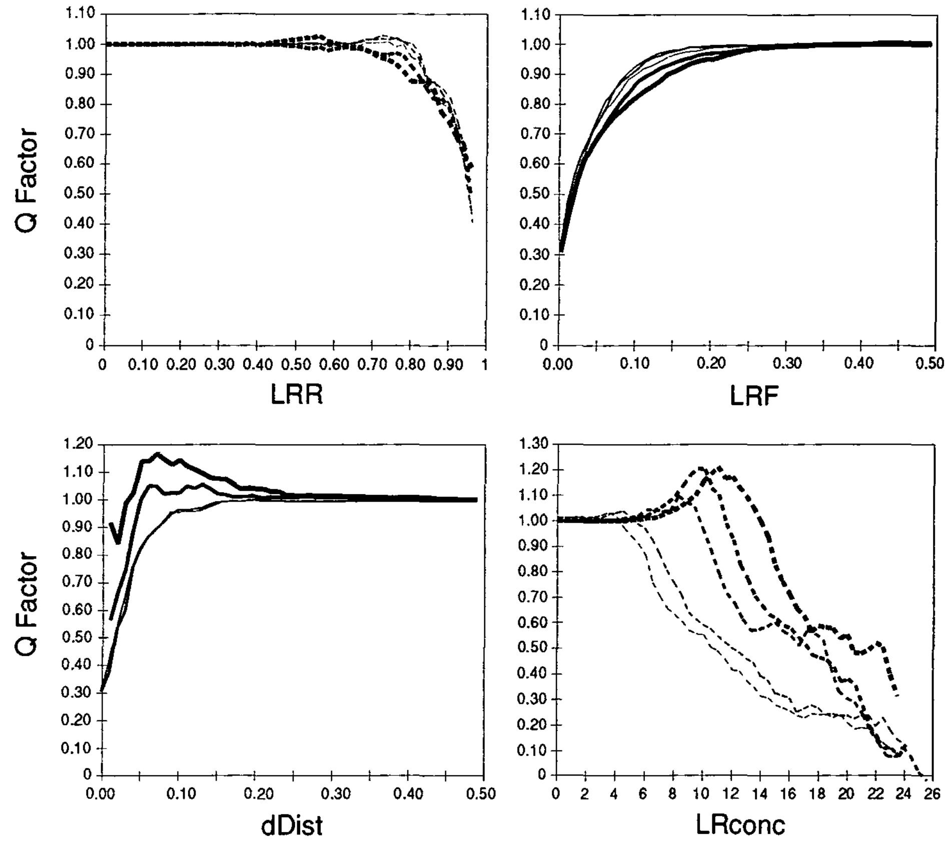

Figure 8.14: The quality factor functions when the W28 data are cut on Left/Right parameters calculated from PMT signals above a certain brightness. Shown is the effect of using signals brighter than 0.5×(thinnest line), 1×, 2×, 4× and 6×(thickest line) times the RMS width of each PMT's random noise distribution. The dotted lines indicate that events below a particular value of the parameter are rejected. The solid lines indicate that the events with the smaller values of the parameter are retained.

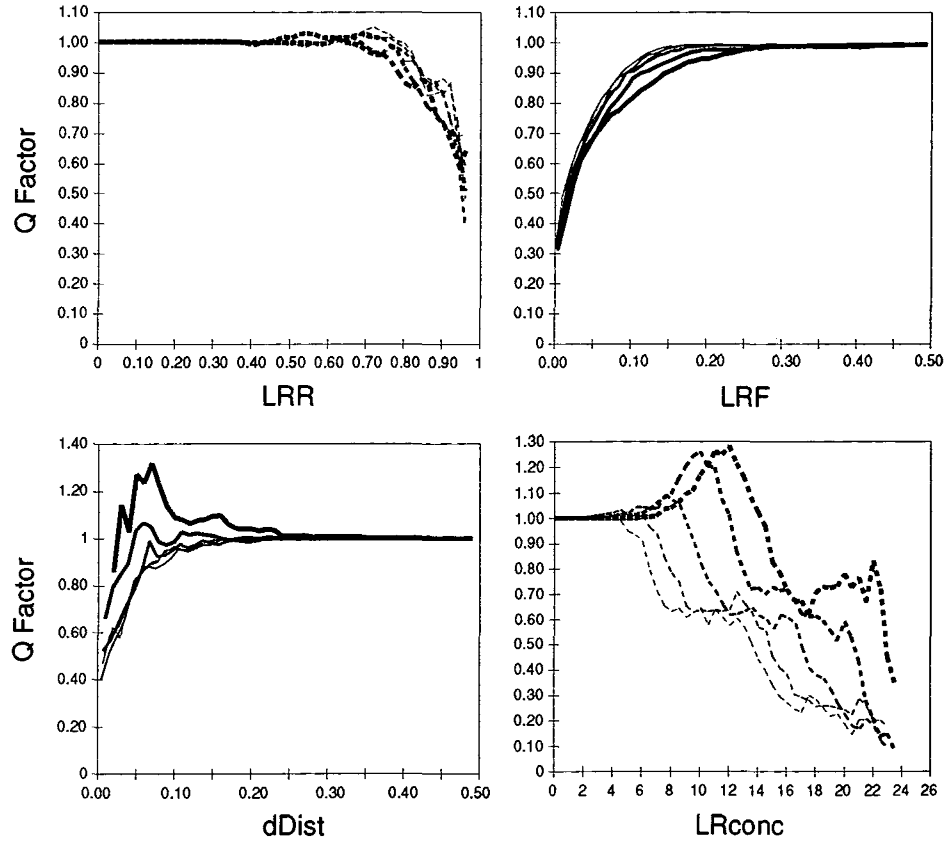

Figure 8.15: The quality factor functions when the W23 data are cut on Left/Right parameters calculated from PMT signals above a certain brightness. Shown is the effect of using signals brighter than 0.5×(thinnest line), 1×, 2×, 4× and 6×(thickest line) times the width of each PMT's random noise distribution. The dotted lines indicate that events below a particular value of the parameter are rejected. The solid lines indicate that the events with the smaller values of the parameter are retained.

obtained when the threshold level is set to 6 times the width of the PMT noise distributions. Both data sets suggest that events with *dDist* $> 0.07°$ should be rejected from analysis. This is very interesting as it is the same value of *dDist* cut that was applied *a priori* to the Cen X-3 data, although without the selection on PMT signal. The *dDist* quality factor functions in the figures show a small peak at $\sim 0.07°$ in the 2σ case which gets bigger as the threshold increases. The simulations also suggest that rejecting events with *LRconc* < 11 may improve the analysis quality factor. The distributions of these parameters are shown in figure 8.16. There is a possibility that a further improvement for *dDist* may be made by increasing the threshold further. However it was found that the smaller events in the data failed to register any PMTs above this brightness causing errors to occur in the calculation of the parameter. Work is continuing to solve this problem but will not be discussed further in this thesis. Table 8.3 shows the effect of applying the cuts suggested here and in the previous sections to the cleaned data. Applying both *dDist* and *LRconc* selections to the data improve quality factors slightly, although it is clear that *dDist* $< 0.07°$ is a more dominant selection than *LRconc*.

8.6 Summary

A detailed model of the Mk 6 telescope which takes full account of the sources of noise and the telescope optics has been used to simulate the appearance of the Cherenkov images of hadron and gamma ray EAS. Modelled images of hadron induced Cherenkov events have been compared against observed data and agree well. By following a similar analysis strategy to that applied on data from the

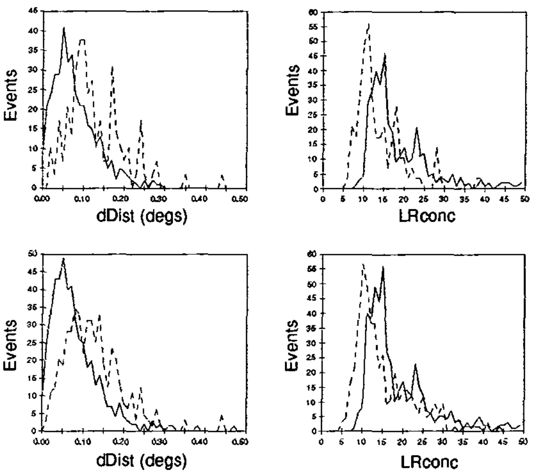

Figure 8.16: The distributions of Left/Right parameters calculated from signals greater than 6 times the PMT random noise distribution width. Gamma ray (solid line) and hadron (dotted line) events surviving (top) the W23 and (bottom) W28 analyses are shown.

HMXRB Cen X-3 [38] a set of cuts have been calculated which pick a strong gamma ray signal from the data. The remaining events have been used to investigate the effectiveness of the Left/Right parameters *dDist*, *LRR*, *LRF* and *LRconc*. None of these parameters are effective at increasing the gamma ray signal unless a selection criteria is placed on the signals used in the calculation of the parameters. If signals which are 6 or more times larger than the RMS noise distribution width of each PMT in the Left and Right detectors are used, *dDist* and *LRconc* can improve the quality factor of current analysis.

The next step in this continuing work would be to apply these cuts, or slight variants of them, to observed data from a confirmed gamma ray source and see if detection significance is improved. An improved model may be necessary to continue investigations into lower brightness events and other Left/Right parameters.

Table 8.3: Remaining simulated events after the cleaning cuts outlined in section 8.4.2 have been applied along with *Alpha* $< 30^\circ$, the two *Width* cuts suggested in 8.4.2 and the Left/Right analyses shown . The Quality factor of cutting the cleaned data are shown.

Width cut	*dDist* cut	*LRconc* cut	Gamma-Ray Events Remaining	Hadron Events Remaining	Q factor
<0.28°	<0.07°	none	286	78	1.7
<0.28°	none	>10	463	220	1.6
<0.28°	<0.07°	>10	270	72	1.7
<0.23°	<0.07°	none	219	21	2.5
<0.23°	none	>11	343	61	2.3
<0.23°	<0.07°	>11	212	17	2.7

Chapter 9

SUMMARY AND FUTURE WORK

9.1 Summary

The Imaging Atmospheric Cherenkov Technique (IACT) has been used by ground based gamma ray astronomers for about a decade. In this period highly significant emission of VHE gamma rays has been detected from nine astronomical objects. The VHE emission from four of these objects, the Crab nebula, PSR1706, Mrk421 and Mrk501 has been confirmed by independent observations. Coordinated multi-wavelength campaigns including VHE telescopes have produced important data for the theoretical modelling of these objects. Observations of sources of VHE gamma rays have allowed the continuing investigation into a diverse range of physics including; the origin of cosmic rays, fundamental particle physics, cosmology and the nature of matter in the intense gravitational and magnetic fields around some astronomical objects. In particular the discovery of the Crab nebula as a standard candle of VHE gamma rays has greatly assisted the development and calibration of Atmospheric Cherenkov Telescopes (ACT) in the Northern Hemisphere.

The Durham University Mk6 telescope is a highly sensitive IACT telescope with a low energy threshold of ~300GeV. It is one of only two fully operational VHE telescopes in the Southern Hemisphere, the other belonging to the CANGAROO collaboration (threshold energy ~1.5TeV). The Durham Mk6 telescope consists of three 42m^2 flux collectors arranged on a horizontal axis on a single alt-azimuth mount. Each flux collector is viewed by a photon detector comprising a PMT camera. Together the three detectors form a sophisticated coincidence trigger that allows the PMTs to be run at high gain and gives the telescope its low energy threshold. Routine analysis of Cherenkov data, by the IACT, is performed on the high resolution images recorded by the central camera. Although the medium resolution Left and Right detectors were designed to provide the coincidence trigger for the telescope they still record some information about the Cherenkov images. This thesis has investigated the use of the images from the Left and Right detectors to provide extra gamma/hadron discrimination power from that obtained by analysing the central camera alone.

The differences between gamma ray and hadron initiated Extensive Air Showers (EAS) were investigated in Chapter 3 with the use of Monte-Carlo simulations. It was found that the fluctuations in Cherenkov photon density were larger for hadron EAS than gamma ray EAS when measured over distances comparable to the 14m separation of the Left and Right detectors. This is due to fundamental differences in the longitudinal development of hadron and gamma ray initiated EAS. Several gamma/hadron discriminating parameters based on a simple, low order, moments analysis of the Left/Right images have been introduced. These are;

LRR and **LRF** - Parameters describing the fluctuations in Cherenkov photon density measured over a 14m baseline.

dDist - The difference of the centroid position of Cherenkov images of the same shower seen in the Left and Right detectors.

LRconc - A measure of the total Cherenkov photon density seen by the combined area (84m^2) of the Left and Right mirrors.

The effects on the parameters of detector resolution, mirror optical performance and photon noise were investigated in Chapter 7. The largest reduction in the gamma/hadron discrimination power of the Left/Right parameters was found to be due to photon noise.

In Chapter 8 a detailed computer model of the Mk6 telescope was constructed. The model was compared against, and agrees well with, observed data. The effectiveness of Left/Right parameters was investigated after an IACT analysis, based on that used on observations with the Mk6 telescope of Cen X-3, was performed on the simulated central camera images. For any of the Left/Right parameters to be successful gamma/hadron discriminators it is necessary to account for noise in the PMT signals. This was performed by calculating the image moments from signals where the signal to noise ratio was > 6. It was found that *dDist* and *LRconc* could offer a 20-30% improvement in source detection significance after a routine IACT analysis. This work has therefore highlighted analysis methods by which the performance of the Mk6 telescope could be improved in a simple manner.

9.2 Future Work

Several interesting areas for future work have been indicated by this thesis, which should be considered as a report of work in progress. The first priority must be the application of the new Left/Right parameters to observed data from gamma ray sources. Other areas are indicated below.

9.2.1 Further Exploitation of Cherenkov Image Information

This thesis has shown that two medium resolution Cherenkov images, taken with detectors separated by small distances, possess information that can be used to help to identify gamma rays from the hadron background. The 20-30% improvement in source detection significance that was obtained with *dDist* may be further improved by representing the information in other ways; for example, the *xdDist* and *ydDist* components of *dDist* could be applied to the data separately. The second order moments, which describe the shape of the images, contain information that has not been exploited here. It is true that their gamma/hadron discrimination power may be limited by the effects of the 0.5° pixel size and photon noise. Nevertheless, the use of the M_2 moments should be investigated, perhaps by making some measure of the differences in *Width* or *Azwidth* measured in the Left and Right detectors.

Using the large (84m^2) flux collecting area of the Left and Right mirrors to calculate *LRconc*, a measure of Cherenkov photon density, was also found to improve gamma ray source detection significance. In the absence of noise it was found that this quantity was a function of Cherenkov brightness. Improvements in gamma/hadron discrimination power could be obtained by creating a new parameter which takes account of the variation with brightness. The information could also be represented in different ways, perhaps by a ratio of the summed Left and Right image/total brightness. A major improvement could be made by including data from the central camera. This however would require careful calibration of the responses to Cherenkov photons of the 1-inch and hexagonal PMTs in use in the three detectors.

9.2.2 New Simulations

The development of ground based gamma ray astronomy in the Northern Hemisphere has been greatly aided by the discovery of the Crab nebula as a standard candle VHE source. This object is difficult to observe from the Southern Hemisphere; it culminates at a zenith angle ~50° at Narrabri during the Southern summer months when the nights are short and weather conditions are often poor. Therefore a telescope model which accurately reproduces observed hadron images would be a very valuable tool for the Durham group. The model discussed in Chapter 8 has been a major step forward in accomplishing this for events above ~1000 digital counts. Work is currently underway on the next generation of simulations for the Mk6 telescope, which hope to better represent the low brightness events than can be done currently. The GENESIS air shower simulation code was written several years ago by K.J. Orford to answer specific questions about the Durham University telescopes. It was chosen at the start of this thesis over other available simulation codes for this work for many reasons; these included the low overheads in set up time due to its previous use for modelling the Durham telescopes, the availability of on-site support from the author and the suitability of the computing resources then available at Durham University. A new model is currently under development that uses the MOCCA air shower simulation code. The MOCCA code is in extensive use around the world and has been chosen to allow better comparison of the results of modelling the Mk6 telescope with those of other groups. Of paramount importance is an improved understanding of the telescope's trigger. This will require careful measurement of all aspects of the performances of the Mk6 telescope.

9.2.3 Upgrades to the Mk6 Telescope

The next generation of ground based ACTs will be multiple stereoscopic arrays and have cameras with very high angular resolution, $\sim 0.1^\circ$. A new array of sensitive telescopes in Australia is unlikely to be built in the near future due to financial considerations. However several upgrade options exist for the Mk6 telescope. The first of these would be to construct new aluminium mirrors for the telescope. At present the optical performance of the telescope is not ideal — the PSF measured in Chapter 5.1.2 suggests that ~30-40% of the light from a point source is imaged within a single tube. It should be possible to produce three new mirrors with PSFs $< 0.05^\circ$ for a modest total cost ~£20,000. This would allow improvements in the detectable gamma ray energy threshold of the telescope and the imaging and analysis of low energy events.

The next possible stage in upgrading the Mk6 telescope would be to replace the Left and Right triggering detectors with similar element PMT arrays. A coincidence trigger requiring that corresponding PMTs in all three detectors pass a discriminator threshold would be operated. Preliminary simulation results suggest that such a system could have an energy threshold (defined in Section 5.1.6) of ~200GeV and would trigger on a significant fraction of 100GeV gamma rays. Improvements in the effectiveness of the Left/Right parameters as gamma/hadron discriminators discussed in this thesis would be obtained by such an upgrade. In addition, further exploitation of the information in the Cherenkov images would be possible by consideration of the higher order moments and the correlations of the Hillas parameters seen in all three dishes. Upgrading the Left and Right detectors in this manner would require an increase in the channels of electronics as well as additional PMTs and cost in the region of £100,000.

Finally an upgrade to the central camera has been considered in addition to replacing the mirrors and the Left and Right detectors. Currently the Mk6 telescope is capable of imaging events containing ~800 digital counts, corresponding to a gamma ray energy of ~300-400GeV at 30° zenith angle. The minimum analysable energy is limited by the PMT resolution; a Cherenkov image needs to appear in ~5 or more 'image and border' PMTs to allow the calculation of meaningful moments. By doubling the resolution of the camera PMTs the analysable images should be obtained from gamma ray EAS with primary energy lower by a factor ~4. Initial simulation studies are underway to model the response of a 'Mk7' telescope with good optics, Left and Right detectors with 91×0.25° resolution elements and a central camera consisting of 469×0.125° resolution PMTs. Two rings of 0.5° PMTs will probably surround the high resolution area, giving the camera a full field of view >4° . By operating a high resolution version of the current Mk6 coincidence trigger it could be possible to image and analyse Cherenkov images from EAS with primary energy < 100GeV. This would be a significant improvement in ground based gamma ray astronomy and allow significant overlap in the observable electromagnetic spectrum using the IACT and Solar Farm techniques. An upgrade of this magnitude would require an investment of ~£300,000 to construct with a further ~£200,000 to operate per year. When compared with the expenses involved in building large telescopes at other wavelengths and high energy satellite experiments such a telescope would be a cost effective tool for cosmology, high energy physics and the continuing search for the origins of cosmic rays.

9.2.4 Future Southern Hemisphere VHE Observations

The most exciting results from the IACT era of ground based gamma ray astronomy has been the discovery of strong, highly variable VHE emission from several Active Galactic Nuclei (AGN). The first AGNs to be discovered in the TeV range were the Northern Hemisphere objects, Mrk421 and Mrk501. Since then two other AGNs have been detected at $> 6\sigma$ significance; PKS2155 and 1ES2344 [40], [29]. Neither of these objects have been confirmed by independent measurements, although the emission is transient in nature. PKS2155 is an important object; it is the first Southern Hemisphere BL Lac object to be observed at these energies and is the most distant of the four AGNs. A measurement of the VHE spectrum of PKS2155 would be very important for studies of the extragalactic IR flux given its large distance ($z = 0.117$ as opposed to $z \sim 0.03$ for the three Northern AGN [43]).

Observations of galactic microquasars (GMC) would give insights into the nature of AGN jets at VHE energies. All of the objects currently identified as GMC are observable from the Southern Hemisphere [116]. Relativistic jets are observed in these objects and as such GMC can be considered as the galactic analogies of AGN. No 'microblazars', i.e. GMC with jets aligned with the line of sight, have yet been observed although VHE emission could still be detected at Earth due to the relative proximity of the objects [7]. In addition the Southern Hemisphere offers opportunities to observe other sources such as the X-ray binaries and plerions. The Galactic Centre itself is a broad source of GeV radiation that may extend to VHE energies [141] and observations with sensitive VHE telescopes may be able to detect emission lines from the annihilation of supersymmetric particles [10]. The field of VHE gamma ray astronomy can only benefit from continuing to observe with and develop ground based telescopes in the Southern Hemisphere.

REFERENCES

[1] Acharya, B.S. *et al.*, 1992, *Astron. Astrophys.*, **258**, 412.

[2] Aguilar-Benitez, M. *et al.*, (Particle Data Group, CERN), 1994, *Phys. Rev.*, **D50**, 1173.

[3] Aharonian, F.A. *et al.*, 1995, *J. Phys. G: Nucl. Part. Phys.*, **21**, 419.

[4] Allan, 1971, *Prog. Elem. Part. and Cosmic Ray Physics*, **10**, 170.

[5] Amelino-Camelia, G. *et al.*, 1998, *Nature*, **383**, 319.

[6] Armstrong, P., *et al.*, 1999, *Exp. Astron.*, **9**, 51.

[7] Atoyan, A.M. and Aharonian, F.A., 1999, *M.N.R.A.S.*, **302**, 253.

[8] Badran, H.M. *et al.*, 1997, *Proc.* 25th *Int. Cosmic Ray Conf.*, Durban, **5**, 185.

[9] Barrau, A. *et al.*, 1998, *Nucl. Instrum. Meth.*, **A416**, 278.

[10] Bergström, L. *et al.*, 1998, *Astropart. Phys.*, **9**, 137.

[11] Bhat, P.N. *et al.*, 1980, *Astron. Astrophys.*, **81**, L3.

[12] Bhat P.N. *et al.*, 1986, *Nature*, **319**, 127.

[13] Bhat, P.N., 1997, *astro-ph/9706026.*

[14] Bhat, C.L., 1997, *proc. Towards a Major Atmospheric Cerenkov Detector V*, de Jager, O.C., (ed.), Berg-en-Dal, 398.

[15] Biller, S.D. *et al.*, 1998, *Phys. Rev. Lett.*, **80**, 2992.

[16] Biller, S.D. *et al.*, 1999, *to be published in Phys. Rev. Lett.*

[17] Blackett, P.M.S., 1948, *Phys. Soc. London, Gaissot Comm. Rep.*, 34.

[18] Böttcher, M. and Bloom, S.D., 1998, *submitted to Ap. J. (astro-ph/9806249)*

[19] Bowden, C.C.G. *et al.*, 1992, *Astropart. Phys.*, **1**, 47.

[20] Bowden, C.C.G. *et al.*, 1993, *Towards a Major Atmospheric Cerenkov Detector II*, Lamb, R.C., (ed.), Calgary, 230.

[21] Bowden, C.C.G. *et al.*, 1993 *Proc.* 23^{rd} *Int. Cosmic Ray Conf.*, Calgary, **1**, 293.

[22] Brazier, K.T. *et al.*, 1989, *Exp. Astron.*, **1**, 77.

[23] Buckley, D.J. *et al.*, 1998, to be published in *Exp. Astron.*,

[24] Bulian, N. *et al.*, 1998, *Astropart. Phys.*, **8**, 223.

[25] Burle Industries Inc., 1980, *"Photomultiplier Handbook"*, **TP-136**, Lancaster, PA, USA.

[26] Bussóns-Gordo, J. *et al.*, *Towards a Major Atmospheric Cerenkov Detector V*, de Jager, O.C., (ed.), Berg-en-Dal, 293.

[27] Cameron, R.A. *et al.*, 1992, *The Compton Observatory Science Workshop*, Schrader, C.R. *et al.* (eds.), NASA, Washington, **3137**, 3.

[28] Catanese, M.A. *et al.*, 1997, *Ap. J.*, **487**, L143.

[29] Catanese, M.A. *et al.*, 1998, *Ap. J.*, **501**, 616.

[30] Catanese, M.A., 1999, *to appear in proc. DPF'99 (astro-ph/9903244)*

[31] Cawley, M.F., 1993, *Towards a Major Atmospheric Cerenkov Detector II*, Lamb, R.C. (ed.), Calgary, 176.

[32] Čerenkov, P. A., 1937, *Phys. Rev.*, **52**, 378.

[33] Chadwick, P.M. *et al.*, 1990, *J. Phys G: Nucl. Part. Phys.*, **16**, 1773.

[34] Chadwick, P.M. *et al.*, 1995, *Proc. 24th Int. Cosmic Ray Conf.*, Rome, **2**, 88.

[35] Chadwick, P.M. *et al.*, 1995, *Proc. 24th Int. Cosmic Ray Conf.*, Rome, **2**, 374.

[36] Chadwick, P.M. *et al.*, 1996, *Sp. Sci. Rev.*, **75**, 153.

[37] Chadwick, P.M. *et al.*, 1997, *Towards a Major Atmospheric Cherenkov Detector V*, de Jager, O.C. (ed.), Berg-en-Dal, 173.

[38] Chadwick, P.M. *et al.*, 1998, *Ap. J.*, **503**, 391.

[39] Chadwick, P.M. *et al.*, 1998, *Astropart. Phys.*, **9**, 131.

[40] Chadwick, P.M. *et al.*, 1999, *Ap. J.*, **513**, 161.

[41] Chadwick, P.M. *et al.*, 1999, *to be given at 26th Int. Cosmic Ray Conf.*, Utah.,

[42] Chadwick, P.M. *et al.*, 1999, *accepted for publication in J. Phys. G: Nucl. Part. Phys.*

[43] Chadwick, P.M. *et al.*, 1999, *Astropart. Phys.*, **11**, 145.

[44] Cheng, K.S. *et al.*, 1986, *Ap. J.*, **300**, 500.

[45] Cheng, K.S. *et al.*, 1986, *Ap. J.*, **300**, 522.

[46] Cheng, K.S. and Ruderman, M., 1989, *Ap. J.*, **333**, L77.

[47] Cheng, K.S. and Ruderman, M., 1991, *Ap. J.*, **373**, 187.

[48] Cheng, K.S. and Ding, Winnis K.Y., 1994, *Ap. J.*, **431**, 724.

[49] Chitnis, V.R., Bhat, P.N., 1998, *Astropart. Phys.*, **9**, 45.

[50] Couper, H., 1998, *New Scientist*, **2160**, 42.

[51] Daum, A. *et al.*, 1997, *Astropart. Phys.*, **8**, 1.

[52] Daum, A. *et al.*, 1997, *proc. Towards a Major Atmospheric Cerenkov Detector V*, de Jager, O.C., (ed.), Berg-en-Dal, 178.

[53] Dickinson, J.E., 1995, *PhD. Thesis*, University of Durham, U.K.

[54] Dietz, L.A., *et al.*, 1967, *Rev. Sci. Inst.*, **38**, 176.

[55] Dowthwaite, J.C. *et al.*, 1984, *Ap. J.*, **286**, L35.

[56] Dowthwaite, J.C. *et al.*, 1984, *Nature*, **309**, 691.

[57] Durham Gamma Ray Group web site, 1999, http://www.dur.ac.uk/~dph0www4/

[58] Edwards, P.G. *et al.*, 1993, *Proc. Astr. Soc. Aus.*, **10**, 287.

[59] Ellsworth, R. W. *et al.*, 1982, *Phys. Rev.*, **D26**, 336.

[60] Erber, T., 1966, *Rev. Modern Phys.*, **38**, 626.

[61] Fazio, G.G. *et al.*, 1972, *Ap. J.*, **175**, L117.

[62] Fegan, D.J. *et al*, 1994, *Towards a Major Atmospheric Cerenkov Detector III*, Kifune, T., (ed.), Tokyo, 149.

[63] Fegan, D.J., 1997, *J. Phys. G: Nucl. Part. Phys.*, **23**, 1013.

[64] Finley, J.P. *et al.*, 1997, *Amer. Astron. Soc.*, **191**, 4806.

[65] Fishman, G.J. *et al.*, 1992, in *The Compton Observatory Science Workshop*, Schrader, C.R. *et al.* (eds.), NASA, Washington, **3137**, 26.

[66] Fletcher, R.S. *et al.*, 1994, *Phys. Rev.*, **D50**, 5710.

[67] Fossati, G. *et al.*, 1998, *M.N.R.A.S.*, **299**, 433.

[68] Frank, I.M., Tamm, I.G., 1937, *Dokl. Akad. Nauk, SSSR*, **14**, 109.

[69] Funk, B. *et al.*, 1998, *Astropart. Phys.*, **9**, 97.

[70] Gaisser, T.K., 1990, *"Cosmic Rays and Particle Physics"*, Cambridge University Press, Cambridge, U.K.

[71] Galbraith, W. and Jelley, J.V., 1953, *Nature*, **171**, 349.

[72] Galbraith, W. and Jelley, J.V., 1953, *J. Atmosph. Terr. Phys.*, **6**, 250.

[73] Gibson, A.I. *et al.*, 1982, *Nature*, **296**, 833crab.

[74] Gillanders, G.H. *et al.*, 1997, *Proc.* 25th *Int. Cosmic Ray Conf.*, Durban, **3**, 185.

[75] Ghisellini, G *et al.*, 1999, *astro-ph/9906165,*

[76] Goeckel, 1910, *Phys. Zeits.*, **11**, 280.

[77] Goret, P. *et al.*, 1997, *Towards a Major Atmospheric Cherenkov Detector V*, de Jager, O.C. (ed.), Berg-en-Dal, 166.

[78] Hartman, R.C.. *et al.*, 1992, in *The Compton Observatory Science Workshop*, Schrader, C.R. *et al.* (eds.), NASA, Washington, **3137**, 116.

[79] HEGRA Collaboration web site, 1999,
http://wpos6.physik.uni-wuppertal.de:8080/Pictures/

[80] den Herder, J.W. *et al.*, 1992, in *The Compton Observatory Science Workshop*, Schrader, C.R. *et al.* (eds.), NASA, Washington, **3137**, 85.

[81] Hess, V.F., 1911, *Phys. Zeits.*, **12**, 998.

[82] Hewish, A. *et al.*, 1968, *Nature*, **217**, 709.

[83] Hillas, A.M., 1985, *Proc.* 19th *Int. Cosmic Ray Conf.*, La Jolla, **3**, 445.

[84] Hillas, A.M., 1987, in *Very High Energy Gamma Ray Astronomy*, K.E.Turver (ed.), D. Reidel Publ. Co., Dordrecht, Holland.

[85] Hillas, A.M., Patterson, J.R., 1990, *J. Phys. G: Nucl. Part. Phys.*, **16**, 1271.

[86] Hillas, A.M., 1996, *Sp. Sci. Rev.*, **75**, 17.

[87] Hillas, A.M., 1998, *Ap. J.*, **503**, 744.

[88] Hinton, J.A., 1998, *PhD Thesis*, University of Leeds.

[89] Hofmann, W. *et al.*, 1997, *Towards a Major Atmospheric Cherenkov Detector V*, de Jager, O.C. (ed.), Berg-en-Dal, 405.

[90] Holder, J., 1997, *PhD. Thesis*, University of Durham, U.K.

[91] de Jager, O.C. *et al.*, 1996, *Ap. J.*, **457**, 253.

[92] de Jager, O.C. (ed.), 1997, *proc. Towards a Major Atmospheric Čerenkov Detector V*, Space Research Unit, Potchefstroom University, South Africa.

[93] Jelley, J.V., 1958, *"Čerenkov Radiation and its Applications"*, Pergamon Press, London.

[94] Jelley, J.V.and Galbraith, W. , 1955, *J. Atmosph. Terr. Phys.*, **6**, 304.

[95] Jelley, J.V. and Porter, N.A., 1963, *Q. J. R. Astron. Soc.*, **4**, 275.

[96] Kalekin, O.R. *et al.*, 1994, *Towards a Major Atmospheric Cerenkov Detector III*, Kifune, T., (ed.), Tokyo, 107.

[97] Kifune, T., *et al*, 1995, *Ap. J.*, **438**, L91.

[98] Kifune, T., 1997, *Towards a Major Atmospheric Cerenkov Detector V*, de jager, O.C. (ed.), Berg-en-Dal, 55.

[99] Király, P. and Mészáros, P., 1988, *Ap. J.*, **333**, 719.

[100] Klepikov, N.P., 1954, *Zh. Eksperim. Teor. Fiz*, **26**, 19.

[101] Knapp, J. and Heck, D., 1998, *"EAS Simulation with CORSIKA: A User's Guide"*, **V5.61**, Institut fur Kernphysik, Karlsruhe, Germany.

[102] Kohnle, A. *et al.*, 1996, *Ast. Part. Phys.*, **5**, 119.

[103] Krawczynski, H. *et al.*, *Proc. BL Lac Phenomenon*, Turku, Finland, 29.

[104] Lessard, R.W. *et al.*, 1997, *proc. Towards a Major Atmospheric Cerenkov Detector V*, de Jager, O.C., (ed.), Berg-en-Dal, 356.

[105] Lewis, D.A. et al, 1993, *Proc.* 23^{rd} *Int. Cosmic Ray Conf.*, Calgary, **1**, 279.

[106] LHEA web site, 1999. http://antwrp.gsfc.nasa.gov/apod/

[107] Longair, M.S., 1997, *"High Energy Astrophysics Volume 1"*, Cambridge University Press, Cambridge.

[108] Longair, M.S., 1997, *"High Energy Astrophysics Volume 2"*, Cambridge University Press, Cambridge, U.K.

[109] Lyne, A.G. and Graham-Smith, F., 1990, *"Pulsar Astronomy"*, Cambridge University Press, Cambridge.

[110] Macomb, D.J. and Gehrels, N., 1999, *Ap. J.*, **120**, 335.

[111] Mallet, L., 1926, *C.R. Acad. Sci. (Paris)*, **183**, 274.

[112] Mallet, L., 1928, *C.R. Acad. Sci. (Paris)*, **187**, 222.

[113] Mallet, L., 1929, *C.R. Acad. Sci. (Paris)*, **188**, 445.

[114] Matsubara, Y., 1997, *proc. Towards a Major Atmospheric Cerenkov Detector V*, de Jager, O.C., (ed.), Berg-en-Dal, 447.

[115] Meintjes, P.J. *et al.*, 1992, *Ap. J.*, **401**, 325.

[116] Mirabel, I.F. and Rodríguez, L.F., 1999, *to appear in Ann. Rev. Astron. Astrophys.*, **37**..

[117] Mohanty, G. *et al*, 1997, *Astroparticle Phys.*, in press

[118] Morton, G.A. *et al.*, 1968, *Appl. Phys. Lett.*, **13**, 356.

[119] Moskalenko, I.V., 1994, *Sp. Sci. Rev.*, **72**, 593.

[120] Nishimura, J., 1994, *Towards a Major atmospheric Cherenkov Detector III*, Kifune, T. (ed.), 1.

[121] Ong, R.A., 1998, *Phys. Rep.*, **305**, 93.

[122] Ong, R.A. and Covault, C.E., 1997, *proc. Towards a Major Atmospheric Cerenkov Detector V*, de Jager, O.C., (ed.), Berg-en-Dal, 247.

[123] Orford, K.J., 1997, *Private Communication.*

[124] Paré, É., 1997, *Towards a Major Atmospheric Cerenkov Detector V*, de Jager, O.C., (ed.), 228.

[125] van Paradijs, J., *"Neutron Stars and Black Holes in X-Ray Binaries"*, to be published in *"The Many Faces of Neutron Stars"*, Buccheri, R. *et al.* (eds), Kluwer Accademic Publishers.

[126] Petry, D. and Kranichm D., 1997, *proc. Towards a Major Atmospheric Cerenkov Detector V*, de Jager, O.C., (ed.), 368.

[127] Plaga, R., 1998, *to be published in Frascati Physics Series*, **11**, 369.

[128] Prescott, J.R. et al., *Nuc. Instr. Methods*, **39**, 173.

[129] Press, W.H., 1986, *"Numerical Recipes: The art of scientific computing"*, Cambridge University Press, Cambridge, U.K.

[130] Procureur, J., 1997, *proc. Towards a Major Atmospheric Cerenkov Detector IV*, Padova, 383.

[131] Punch, M. *et al*, 1991, *Proc.* 22^{nd} *Int. Cosmic Ray Conf.*, Dublin, **1**, 464.

[132] Punch, M. *et al.*, 1992, *Nature*, **358**, 477.

[133] Québert, J., 1997, *proc. Towards a Major Atmospheric Cerenkov Detector V*, de Jager , O.C. (ed.), Berg-en-Dal, 234.

[134] Quinn, J. *et al.*, 1996, *Ap. J.*, **456**, L83.

[135] Rao, M.V.S. and Sinha, S., 1988, *J. Phys. G: Nucl. Part. Phys.*, **14**, 811.

[136] Reynolds, 1993, *Ap. J.*, **404**, 206.

[137] Rivoal, M., 1997, *Towards a Major Atmospheric Cerenkov Detector V*, de Jager, O.C., (ed.), 89.

[138] Roberts, I.D., 1998, *PhD. Thesis*, University of Durham, U.K.

[139] Robson, I., 1996, *"Active Galactic Nuclei"*, Wiley-Praxis, Chichester.

[140] Romani, R., 1996, *Ap. J.*, **470**, 469.

[141] Québert, J. *et al.*, 1997, *Towards a Major Atmospheric Cerenkov Detector V*, de Jager, O.C., (ed.), 142.

[142] Rutherford and Cooke, 1903, *Phys.Rev.*,**16**, 183.

[143] Roberts, I.D., 1998 *PhD. thesis*, University of Durham.

[144] Sinha, S., 1995, *J. Phys. G: Nucl. Part. Phys.*, **21**, 473.

[145] Sinitsyna, V.G., 1997, *proc. Towards a Major Atmospheric Cerenkov Detector V*, de Jager, O.C., (ed.), Berg-en-Dal, 190.

[146] Stecker, F.W. and De Jager, O.C., 1998, to be published in *Astron. Astrophys. Lett. (astroph/9804196)*

[147] Sturrock, P.A., 1971, *Ap. J.*, **164**, 529.

[148] Sommers, P. and Elbert J.W., 1987, *J. Phys. G: Nucl. Part. Phys.*, **13**, 553.

[149] Tanimori, T. *et al*, 1997, *proc. Towards a Major Atmospheric Cerenkov Detector V*, de Jager, O.C., (ed.), Berg-en-Dal, 158.

[150] Tanimori, T. *et al.*, 1997, *Ap. J.*, **497**, L25.

[151] Thompson, D.J. *et al.*, 1993, *Ap. J. Supp.*, **86**, 629.

[152] Tümer, O.T. *et al.*, R.C, 1985, *Proc.* 19th *Int. Cosmic Ray Conf.*, La Jolla, **1**, 139.

[153] Turver, K.E. & Weekes, T.C., 1978, *Nuovo Cimento*, **45B**, 99.

[154] Turver, K.E., 1997, *Towards a Major Atmospheric Cerenkov Detector V*, de Jager, O.C., (ed.), Berg-en-Dal, 389.

[155] Urry, C.M., 1998, *talk given at Turku Conf. Bl Lac Phenom. (astro-ph/9812420).*

[156] Vladimirskii, B.M. *et al.*, *Proc. 13th Int. Cosmic Ray Conf.*, Denver, **1**, 456.

[157] Weekes, T.C. *et al.*, 1972, *Ap. J.*, **174**, 165.

[158] Weekes, T.C., 1988, *Phys. Reports*, **160**, 1.

[159] Weekes, T.C. *et al.*, 1989, *Ap. J.*, **342**, 379.

[160] Weekes, T.C., 1992, *Sp. Sci. Rev.*, **59**, 314.

[161] Weekes, T.C. *et al.*, 1997, *proc. Towards a Major Atmospheric Cerenkov Detector V*, de Jager, O.C., (ed.), Berg-en-Dal, 202.

[162] Weekes, T.C. *et al.*, 1997, *proc. Towards a Major Atmospheric Cerenkov Detector V*, de Jager, O.C., (ed.), Berg-en-Dal, 433.

[163] Whipple Collaboration Web Site, 1999,
http://egret.sao.arizona.edu/

[164] Witten, E., 1996, *Nucl. Phys. B*, **471**, 135.

[165] Yodh, G.B. *et al.*, 1983, *Phys. Rev*, **D27**, 1183.

[166] Yoshikoshi, T. *et al.*, 1997, *Ap. J.*, **487**, L65.

[167] Zombeck, M.V., 1990, *"Handbook of Space Astronomy and Astrophysics, second edition"*, Cambridge University Press, Cambridge.